Alma Mater Studiorum · Università di Bologna

Scuola di Scienze
Dipartimento di Fisica e Astronomia
Corso di Laurea Magistrale in Fisica

Neutron Veto of XENONnT: final construction design of the system and extensive study and calibration of the PMTs.

Relatore:
Prof.ssa Gabriella Sartorelli

Correlatore:
Dott.ssa Federica Agostini

Presentata da:
Andrea Mancuso

Anno Accademico 2018/2019

Sommario

Numerose e convincenti sono le evidenze sperimentali che portano a credere che gran parte dell'Universo sia costituito dalla cosiddetta Materia Oscura. Molti sforzi, sia sperimentali che teorici, sono stati dedicati alla ricerca della materia oscura a tal punto da essere considerata uno dei più grandi misteri della fisica moderna. La possibilità di interazione esclusivamente gravitazionale e debole con la materia ordinaria ne rende complicata la rivelazione. I candidati più promettenti a comporre la materia oscura sono da ricercarsi in teorie oltre il Modello Standard e sono genericamente chiamati WIMP, acronimo per Weakly Interacting Massive Particles.

I rivelatori che nel corso del tempo hanno raggiunto i livelli di sensibilità più competitivi, hanno in comune le caratteristiche di essere costruiti con materiali ultra-puri e di essere posizionati sotto terra, essendo, così, schermati dai raggi cosmici. Il progetto XENON è situato presso i Laboratori Nazionali del Gran Sasso (LNGS), in Italia, sotto una copertura di roccia corrispondente a 3600 metri di acqua; con l'esperimento XENON1T, si è riuscito a ottenere il miglior limite di esclusione per la sezione d'urto di interazione WIMP-nucleone indipendente dallo spin per WIMP di massa superiore a 6 GeV/c^2, con un minimo a 4.1×10^{-47} cm^2 per 30 GeV/c^2. Tale risultato è stato ottenuto con l'impiego di una Time Projection Chamber (TPC) a doppia fase (liquida e gassosa) con una massa attiva di 2 t di xenon (di cui 1.3 t utilizzate come volume fiduciale).

Il prossimo step del rivelatore è XENONnT, il quale sta attraversando la fase finale di costruzione. Con una TPC più grande, contenente 6 t di xenon, il principale obiettivo è quello di aumentare il potenziale di rivelazione delle WIMP migliorando la sensibilità di un ordine di grandezza in 5 anni di presa dati. Questo risultato può essere raggiunto solo con una sostanziale diminuzione del background, ottenuta con un'ulteriore riduzione dei contaminanti dello xenon e dei materiali che compongono il rivelatore, e, inoltre, impiegando il sistema del Neutron Veto (nVeto); quest'ultimo ha lo scopo di rivelare i neutroni radiogenici provenienti dai materiali dell'esperimento. Il nVeto sarà installato intorno al criostato (contenente la TPC) e sfrutterà la presenza di gadolinio in acqua (con una concentrazione dello 0.2 % in massa di solfato di Gd), per incrementare notevolmente la sezione d'urto di cattura neutronica e rendere l'efficienza di rivelazione dei neutroni dell'ordine del 85%.

Il nVeto sarà costituito da 120 fotomoltiplicatori (PMT) Hamamatsu R5912 (8 pollici di fotocatodo), caratterizzati da un'alta quantum efficiency ed una bassa radioattività. I PMT saranno installati su una struttura che circonda il criostato, assicurando il contenimento della luce proveniente dagli eventi di cattura neutronica.

Il design della struttura, così come la sua installazione, sono responsabilità del gruppo di ricerca di Bologna. La descrizione del lavoro per progettare e realizzare il nVeto è argomento di questa tesi. Inoltre, è stato effettuato uno studio approfondito delle performance dei PMT tramite un setup sperimentale presso i LNGS nel periodo tra Marzo e Luglio 2019. La descrizione completa del setup, così come dei risultati dei test dei PMT del nVeto è l'altro importante argomento su cui si focalizza questa tesi.

Abstract

Numerous and convincing are the experimental evidences that led to the believe that most of the Universe is constituted by the so-called Dark Matter (DM). Its research has attracted many theoretical and experimental efforts to the point of being considered the greatest mystery of modern physics. The possibility of DM interacting only gravitationally and weakly makes its detection a huge challenge. The most promising candidates to DM belong to theories beyond Standard Model and are generically named as WIMPs, an acronym for Weakly Interacting Massive Particles.

The detectors that have reached the most competitive sensitivity levels in the hunt for dark matter have in common the characteristics of being built with ultra-pure materials and located underground, in order to be shielded from cosmic rays. The XENON project, located at the Laboratori Nazionali del Gran Sasso (LNGS), in Italy, under 3600 meters-water-equivalent mountain rock, managed to set so far, with the XENON1T experiment, the world-best exclusion limits of WIMP-nucleon spin-independent interaction cross-section for WIMP masses above 6 GeV/c^2, with a minimum of 4.1×10^{-47} cm^2 at 30 GeV/c^2. To achieve this result, the experiment employed a dual-phase (liquid-gaseous) Time Projection Chamber (TPC) with 2 t of xenon active mass (1.3 t of which used as fiducial volume). The next step of the detector is XENONnT, which is currently in the final assembling stage. With a bigger TPC containing 6 t of xenon active mass, the main goal is to improve the detection potential for WIMPs by increasing the sensitivity of one order of magnitude in five years of data taking. That result can be achieved only with a substantial background lowering attained with a further reduction of the contaminants of the xenon as well as of the detector materials and finally with the Neutron Veto system (nVeto); the latter is defined as a detector which tags the radiogenic neutrons coming from the materials of the experiment. The nVeto will be installed around the cryostat (containing the TPC) and will employ the gadolinium-loaded water technology (with a 0.2% in mass of Gd-sulphate) to significantly enhance the neutron capture cross-section such that the nVeto tagging efficiency becomes of the order of 85%.

The nVeto will be instrumented with 120 8-inches Hamamatsu R5912 photomultipliers (PMT) featuring high quantum efficiency and low radioactivity. The PMTs will be installed in a structure all around the cryostat, which ensures an optical containment of the light from the neutron capture events. The design of the nVeto structure, as well as its construction, is under the responsibility of the Bologna research group. Most of the work done to design and realize the Neutron Veto system is the argument of this thesis. In addition, an extensive study of the nVeto

photomultiplier performance has been done in a dedicated experimental setup at the LNGS in the period between March and July 2019. The complete description of the setup, as well as the results of the Neutron Veto PMT tests, is the other big topic of this thesis.

Contents

Introduction

Here is an astonishing fact: all the matter that interacts and that we can observe, constitutes less than 5% of the Universe's total mass-energy. Then what about the remaining 95%? The answer to this question represents one of the greatest mysteries of physics. Both experimental evidences, as well as theoretical models, lead most of the physicists to believe that about 68.5% is made up of dark energy while the remaining 26.5% can be ascribed to dark matter. Those hypotheses widely motivated efforts in the investigation of these areas for years.

The description of the dark matter research landscape is the topic of Chapter 1 of this thesis. The different evidences on the astronomical and cosmological scale have made it possible to narrow the search field for particle candidates to compose all the amount of invisible matter in our Universe. By invisible matter, we mean that it does not interact electromagnetically with ordinary matter, but only gravitationally and weakly. Therefore we are dealing with particles characterized by a very low interaction cross-section and this makes their detection very challenging. Theories beyond the Standard Model provide the most promising candidate particles for DM; they are generically called **W**eakly **I**nteracting **M**assive **P**article (WIMP). As for the detection strategies, they are divided into direct, indirect detection and production at colliders. By flying over the other two techniques, in the direct search for DM we try to detect the energy release of target nuclei after the interaction with the WIMPs. Since the expected rate of events of this type is rather low (below few events/ton/year) their observation relies on massive, ultra-pure detectors located in low radioactivity environments and shielded from cosmic rays; thus the main experimental facilities are placed underground.

Chapter 2 is dedicated to the XENON project, which is leading the direct search of dark matter. It is located in the Laboratori Nazionali del Gran Sasso (LNGS), in Italy, under 3600 meters-water-equivalent of mountain rock. The experiment employs a cylindrical dual-phase Time Projection Chamber (TPC) filled with ultra-pure xenon in liquid phase (LXe), with a small gap of gaseous xenon (GXe) on the top. The choice of the xenon as target is due to its property of being an excellent scintillator medium (ideal to detect rare scattering events) as well as an ionization medium with high charge yield. The light produced from the scintillation is collected by two arrays of Photomultiplier Tubes (PMTs) placed at the top and the bottom of the TPC. On the other hand, by applying an internal electric field, the electrons from ionization are drifted towards the gas region on the top; there, secondary electrons are extracted and accelerated to produce a signal through proportional scintillation. The power of this technology consists of using a combination of two signals (ionization and scintillation) in order to disentangle WIMPs interactions

from background events, allowing to reach an impressive background reduction. The XENON1T experiment represents the first tonne-scale detector, with a total of 3.2 t xenon, and is so far the most sensitive DM detector in the world. The background reduction allowed us to set an upper limit for WIMP masses above 6 GeV/c^2, with a minimum at 4.1×10^{-47} cm^2 for a mass of 30 GeV/c^2 [1]. Following the excellent results obtained, the XENON Collaboration moved to the XENONnT upgrade (with about 8 t LXe), aiming at improving the experimental sensitivity to WIMPs by an order of magnitude, thanks to the $\sim$4 times larger target mass and the enhanced background suppression. The latter will be achieved also thanks to the presence of a new detector, the Neutron Veto (nVeto), which provides a radiogenic neutron tagging efficiency around 85%. The combination of the low radioactivity material selection, together with the nVeto allows reaching a radiogenic background suppression of factor 6.

In Chapter 3, the reasons that led to the development of a neutron tagging detector, as well as its description are presented. The nVeto will be located between the walls of the water tank and the cryostat, achieving an optical separation, by means of a stainless steel structure on which reflective panels and 120 PMTs are installed. The PMTs detect the photons emitted following the neutron capture process; the latter will be enhanced by adding gadolinium sulphate to the water.

The PMTs that will be used in the nVeto are the Hamamatsu R5912; the diameter of the photocathode is 8" and they feature high quantum efficiency ($\geq$ 30%), low radioactivity, low dark rate ($\leq$ 6 kHz) and high gain ($\sim 10^7$). The detailed description of the photomultipliers, as regards the underlying physics and their role within the XENON project, is the topic of Chapter 4. In view of the installation of the photomultipliers within the experiment, tests were organized in order to cross-check, with respect to the values quoted on the Hamamatsu data-sheets, their main parameters as the gain, the dark rate, the transit time and the transit time spread. The PMTs' parameters were also monitored at different supply voltage, in order to be able to decide in which condition we want to keep them inside the nVeto (for instance, such that they are equalized in gain within few %). Moreover, during the tests, we measured the influence of the Earth's magnetic field on the performance of the PMTs, by comparing the gain, the peak-to-valley ratio and (indirectly) the PMT's detection efficiency without and with the employment of a mu-metal magnetic shield. The tests, entirely performed at the Laboratori Nazionali del Gran Sasso between March and July 2019 (following the tight schedule of the XENON Collaboration), were carried out in a light-tight water tank setup, the so-called Small Water Tank. The topic of Chapter 5 is the description of the experimental setup and the results of the tests.

Very soon we will install the Neutron Veto, the last step of the complete installation of the XENONnT experiment. The work of optimizing the structure of the apparatus (Chapter 3), as well as the calibration of the photomultipliers (Chapter 5), are the main topics of this thesis and will show to be fundamental for the construction of the nVeto system and to ensure the required efficiency of the detector.

Chapter 1

Dark matter

Matter as we know it, atoms, stars, galaxies, and planets, accounts for less of 5% of the known Universe; about 25% is Dark Matter and 75% Dark Energy, both of which are invisible [2]. This suggests that everything we experience is only a tiny fraction of reality. The hunt of Dark Matter (DM) has spanned decades, attracting large and growing efforts in the scientific community; thus, his existence represents one of the major open questions in Physics. The name "*Dark Matter*" refers to the fact that it does not interact with electromagnetic radiation, resulting invisible. The existence of DM came from Fritz Zwicky's observations; in 1993, from a study on the redshifts of various galaxy clusters, he noticed a large discrepancy in the apparent velocities of eight galaxies within the Coma Cluster (figure 1.1), with differences that exceeded 2000 km/s [3]. Taking into account the

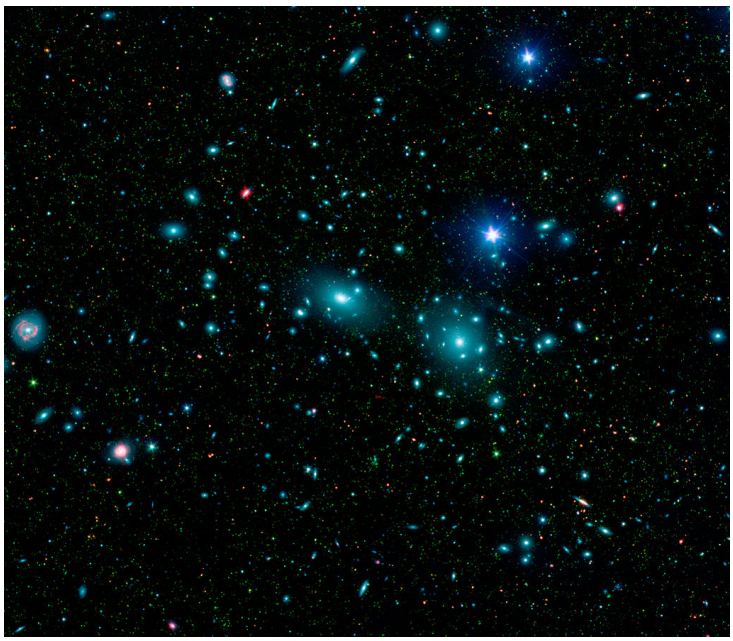

Figure 1.1: Central region of the Coma Cluster, located in the Coma Berenices Constellation with a mean distance of 321 million light-years. The Coma Cluster provided the first evidence of gravitational anomalies which were considered to be indicative of unobserved mass. This image is obtained by a combination of data from the Sloan Digital Sky Survey and from NASA's Spitzer Space Telescope.

mass of the visible matter, the velocity of the galaxies resulted about one order of magnitude higher than the expectations. To explain this behavior Zwicky came to "*the surprising result that dark matter is present in a much greater amount than luminous matter*" [3]. Up to now the existence of DM is firmly established among physicists since many astronomical and cosmological evidences were collected in the last century (Section 1.1). However there is no shortage of alternative theories; some of them, as the modified theory of gravity (Section 1.1.5) could explain the observation of the gravitational effects introducing some corrections to General Relativity and avoiding the necessity to postulate the presence of an unknown class of particles.
On the other hand, the idea of DM particles (Section 1.2) is based on the certainty that the Standard Model cannot fulfill all the required properties. Among the several particle models proposed, the most promising candidates are called Weakly Interacting Massive Particles (WIMPs), which are subjected to weak force as well as to the gravitational one. The interest in this class of particles is linked to the fact that WIMPs are well suited in several models beyond SM and can be investigated with the current technologies. Several experiments, realized in the last years, are focused to inspect different regions in the DM parameter space (Section 1.3); they mostly exploits two different techniques: direct detection (based on the interaction between WIMP and ordinary matter) and indirect detection (which consists of the observation of the annihilation products of two WIMPs).

1.1 Dark matter evidences

In his study of the Coma Cluster, Zwicky estimated the mass of the cluster with the Virial Theorem [4]. A cluster is a structure of galaxies that moves with very complex dynamics; thus, the velocities of the galaxies were determined by measuring the Doppler effect on their spectra. For the Virial Theorem[1], one has that $U = -2K$, where U and K are the potential and kinetic energy respectively. Assuming a spherical distribution of the galaxies inside the cluster, the mass is then given by:

$$M = \frac{R \langle v^2 \rangle}{G} \tag{1.1}$$

where v is the mean squared velocity. Since only the line of sight velocities $v_{\parallel}^2$ can be determined via redshift, a factor three is introduced in Eq.1.1. The physical size of the cluster was considered to be around 2×10^6 light-year; assuming that the cluster contained around 000 galaxies with a velocity dispersion measured of ~ 1000 km/s, Zwicky found an average of $4.5 \times 10^{10} M_{\odot}$ mass per galaxy. This value is several orders magnitude higher than the average absolute luminosity of Coma's galaxies which is around $8.5 \times 10^7 L_{\odot}$, leading to a very high mass-to-light ratio (~ 500). Although this ratio was overestimated with respect to the current measurements, the result was considered as one of the leading evidence of the presence of dark matter, which contributes to the mass without increasing the galactic luminosity. However, Zwicky's considerations were not the only ones that showed a discrepancy

[1] in case of a stationary distributed system

with respect to the expectation resulting from a Universe without the Dark Matter. In the next sections, there is an overview of the main evidences on the astrophysical and cosmological scale.

1.1.1 Galaxy scale evidences

The measurements of the rotation curves of spiral galaxies are considered the most reliable evidences of dark matter. Spiral galaxies (Figure 1.2) are rotationally sustained systems.

Figure 1.2: Image of the NGC6503 dwarf spiral galaxy displayed by Hubble's Advanced Camera for Surveys. The galaxy is located at the edge of a region of space called the Local Void and is said to be gravitationally alone since it does not belong to a larger galaxy group or cluster.

Their velocity distribution can be measured by evaluating the hydrogen clouds velocity with the indications from the 21 cm line of the natural Hydrogen HI and from its low level of absorption in the interstellar medium. Several spiral galaxies were studied in the 70s; all of them showed mass discrepancy from the rotational curves. Simple models of spiral galaxies consider these systems as being made of a central core (disk + bulge) and an outer region; the central core is supposed to contain almost all the mass of the galaxy. The dynamic of these systems can be simply described assuming a spherical distribution of the mass. Thus, the velocity distribution is given by:

$$\frac{v(r)^2}{r} = \frac{GM(r)}{r^2} \quad \Rightarrow \quad v(r) = \sqrt{G\frac{M(r)}{r}} \tag{1.2}$$

where the mass $M(r)$ contained in the spherical central core is given by:

$$M(r) = 4\pi \int_0^R \rho(r) r^2 dr \tag{1.3}$$

with $\rho(r)$ matter density of the galaxy. From Eq.1.2 one expects that outside the optical disk, the visible mass distribution stays constant and the velocity drops as $v(r) \propto r^{-1/2}$.

On the other hand, in most spiral galaxies, such as the NGC 6503 [5] and the M33 Galaxy [6], it was observed a constant velocity distribution in the outermost regions (Fig.1.3).

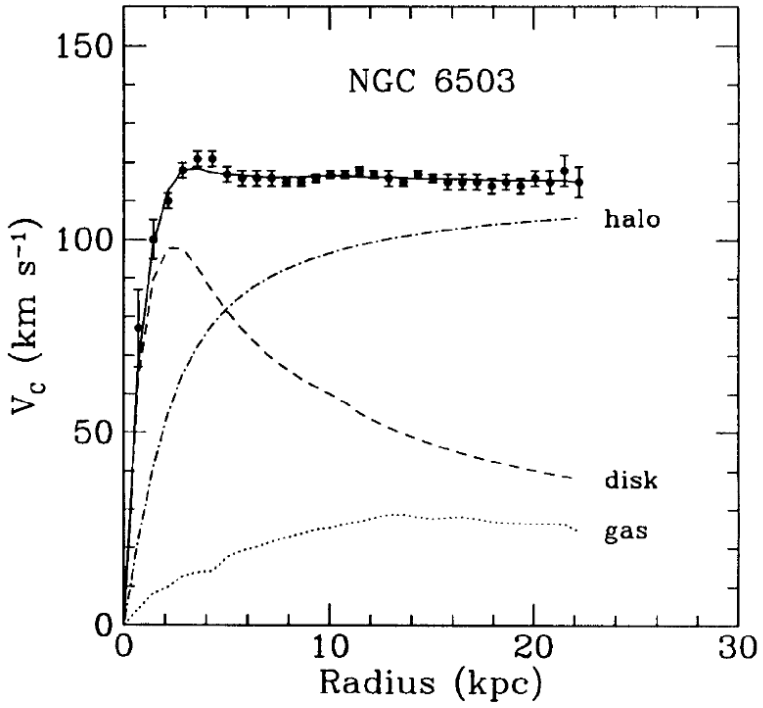

Figure 1.3: Velocity distribution of the NGC 6503. The black dots are the observed data while the dashed line is the behavior expected considering only the disk contribution. It is clear the need for the dark halo contribution to match the data.

Such result could be explained assuming that the spiral galaxies are enclosed in *dark halos* with a density profile $\rho \propto r^{1/2}$; for instance one popular density profile that fits well the profile obtained from gravitational lensing data (Section 1.1.2) is given by the Navarro-Franck-White (NFW) model:

$$\rho(r) = \frac{\rho_s}{(r/r_s)(1 + r/r_s)^2} \tag{1.4}$$

where r_s is the halo scale radius and ρ_s is its characteristic density.

1.1.2 Gravitational lensing

One successful technique to investigate DM is based on the Gravitational Lensing effect, the deflection of photons as they pass through the warped spacetime of a gravitational field [7]. The path of the light rays from distant sources is not "straight" (in an Euclidean frame) when passing near massive objects, such as stars, clusters of galaxies or dark matter. This effect was first observed in 1919 during a solar eclipse in front of the Hyades Cluster whose stars appeared to move as they passed behind the Sun [8]. This effect is easier to observe around a dense concentration of mass (such as a core of a galaxy or cluster of galaxies); in this

regime called *strong lensing*, the space-time is so warped that light can travel along multiple paths around the lens and be deflected back towards the observer. Commonly the line of sight does not pass near a strong gravitational lens, thus the light deflection can be very slight; this situation is called *weak regime*.

When only the light of physically small sources is significantly affected, with the extended background sources like galaxies that are effectively immune, the phenomenon is called *gravitational microlensing* [9]. Unlike the strong and weak lensing, what is observed in the microlensing technique is a time modulation of the luminosity of the source (Figure 1.4) due to the relative motion with respect to the lens (characterized by a reasonable duration, from seconds to years instead of millions of years); this technique was exploited by B. Paczyński [10] to investigate Dark Matter in the form of massive compact halo objects (MACHOs) in the Galactic halo.

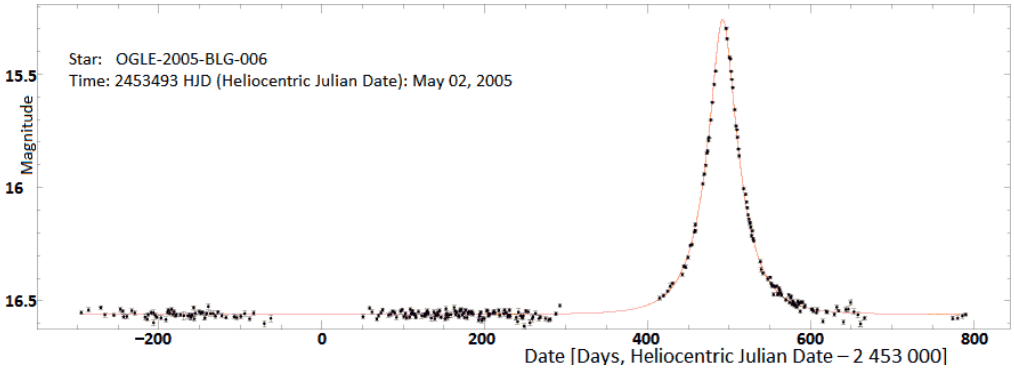

Figure 1.4: Typical light curve of a microlensing event of the OGLE-2005-BLG-390L star located in the Scorpius Constellation [11].

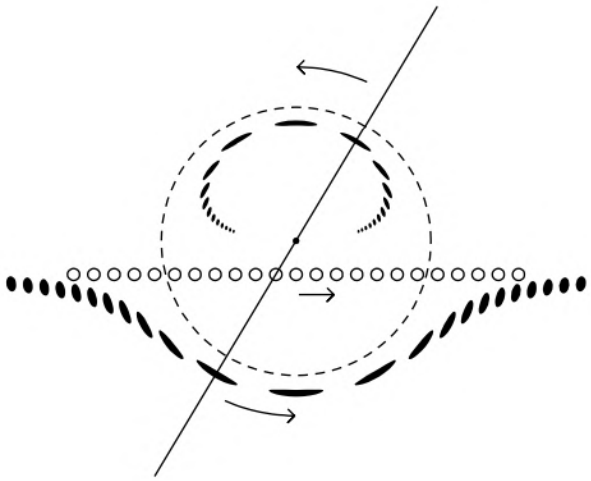

Figure 1.5: The geometry of gravitational lensing: the lensing mass (indicated with a dot) is located at the center of the *Einstein ring*, marked with a dashed line. The source positions in each instant are shown with a series of small open circles. The locations and the shapes of the two images are drawn as a series of dark ellipses. Picture taken from [10].

In the mathematical description of the microlensing the main parameter is the *Einstein Radius* θ_E which is the angular radius of the Einstein ring (Figure 1.5) in case of perfect alignment:

$$\theta_E = \sqrt{\frac{4GM}{c^2}\frac{D_S - D_L}{D_S D_L}} \quad \text{[rad]} \tag{1.5}$$

where D_L and D_S are the distance of the lens and the source respectively, from the observer plan, and M is the lens mass. Since this angle is generally of the order of microarcseconds (thus the therm *microlensing*), the detection of the lensing events depends on their duration (the so-called *Einstein Crossing Time*) related to the lens mass, distance, and velocity. Historically the first two microlensing events interpreted as caused by dark matter were observed in the direction of Large Magellanic Cloud and the results were published by MACHO and EROS collaborations [12]. This interpretation was due to the discrepancy between the visible mass and the mass calculated from the lensing effect. With the detection in the following years of additional events, the data rejected the hypothesis that all the dark halo comprises MACHOs [13], but the two collaborations found a significant unexplained excess of $\sim$ 20% of the halo mass. Currently, the SuperMACHO project [14] seeks to locate and to investigate the nature of the lenses responsible for MACHO's results.

1.1.3 Bullet cluster

The *Bullet Cluster* (BC) is the collision between galaxy clusters. Strictly speaking, the name bullet cluster refers to the smaller subcluster, moving away from the larger one as for the famous BC (1E0657-558) shown in figure 1.6a. From the collision an emission in the X-ray can be observed; it is linked to the interaction inside the intergalactic hot gas. This emission gives a clear image of the matter distribution that can be detected by an X-ray telescope like Chandra. The pink area in figure 1.6 represents the distribution of the intergalactic gas which is the majority of ordinary matter in the galaxy, while the blue area is the mass distribution reconstructed with the weak lensing [17]. Due to the electromagnetic interaction, the hot plasma is decelerated during the collision; thus the stars of the galaxies proceed on ballistic trajectories. From the figures reported it is clear the discrepancy between the distribution of ordinary luminous matter with respect to the total mass. Thus, gravitational lensing studies of BC are claimed to provide the best evidence to date for the existence of dark matter. Even if the observations of other galaxy cluster collisions, such as MACS J0025.4-1222 (Figure 1.6b), similarly support the existence of dark matter, the discussion is still open because of the discrepancy with computational models and for the several attempts to describe the phenomenon with the Modified Dynamic theory (MOND).

1.1.4 Cosmological scale evidences

Several convincing experimental evidences of the DM scenario, that can not be explained by invoking modifications of the laws of dynamics (Section 1.1.5), come

(a) (b)

Figure 1.6: (a) Picture of the MACS J0025.4-1222 BC [15]. (b) Picture of the 1E0657-558 BC [16]. Both the figure represent bullet cluster events and are obtained by the composition of a picture made by Hubble optical telescope and an X-Ray image from the Chandra X-Ray observatory; the latter is overlaid in pink, showing the distribution of hot gas in the two clusters and thus of the ordinary luminous matter. The blue regions represent the mass distribution reconstructed from weak lensing measurements. The discrepancy is evident for both the events.

from the *Cosmic Microwave Background* (CMB). The CMB was discovered accidentally by Penzias and Wilson in 1965 [18] and consists of relic photons from the early Universe when the temperature dropped down to ~ 3000 K (allowing the recombination of the electrons with protons). In that phase, the Universe became transparent to photons as they had not enough energy to ionize hydrogen. Even if the spectrum of CMB is a perfect black body with a temperature $T_0 = (2.7255 \pm 0.0006)$ K [19], it shows anisotropies at the 10^{-5} lower level; these anisotropies were originated from quantum fluctuation before the primordial nucleosynthesis that caused a not uniform matter distribution and can give huge hints on the Universe Composition.

Because of the peak structure of the CMB spectrum (Figure 1.7) it is possible to obtain an angular power spectrum through the expansions of the anisotropies into spherical harmonics:

$$\frac{\delta T}{T}(\theta, \phi) = \sum_{l=2}^{+\infty} \sum_{m=-l}^{+l} a_{lm} Y_{lm}(\theta, \phi) \tag{1.6}$$

From Eq.1.6 several information on cosmological parameters such as the curvature of the Universe and the energy-matter composition can be extracted. The Plank Collaboration recently released the most accurate estimation of these parameters [2], from which the abundance of DM is :

$$\Omega_{DM} h^2 = 0.120 \pm 0.001 \tag{1.7}$$

while the baryonic matter density is $\Omega_b h^2 = 0.0224 \pm 0.0001$, a factor 5 less abundant than the DM. The estimate of the total matter density is thus:

$$\Omega_m h^2 = 0.315 \pm 0.007 \tag{1.8}$$

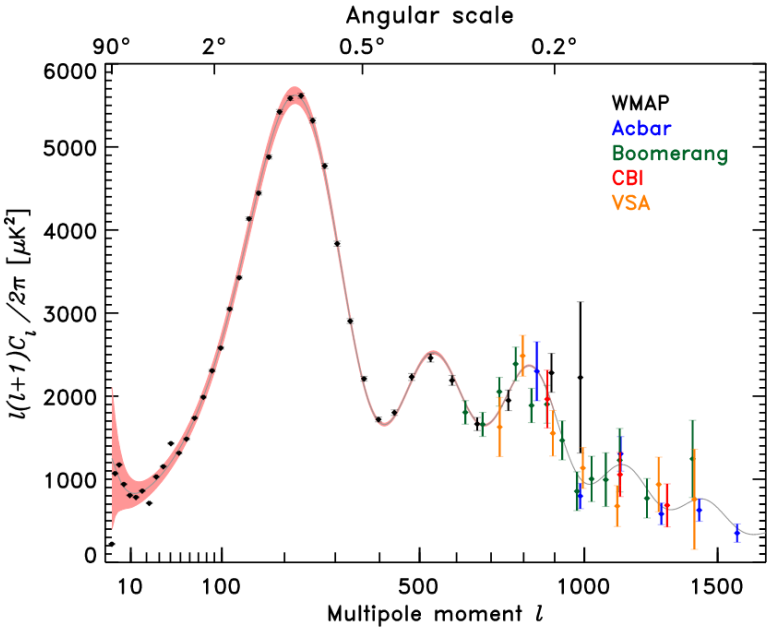

Figure 1.7: Plot of the angular power spectrum of the CMB radiation temperature anisotropy. The data represented comes from the WMAP (2006), Acbar (2004) Boomerang (2005), CBI (2004), and VSA (2004) instruments. The best fit came from the ΛCMD model. Plot from [20]

The remaining 68.5% of the Universe is in the form of Dark Energy, the energy introduced to account the accelerated expansion of the flat Universe.

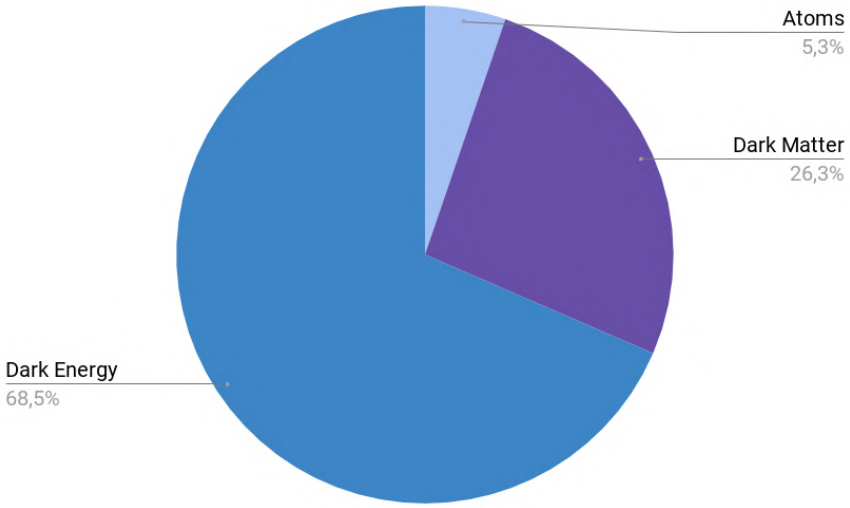

Figure 1.8: Chart of the contributions to the Universe content (results from the final full-mission Planck measurements of the CMB anisotropies [2]).

All the contributions found (Figure 1.8) are consistent with the ΛCDM (Λ Cold Dark Matter) cosmological model, which results from the study of the large-scale structures in the Universe; the latter indicated the existence of DM and a nonzero

cosmological constant. The Cold Dark Matter model also provides indications on the structure formation in the early Universe, which are considered by cosmologists to be the strongest arguments for DM existence. In particular, these would have originated from the growth of initial perturbation in matter density; the consistency with the actual size of the perturbation in matter ($\delta\rho/\rho \gtrsim 1$) is only obtained with the introduction of a non-baryonic dark matter. The success of the ΛCDM model allows for the discrimination of the candidate particles for DM.

1.1.5 Modified Newtonian Dynamics

Some of the evidences reported can be explained avoiding the introduction of DM, by simply modifying the theory of gravitation. The first argument of this paradigm is that Einstein's General Relativity (GR) has successfully passed every direct experimental test only on small scales compared to the cosmological ones; thus a modified gravity theory has the aim to solve the DM problem up to cosmological scale. The first alternative theory to DM was the **MO**dified **N**ewtonian **D**ynamics (MOND) proposed by Milgrom (1982) [21], who claimed to solve the galaxy rotation curves problem raised by Zwicky in 1933. Following the idea of Special Relativity for which the Newtonian dynamics does not apply in determined regimes, Milgrom stated that the MOND regime is the one with very low acceleration with respect to the scale $a_0 \sim 10^{-10}$ m/s^2 which is on the order of the centripetal accelerations of gas clouds in disk galaxies. Thus, the modified second law of dynamics is

$$\widetilde{\mu}\,(a/a_0)\,\vec{a} = -\vec{\nabla}\Phi_N \tag{1.9}$$

where the positive monotonic function $\widetilde{\mu}$ tends to unity when $a \gg a_0$ and tends to its argument (a/a_0) in the deep MOND regime; Φ_N is the newtonian gravitational potential originated by the baryonic mass density. The MOND theory could explain the galactic rotational curves as well as the mass discrepancy in galaxy clusters. However, it is a non-relativistic model and there are a lot of obstacles if one attempts to give a relativistic formulation. Even if there are some attempts to generalize also GR [22], the observations of gravitational waves (of which the first occurred on September 14, 2015 [23]) rejected all the MOND-like theories, confirming the entire GR framework.

1.2 Dark matter particles

The identification of dark matter is an open question and there are no particle models that fulfill all the requirements associated to the DM; the hypothesized candidates have very different production mechanisms in a very wide range of masses, from 10^{-5} eV of axions to 10^{13} GeV like SuperHeavy WIMP. However they share the requirement to be stable on a cosmological time scale, otherwise, they would have already decayed, and they must provide the correct matter density Ω_{DM} (Section 1.1.4); furthermore the coupling with ordinary matter must be gravitational and (possibly) weak. To exclude some candidates, one should consider that dark matter plays a crucial role on the formation and evolution of structures in the Universe; in particular, the primordial velocity during the decoupling phase of DM

from the cosmological fluid is an important parameter that leads to three possible scenarios:

- Hot Dark Matter;
- Cold Dark Matter;
- Warm Dark Matter.

The Hot Dark Matter (HDM) scenario involves relativistic DM particles at the time of decoupling and the corresponding model of structure formation is the *top-down model*; according to this, the large structures were formed first and then fragmented into smaller units [24]. The primary candidates as DM particles in this scenario are Standard Model *relic neutrinos*. However, this fragmentation model is not consistent with the observed galaxies' age. Furthermore, the constraints on the relic neutrinos' density lead to the rejection of the HDM hypothesis. Nowadays, the Cold Dark Matter (CDM) scenario characterized by massive non-relativistic DM is the most accepted and supported. This scenario leads to the *bottom-up model*, for which large structures were formed from the aggregation of small objects. Most of the valuable candidates for the CDM scenario come from theories beyond the SM; among those, the most investigated class of candidates for CDM are the Weakly Interacting Massive Particles (WIMP) (Section 1.2.1). Finally, there is the Warm-DM model, which stands as a middle ground between the other two by proposing a top-down formation for small structures and a bottom-up for larger structures. The most motivated candidate in this framework is the *Sterile Neutrino*, a right-handed neutrino with only gravitational coupling with matter. Regarding the baryonic contribution to the DM, it was pointed as the responsible for the mass contained in the dark galactic halos in the form of MACHOs, *MAssive Compact Halo Objects*; this term refers to non-luminous objects like black holes, neutron stars, brown dwarf and very faint red dwarfs. As already reported in section 1.1.2, the latest data from EROS and SuperMACHO claimed that MACHOs contribute for less than 20% to the total DM in galactic halos. Even if the results confirm the existence of a fraction of baryonic Dark Matter, the following paragraphs focus on the major contributions of non-baryonic nature.

Relic neutrinos The first natural approach that can be taken addressing the problem of DM nature, is to investigate based on the certainties contained in the Standard Model of particle physics. As a matter of fact, what one founds is that it is possible to remain in the SM framework only dealing with the HDM scenario, in particular with the *relic neutrinos*. Relic neutrinos are stable, weakly interacting and relativistic particles, main candidates for the HDM; in this scenario, they were originated after the Big Bang and formed the *Cosmic Neutrino Background* ($C\nu B$) [25]. The predicted density is given by

$$\Omega_\nu h^2 = \sum_{i=1}^{3} \frac{m_i}{93 \text{ eV}} \tag{1.10}$$

where m_i are the masses of the three neutrino flavours. The constraint for the sum of the neutrino masses is provided by the latest Planck's data [26]:

$$\sum_{i=1}^{3} m_i < 0.12 \text{ eV} \quad (95\% \; C.L.) \tag{1.11}$$

Such upper bound implies a limit on the relic density of $\Omega_\nu h^2 < 0.0013$ which is not consistent with the estimated total DM density in Eq.1.7. Furthermore, another consideration that allows rejecting these candidates is their relativistic nature, which implies the formation of galactic structures according to the top-down model; the latter results to be inconsistent with cosmological data.

Axions From the extension of the SM for the solution of the strong CP problem, *axions* emerge as possible candidates for DM. In 1977, R. Peccei and H. Quinn postulated a new global chiral symmetry $U(1)_{PQ}$, to avoid the violation of the CP symmetry in the QCD framework [27]; in this theory, the axions are the *Nambu-Goldstone bosons* (NG) occurring for the spontaneous symmetry breaking (SSB) of the group. The coupling of the NG bosons to the SM particles is suppressed by the energy scale that characterizes the SSB, *i.e.* the decay constant f which appear in the interaction Lagrangian:

$$\mathcal{L} = f^{-1} J^\mu \partial_\mu \phi \tag{1.12}$$

with J^μ Noether current of the SSB. In the Peccei-Quinn mechanism the symmetry is broken at a scale of f_A, the axion decay constant, also called *PQ scale*. From the chiral perturbation theory one founds that axions mass is given by:

$$m_A = 5.691(51) \left(\frac{10^9 \text{GeV}}{f_A} \right) \text{meV} \tag{1.13}$$

Furthermore, limits on the PQ theory parameters came from the expression of the relic abundance of the axions:

$$\Omega_A h^2 = \theta^2 \left(\frac{f_A}{10^{12} \text{GeV}} \right)^{1.175} \tag{1.14}$$

with $\theta \sim 0.1$ and $f_A \sim 10^{12}$GeV which might support the hypothesis of a CDM consisting of axions; assuming this, the constraint on the mass of the particles would be $m_A = (2.6 \pm 0.3) \times 10^{-5}$eV.

The detection of axions is based on the *Primakoff effect* (Figure 1.9), in which an axion is converted into a photon under the effect of a magnetic field, according to the coupling

$$L_{A\gamma\gamma} = -g_\gamma \frac{a}{\pi} \frac{A(x)}{f_A} \vec{E} \cdot \vec{B}. \tag{1.15}$$

There are several experiments investigating the *Axion Like Particles* (ALPs); some of them exploit the conversion $\gamma \to A \to \gamma$ (with the so-called *Light-Shining-through-Walls* technique), such as the OSQAR experiment [28], others instead observe the variation of polarization of a photon beam (due to axion generation) as the PVLAS experiment [29].

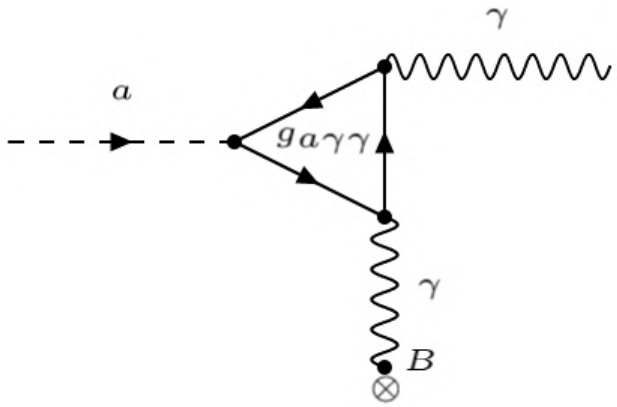

Figure 1.9: Feynman diagram of the Primakoff Effect consisting of the conversion of the axion a into a photon γ under the effect of a magnetic field B. Also the reverse process can happen.

Even the dark matter direct research experiments (Section 1.3.1) conceived for WIMP search have the ability to investigate ALPs, taking advantage of the axio-electric effect (Figure 1.10) in liquid xenon; this was done with the LUX [30] and XENON100 [31] experiments. Currently the most promising experiment focused

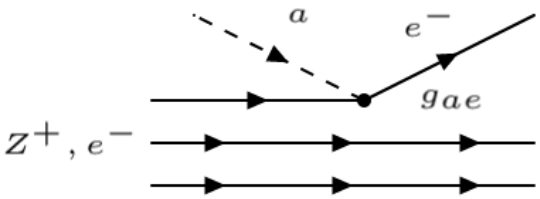

Figure 1.10: Feynman diagram of the Axio-Electric Effect which is a photoelectric-like process.

in this topic is ADMX, which recently demonstrated unprecedented sensitivity to axion-photon coupling [32], and is going through an upgrade that will test axion models in a wider range of masses. By extending these considerations to the Supersymmetric theories, the axion has both a scalar and a fermionic superpartner; the latter is called *axino* and could be the lightest supersymmetric particle (LSP) as well as a candidate for CDM [33].

Sterile neutrinos As already discussed before, neutrinos, for their elusive nature, are in principle a very natural DM candidate. The reasons why the known neutrinos can not explain all of the evidences for DM are the smallness of their mass as well as the magnitude of their coupling to SM particles. Hence, the most intuitive

hypothesis is the existence of heavier "*sterile*" neutrinos with weaker interactions; all these requirements must also comply with the constraints from cosmic structures formation and the matter densities observed. The *sterile neutrinos* were proposed as DM candidates by Dodelson and Widrow in 1994 [34], with only the constraint for the mass in the order of keV. These particles are conceived as neutral, massive and unstable, with a lifetime longer than the age of the Universe. Such sterile neutrinos would have been produced in the early Universe at high temperatures and, unlike other cosmic relic particles, their very weak interaction strength would have prevented the reach of the thermal equilibrium. The interaction of sterile neutrinos with ordinary matter could leave imprints in X-ray spectra of galaxies and galaxy clusters; thus the possibility of their detection relies on X-ray observations by X-ray satellites. Recently, it has been observed an unidentified feature in galaxy clusters spectra. The signal, consisting of an X-ray line at ~ 3.5 keV [35], could be interpreted as coming from the decay of a DM particle with the mass ~ 7 keV. This observation from the XMM-Newton satellite has been repeatedly questioned because of the lack of other supporting evidences; thus, possible explanations of the origin of the line include statistical fluctuation or instrumental feature, as well as atomic transition. Therefore, the understanding of the nature of ~ 3.5 keV line relies on the next generation of high-resolution X-ray missions, including XARM (Hitomi replacement mission), LYNX and Athena (Figure 1.11).

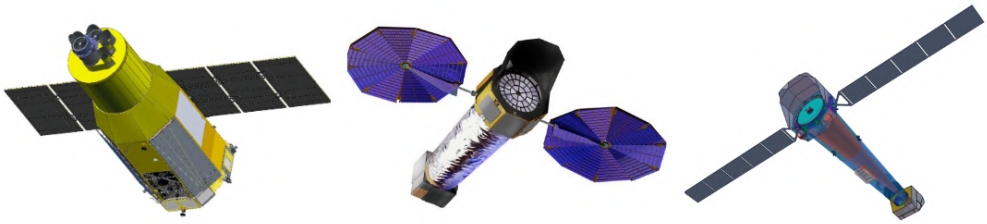

Figure 1.11: Models of the three most promising satellites employed in the understanding of the anomalous X-ray signals in galaxy cluster spectra. (a) The X-ray Imaging and Spectroscopy Mission (XRISM) (formerly XARM) is JAXA/NASA collaborative mission, with ESA participation [36]. (b) The Lynx X-ray Observatory is a concept study for the next X-ray space telescope mission, with the launch planned in 2035 [37]. (c) The Advanced Telescope for High Energy Astrophysics (ATHENA) is the X-ray observatory mission designed by ESA; also this is planned for ∼2030 [36].

Supersymmetric particles Supersymmetry (SUSY) stands as the most popular extension of the SM to face a series of phenomenological problems like the hierarchy problem [38], the unification of gauge symmetries and the fine-tuning of Higgs boson mass [39]. SUSY is a space-time symmetry defined by the transformation between supermultiplets, consisting of an SM particle and its supersymmetric partner; particles within a multiplet share the same quantum numbers except for the spin, which differs by 1/2. It goes without saying that such a framework could also propose an elegant solution to the DM problem, theorizing the existence of

several CDM candidates. Among them, the most interesting one is the *lightest supersymmetric particle* (LSP) whose existence results to be a consequence of the *R-Parity* conservation[2] defined as:

$$R = (-1)^{3B+L+2S} \tag{1.16}$$

where B, L and S are baryonic, leptonic number and spin respectively. All the SM particles share the same $R = +1$, while superpartners have $R = -1$. From the conservation law of Eq. 1.16, one can easily conclude that an LSP is stable since it can not decay into any SM particle (characterized by an opposite R), neither into an odd number of SUSY particles for energy considerations. Thus, an LSP would be an excellent candidate for CDM and the detection would be possible only via annihilation. In the previous paragraph dedicated to the *axion*, its superpartner, the *axino*, has been already introduced; other relevant superpartner in the DM topic are the *sneutrinos*, the *gravitinos* and the *neutralinos*.
The **sneutrinos** are the supersymmetric partners of the neutrinos with a mass ranging between 550 GeV and 2300 GeV [40]. For a long time they were considered the most promising candidates for DM for their hypothetical relic density; nowadays their relevance is waning because of a scattering cross-section expected higher than the exclusion limits set by DM direct experiments [40].
The **gravitino** is instead the superpartner of the graviton; it is a fermion and with its mass of the order of the eV is the LSP in some SUSY frameworks. However, the coupling with the ordinary matter of gravitational nature would imply an inefficient production mechanism in the primordial Universe which therefore would not explain the measured Ω_{DM}.
As the name suggests, the *Minimal Supersymmetric Standard Model* stands as the minimal set of fields to extend the Standard Model and realizing the supersymmetry consistent with phenomenology [41]. In this framework the SM gauge field superpartners are the followings:

- `bino` $\widetilde{B}$: superpartner of the $U(1)$ gauge field corresponding to *weak hypercharge*;
- `wino` $\widetilde{W_3}$: superpartner of the Z boson of the $SU(2)_L$ gauge fields.
- `higgsinos` $\widetilde{H_1^0}$ and $\widetilde{H_2^0}$: superpartner of the higgs fields.

They mix into four Majorana fermionic mass eigenstates, called **neutralinos**. The neutralinos are the most studied and investigated DM candidates. Their relevance is explained in section 1.2.1, dedicated to the discussion of the Weakly Interacting Massive Particles.

Other candidates In a non-thermal scenario, relic super-heavy DM particles can be found. These particles, known as *Wimpzillas*, defined in a wide range of masses (from 10^{10} to 10^{16} GeV/c^2), have been proposed as a first explanation for the ultra-high energy cosmic rays observed above the GZK cut-off [42]; above this threshold of $\sim 5 \cdot 10^9$ eV the Universe becomes opaque to protons. Lacking any

[2] whose validity is granted in the *Minimal Supersymmetric Standard Model* (MSSM)

proposal for high energy source, the hypothesized production mechanism is the annihilation (or the decay) of superheavy DM.
Moving on towards Extra Dimension theories, the lightest particle, called *Kaluza-Klein* particle, has been proposed as a viable candidate for DM [43]. The Kaluza-Klein theory constituted an attempt to formulate an extra-dimensional theory to include electromagnetism in the framework of GR. It was proposed in 1921 by Kaluza [44], who suggested the metric for a classical five-dimensional theory; the latter was simply an extension of the GR metric. Klein's contribution [45] came, five years later, with the quantum interpretation of the theory. Among the particles theorized, the lightest one would have a mass ranging between 10 to 1000 GeV. Even if there is a great variety of other candidate particles for DM, the interest of the main experiments in this topic is addressed to Weakly Interacting Massive Particles, whose main features are reported in the next section.

1.2.1 Weakly Interacting Massive Particles

Models beyond SM, such as SUSY, predict as best suited candidate for particle DM the so-called *Weakly Interacting Massive Particles*. More in detail, WIMPs are a class of particles with the following features:

- electrically neutral;
- non-baryonic;
- with masses in the 1 GeV - 100 TeV range;
- cold at the decoupling from primordial plasma;
- stable or extremely long-lived;
- they interact with SM particles with cross-sections typical of weak interactions (weak self-interaction are expected as well).

WIMPs became, in the '80s, the preferred DM candidates because of the predicted relic abundance consistent with the observed DM one. This class of particles is usually split according to their production as "thermal" or "non-thermal" relics. In the first case, the production would have happened in the early Universe in thermal equilibrium conditions, with the decoupling phase or "*freeze out*" occurring when their interactions could not keep up with the Universe expansion; after the abundance "froze out", the number of WIMPs per co-moving volume remained constant. The non-thermal relics were not produced in this way, but rather via the decay of other particles. What changes between the two models is the expected relic density. Thus, the interest is usually addressed to the standard freeze-out scenario. Assuming WIMPs of mass m_χ one has that for $T > m_\chi$ they were in thermal equilibrium; with decreasing temperature, below m_χ, the decoupling started as their abundance began to lower. Finally, when the expansion rate of the Universe became larger than the annihilation rate, the WIMP abundance saturated resulting to be the current one.

By studying the evolution of WIMP density one finds out that the relic density can be expressed as a function of the annihilation rate:

$$\Omega_\chi h^2 = 3 \cdot 10^{-27} \frac{cm^3 s^{-1}}{\langle \sigma_a v \rangle}. \tag{1.17}$$

Considering the abundance observed nowadays, the annihilation cross section would be estimated as :

$$\langle \sigma_a v \rangle \sim 10^{-25} cm^3 s^{-1} \tag{1.18}$$

and, since one has $\langle \sigma v \rangle \sim \alpha^2 / 8\pi m_\chi^2$, the particle mass would be in the GeV and TeV range. This is considered as the main indication that, if a stable particle associated with the electro-weak scale interaction exists, then one can be pretty confident it is dark matter; this is the "WIMP miracle" that justifies all the experimental efforts made in this direction. As already noted, among all the WIMP candidates the most promising one is the *neutralino*.

Neutralino In the MSSM from the mix of the bino $\widetilde{B}$, the wino $\widetilde{W_3}$ and the higgsinos $\left(\widetilde{H}_1^0, \widetilde{H}_2^0\right)$, four Majorana fermionic mass eigenstates come out; these are the *neutralinos* $\widetilde{\chi}_1^0$, $\widetilde{\chi}_2^0$, $\widetilde{\chi}_3^0$ and $\widetilde{\chi}_4^0$. In particular, the first is the lightest one and here is referred simply as χ. As it will be reported in section 1.3.1, the DM search strategies are based on the observation of self-annihilation and elastic scattering with nucleons. The leading channels for neutralino annihilation at low energy, are into fermion-antifermion, gauge boson pairs and final states containing Higgs bosons. On the other hand, the nature of the WIMP interaction with matter can be classified as *Spin-Independent* (SI) and *Spin-Dependent* (SD). Considering an SI WIMP-quark interaction, the cross-section might arise from scalar-scalar and vector-vector couplings in the Lagrangian:

$$\mathcal{L}_{SI} \propto a_q^S \bar{\chi}\chi\bar{q}q + a_q^V \bar{\chi}\gamma_\mu\chi\bar{q}\gamma^\mu q \tag{1.19}$$

where a_q is the WIMP-quark coupling. The presence of these couplings depends on the particle physics model underlying the WIMP candidate.

In particular, here we are dealing with neutralinos, which are theorized to be *Majorana particles*; thus the vector coupling vanishes [46] and the Lagrangian becomes simply:

$$\mathcal{L}_{scalar} = a_q \bar{\chi}\chi\bar{q}q. \tag{1.20}$$

The Feynman diagrams for SI neutralino interactions are shown in figure 1.12. Considering only the scalar contribution, the WIMP-nucleons scattering cross-section is:

$$\sigma_{WN} = \frac{4m_n^2}{\pi} f_{p,n}^2 \tag{1.21}$$

where m_n is the reduced mass of the nucleon and $f_{p,n}$ indicates the coupling constant to protons and neutrons. Extending this result to a nucleus of mass A and Z protons, one has:

$$\sigma = \frac{4m_n^2}{\pi} \left(Z f_p + (A - Z) f_n\right)^2 \tag{1.22}$$

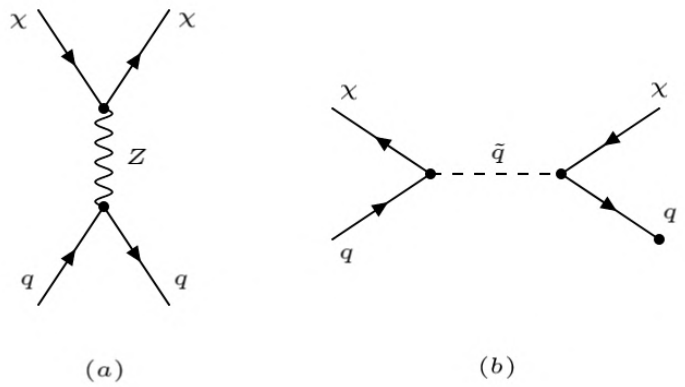

Figure 1.12: Feynman diagrams for neutrino-quark elastic scattering interactions. Here is shown the SI case; however the corresponding SD interaction provides the exchange of an Higgs boson instead of the Z gauge boson.

which is just the sum of the Eq.1.21 over all the nucleons. Under the approximation that $f_p \approx f_n$ the Eq.1.22 reads:

$$\sigma = \frac{4m_n^2}{\pi} A^2 f^2 \tag{1.23}$$

where is highlighted the dependence of the spin-independent contribution to the number of nucleons A. In order to generalize the discussion, the contribution to the cross-section (in case of a Dirac particle) of the WIMP-quark vector coupling is shown. Interestingly, the sea quarks and gluons do not contribute to the vector current, unlike valence quarks. Thus the cross-section reads:

$$\sigma = \frac{\mu_N^2 B_N^2}{64\pi} \tag{1.24}$$

with $B_N \equiv a_u^V (A+Z) + a_d^V (2A - Z)$ and $\mu_N = m_\chi m_N / (m_\chi + m_N)$.
In the most general case, the SI differential cross-section is given by:

$$\left(\frac{d\sigma_{WN}}{dE_R}\right)_{SI} = \frac{2m_N}{\pi v^2} \left[[Z f^p + (A-Z) f^n]^2 + \frac{B_N^2}{256} \right] F^2(E_R) \tag{1.25}$$

where E_R is the recoil energy of the nucleus after the scattering and $F^2(E_R)$ is the nuclear form factor for coherent interactions. With the same assumption made for Eq.1.23, Eq.1.25 becomes:

$$\left(\frac{d\sigma_{WN}}{dE_R}\right)_{SI} = \frac{2m_N A^2 (f^p)^2}{\pi v^2} F^2(E_R) \tag{1.26}$$

The contribution to the SD part of the WIMP-nucleus scattering cross-section arises instead from the coupling with the quark axial current (axial-vector interaction) $\bar{q}\gamma_\mu\gamma^5 q$.

The lagrangian, considering the neutralinos case, is given by:

$$\mathcal{L}_{axial-vector} = a_q^A \left(\bar{\chi}\gamma_\mu\gamma^5\chi\right)\left(\bar{q}\gamma_\mu\gamma^5 q\right) \tag{1.27}$$

where a_q^A is the coupling constant. The cross-section section is given by:

$$\frac{d\sigma}{d|\vec{v}|^2} = \frac{1}{2\pi v^2}\overline{|T(v^2)|^2} \tag{1.28}$$

where v is the WIMP velocity relative to the target nucleus and $T(v^2)$ the matrix element. What should be noted is that for target nuclei with even numbers of protons and neutrons the total spin is equal to 0; thus since the matrix element depends on the total nuclear spin J as:

$$\overline{|T(v^2)|^2} \propto \frac{(J+1)}{J} \tag{1.29}$$

for such nuclei the spin-dependent cross-section vanishes. The differential cross-section results to be proportional to

$$\left(\frac{d\sigma_{WN}}{dE_R}\right)_{SD} \propto \frac{16 m_N}{\pi v^2} G_F^2 \frac{J(J+1)}{J^2} \tag{1.30}$$

In section 1.3 there will be an overview of the main experimental techniques to search WIMPs. Among them, the *direct detection* aims to measure the recoil energy of nuclei which interact with WIMPs trapped in the galactic halo[3]. In this context, the differential rate of expected events is defined as:

$$\frac{dR}{dE_R} = \frac{\rho_0 \sigma_0^N}{2\mu_N^2 m_\chi} A^2 F(q)^2 \int_{v_{min}}^{v_{escape}} \frac{\rho(\vec{v} + \vec{v_{sun}})}{v} dv \tag{1.31}$$

with

$\rho_0 \sim 0.3$ GeV/cm^3	WIMP local density
σ_0^N	WIMP-Nucleon scattering cross-section
m_N	Target nucleus mass
m_χ	WIMP mass
$\rho(\vec{v})$	WIMP velocity distribution (Maxwell-Boltzmann)
$\vec{v} \sim 200$ km/s	WIMP velocity
$\vec{v}_{Sun} = 250$ km/s	Earth velocity with respect to the Sun
$\vec{v}_{escape} = 544$ km/s	Escape velocity from the galaxy
v_{min}	Minimal velocity required for a WIMP to induce nuclear recoil

From a simple comparison between Eq.1.26 and Eq.1.30 it results that the spin-independent contribution scales as the squared number of nucleons (A^2), whereas the spin-dependent part is proportional to a function of the nuclear angular momentum $(J+1)/J$. Although they are both to take into account, the SI component dominates for heavy targets ($A > 20$); this is the case for most of the direct detection experiments (Section 1.3.1) based on targets with Argon, Germanium or Xenon. Figure 1.13 shows the dependency of the differential rate of events from the recoil energy for several heavy target nuclei.

[3]with velocity lower than the escape velocity from the galaxy

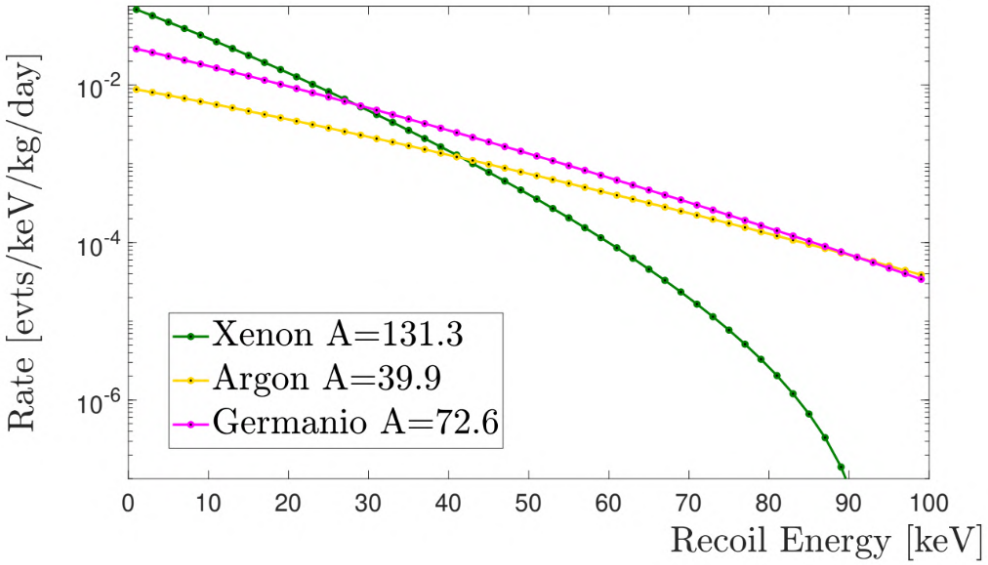

Figure 1.13: Recoil Energy spectra for several target nuclei. The differential rate is expressed in *differential rate units* (dru) which is [events/KeV/kg/days]. The plot was obtained assuming a WIMP mass $m_\chi = 50$ GeV/c^2 and a SI interaction dominant. The simulated data are taken from [47]

The differential rate is a function of the scattering cross-section, and thus a function of the target mass A. It is clear from figure 1.13 (as well as from Eq.1.31) that lighter nuclei are characterized by a lower rate for low energy values. However, the rate depends also on other terms like the form factor, which is responsible for the suppression of the xenon spectrum at high energy. The number of events in an experiment running for a time T is obtained by integrating Eq.1.31 within the detector threshold energies E_{low} and E_{high}:

$$N = T \int_{E_{low}}^{E_{high}} dE_R \epsilon(E_R) \frac{dR}{dE_R} \tag{1.32}$$

with ϵ detector efficiency, which is function of the energy.

Among the dependency of the differential rate, there is the Earth velocity through the dark matter halo given by [48] :

$$v_E = V_\odot + v_\oplus \cos[\omega(t - t_0)] \tag{1.33}$$

where $v_\odot = v_c + 12$ km/s describes the motion of the Sun with respect to $v_c = 220$ km/s which is the local circular velocity (of the Sun around the galactic center). Furthermore, $v_\oplus = 30$ km/s is the speed of the Earth orbiting around the Sun and $\theta \sim 60°$ is the inclination angle between Earth's orbit and the galactic plane; finally the angular frequency $\omega = 2\pi/T$ is defined by $T = 1$y and the phase t_0 results to be June 2, when $v_\odot$ and $v_\oplus$ add up maximally. These details lead to two observational consequences used in the Earth-based experiments. First of all the incident WIMP velocity is different in summer (where $v_\odot$ and $v_\oplus$ are parallel) and in winter (when they are antiparallel) (Figure 1.14), resulting in a harder or softer WIMP spectrum.

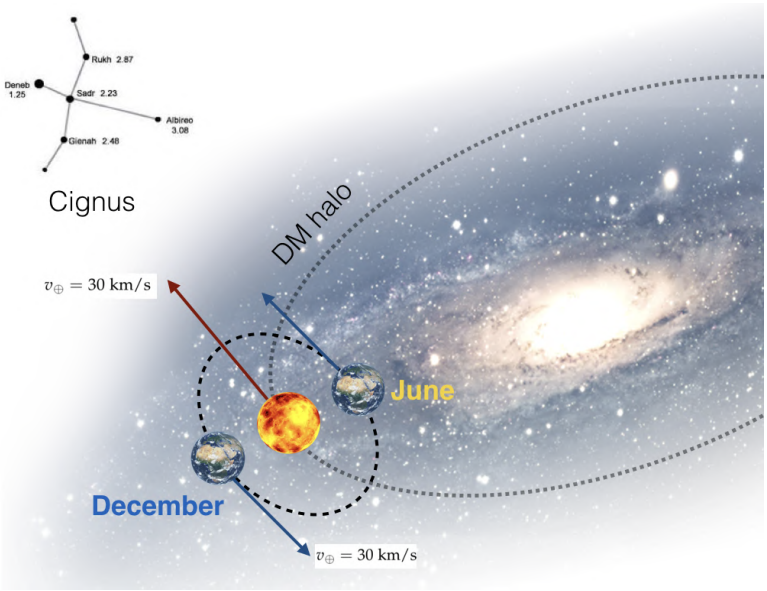

Figure 1.14: Illustration of the Sun-Earth system motion through the DM Halo of the Galaxy. It is also highlighted the direction of $v_\odot$ towards the Cignus constellation.

Thus, a detector can look for a modulated signal; however, in this case, some possible background sources can also show seasonal modulation, e.g, the atmospheric neutrino flux [49]. An even stronger DM signature that can be used to mitigate the background events is the directionality of the "WIMP wind" expected from the constellation of Cygnus; this is due to the fact that $v_\odot \approx v_c$, meaning that the main component of the incident WIMP velocity points towards that direction (Figure 1.14). Thus, since almost all the background is expected to be uniformly distributed, from a track reconstruction one can distinguish a dark matter signal from the background events [50].

1.3 Detection of WIMPs

In recent years, the research in the DM field has seen a rapid increase in both dedicated experiments and scientists involved; it is therefore considered one of the greatest experimental challenges in the history of particle physics. The detection of DM can be addressed with three different approaches: direct detection, indirect detection, and production at colliders (Figure 1.15). The **direct detection** is based

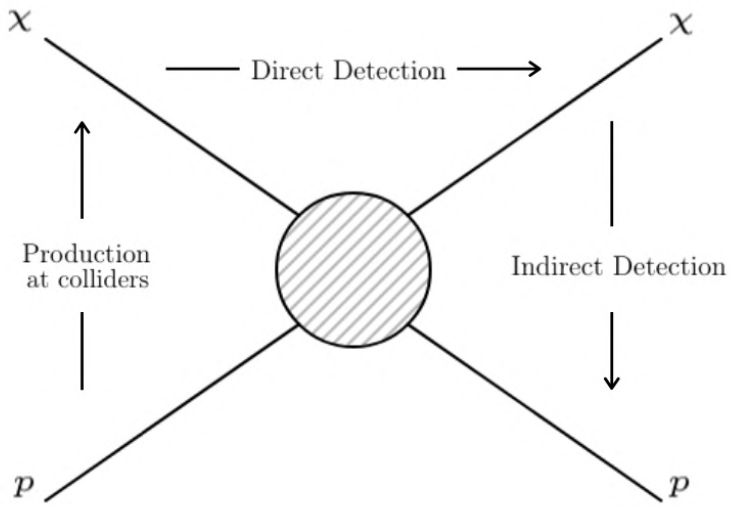

Figure 1.15: In this schematic representation is shown the couplings of a WIMP χ to ordinary matter p, with the corresponding detection technique. The annihilation of DM particles (downward arrow) would give a pair of SM particles (in an LSP model) and this is exploited by the indirect detection technique. On the other hand, the collision of SM particles like electrons or protons at colliders (upward arrow) could produce DM particles. The consequent energy loss is measured. Finally, the elastic scattering of DM off nuclei (rightward arrow) is exploited in the direct detection technique

on the WIMPs scattering off target nuclei; due to the low energy interaction the research is conducted with ultra-low background detector, typically underground (Section 1.3.1). On the other hand, the **indirect detection** searches for DM particles annihilation products inside and outside the galaxy (as gamma rays, X-rays, neutrinos, positrons, and antiprotons) (Section 1.3.2). The DM challenge is increasingly attracting efforts from accelerator experiments with the research of emerging particles produced in high energy collisions with missing energy signature in the reconstructed events. From here on, an overview of the experimental strategies follows.

1.3.1 Direct detection experiments

Based on the collision of DM particles with target materials, the direct detection technique aims to measure the recoil energy of the nuclei. Since this energy is expected to be very low, this technique requires an ultra-low background, achieved by:

- shielding the detector from the environmental radioactivity;
- enhancing the radiopurity of all the detector materials;
- placing the detector underground to reduce cosmic rays background.

Thus, the WIMP detection relies on the ability to recognize and mitigate the background sources. The electrons background comes typically from external gamma radiation or β-decay that can take place in the detector surrounding material. However, there are also background components with nuclear recoil signature like neutrons from radioactivity that can mimic the WIMP signal.
The WIMP-nucleus interaction can result in the production of scintillation light by the de-excited nuclei, in the production of charge by the ionization of atoms or heat. There are detectors that can use one of these signals, or a combination of two in order to disentangle WIMPs from background recoils, as illustrated in Figure 1.16. Depending on the choice of the signal detection technique a variety of target

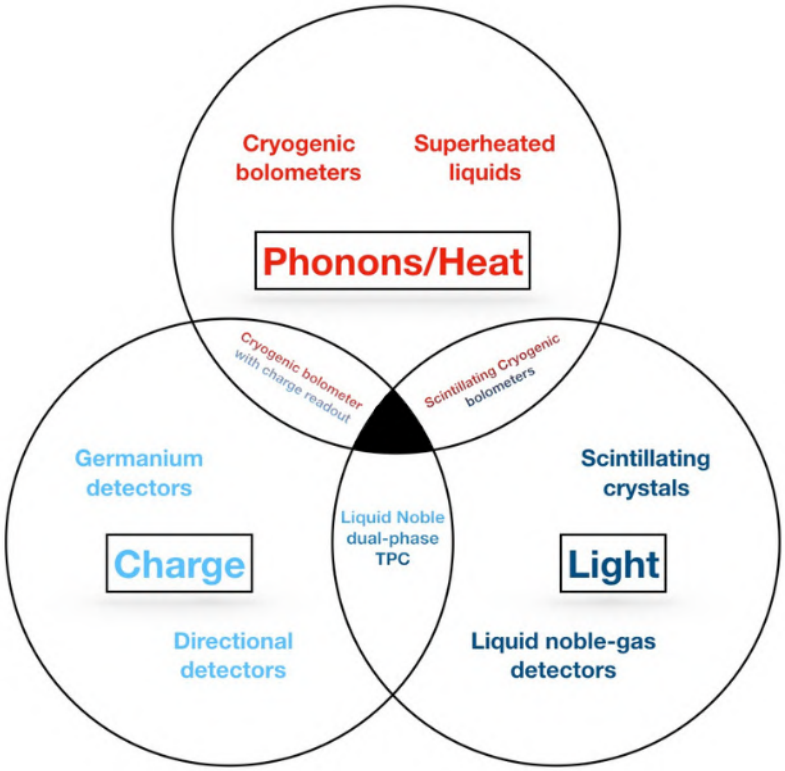

Figure 1.16: Schematic of the three possible signals emerging from the WIMP-nuclei interactions on which the direct detection technique is based. In addition, are also shown the detectors capable of detecting the individual signals and those which use a combination of two of them. The black area means that so far, no attempt to measure all three channels simultaneously in one detector was successful.

material are employed in the direct detection experiments. Another dark matter signature already mentioned could be an annual modulation signal due to Earth's motion through the galactic halo in which the WIMPs are supposed to be trapped.

Inorganic crystal detectors The first experimental attempt of DM direct detection, born from the suggestion of Goodman and Witten, belongs to this class of detectors [51]. The detector prototype [52] used high purity Germanium (HPGe) crystals to search dark matter-induced signals. Since the amount of energy required to create the electron-hole pair in such semiconductor detectors is very small (for the Ge is ~ 2.9 eV and for Si is ~ 3.6 eV), the charge yield results to be very large, ensuring a good energy resolution; however they are very sensitive to the electronic noise and to solve this it would be necessary to go down to cryogenic temperatures, which is very difficult to do for massive detectors. Current state-of-the-art experiments use kg of Ge, at liquid nitrogen temperature, and are based on a passive reduction of the background with the so-called *Point Contact Germanium* detectors; this kind of detectors can reach very low energy thresholds. The **CoGeNT** experiment [53] exploited this technique and was designed to look for WIMP candidates in the low mass range (~ 10 GeV/c^2); with a modest statistical significance ($\sim 2.2\sigma$) the experiment claimed the observation of an annual modulation in its data. Even if the DM interpretation of this excess was soon discarded, a similar situation occurred with another experiment, albeit with a different design: the **DAMA/LIBRA** experiment [54]. The latter, operating at Laboratori Nazionali del Gran Sasso (LNGS), underground laboratory in Italy, employs about 250 kg of highly radio-pure NaI(Tl) crystals. The advantage of such kind of detectors which exploits only the *scintillation light*, is their rather simple design, which can be operated stably for long periods. Furthermore, recalling Eq.1.26, the high mass number of I ($A = 127$) leads to high sensitivity to spin-independent interactions. Experiments based on this technology mainly search for an annually modulated signal over a flat background as DM signature. Over time DAMA has reached a statistical significance of 12.9σ for a DM-like signal annually modulated [55]. By giving an interpretation to this signal, according to the standard halo model, two possible solutions have been proposed:

- a WIMP with $m_\chi \simeq 50$ GeV/c^2 and $\sigma_\chi \simeq 7 \cdot 10^{-6}$pb;
- a WIMP with m_χ in the 6 - 16 GeV/c^2 range and $\sigma_\chi \simeq 2 \cdot 10^{-4}$pb.

One of the first argument against the analysis made over 14 annual cycles was that the amplitude of the annual modulation showed to decrease with time [56]. However, the results also disagree with the ones published by other experiments using different detection techniques and targets. The last few years have seen a growing number of projects using the same detection strategy as DAMA, like **COSINE** [57] and **SABRE** [58]; the latter plans to run NaI(Tl) immersed in liquid scintillator. To detect the shift in phase of the annual modulation, two setups are located in each hemisphere (one at LNGS and one in the underground laboratory site STAWELL in Australia).

Cryogenic detectors Cryogenic bolometers allow for the detection of the heat signal in the form of phonons by measuring the increase of temperature following the WIMP-nucleus interaction. The sensibility is given by [48]:

$$\sigma^2 = c_1 kT(TC + c_2 E) \tag{1.34}$$

with c_1, c_2 detector-specific constants. Eq.1.34 shows a dependence on the operation temperature T and on the detector heat capacity (which is a function of the temperature). Thus, to optimize the sensitivity, the detector operates at cryogenic temperatures. Dielectric crystals (again Ge and Si) are usually employed since their heat capacity is proportional to $C \propto M \times T^3$ (at cryogenic temperature) where M is the detector mass. A detection strategy for the small temperature variations ΔT is based on the use of *transition edge sensors* TES which consist of thin tungsten wires operating at the transition temperature between the superconducting and normal-conducting state; small temperature increase have a strong influence on the resistivity and thus on the running current. In order to accomplish a signal/background discrimination in the WIMP search, all modern cryogenic experiments follow a two-channel approach, combining the phonon readout technique and a second channel that could be ionization or scintillation.
The **Cryogenic Dark Matter Search** (CDMS) is a series of experiments designed with a cryogenic bolometer with additional charge readout. In 2013 CDMS-Si [59] reported the observation of 3 WIMP events, with a rejection of the background hypothesis with 99.8% significance; however, the results have not been confirmed in subsequent experiments of the same collaboration (i.e. CMDS-II and SuperCDMS [60]).
The cryogenic experiment **CRESST** [61] at LNGS, uses scintillating crystals as detector exploiting light from scintillation as the second channel. In 2011, with a significance level close to $\sim 5\sigma$, the experiment observed an excess of events in the low mass range (around 10 and 25 GeV/c^2); however, it turned out to be due to a missing contribution in the assumed background model [62]. Somewhat all these cryogenic experiments are now turning all their efforts towards an operation mode which gives up the discrimination in the face of decreasing their thresholds to access to low mass WIMPs (< 10GeV/c^2) [46]; this is also due to the overwhelming progress for liquid noble gas detectors for WIMP masses above 10 GeV/c^2. As one can easily see from Figure 1.17, which shows the upper limits to the WIMP cross-sections and mass, in case of SI interactions, the current ones for low mass WIMPs[4] are rather high; a significant improvement does not need a large detector mass[5].

The orange area in figure 1.17 is delimited by the *neutrino floor* which is a lower limit due to the irreducible background rate from solar neutrinos elastic scattering off target nuclei. In order to overcome this limit in the 7 GeV/c^2 region a detector mass of 200 kg is required and this is the direction that SuperCDMS at SNOLAB is taking. A variant of the detectors treated so far worth mentioning is the one that uses superheated liquids, usually refrigerants such as CF_3I, C_3F in bubble chambers; in these setups, the liquids are kept at a temperature just below the boiling point and operate as threshold detectors. Using this technology, the PICO experiment has reached the best sensitivity worldwide for spin-dependent couplings at all WIMP masses [46, 63].

[4]The plot shown in figure 1.17 is not up to date, but the state of the art in the low mass region is not changed so much since 2017. A more recent plot will be shown later.

[5]the current limits for a 3 GeV/c^2 WIMP are 5 orders magnitude higher than at 30 GeV/c^2 and a detector mass of 100 g is enough to gain in sensitivity [46]

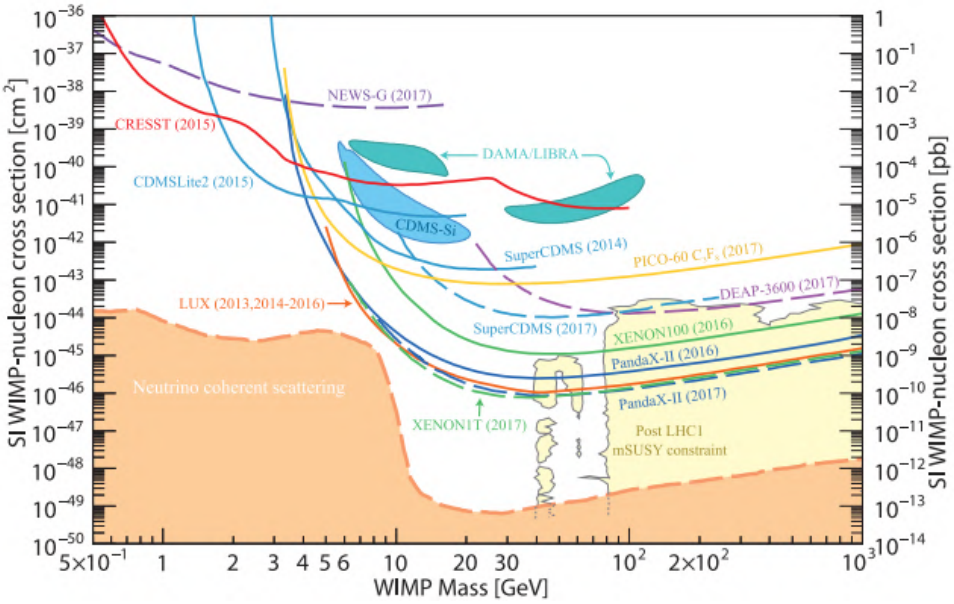

Figure 1.17: Limits on the WIMP cross-section for spin-independent coupling versus mass [46]. These plot dates to 2017 and a more updated one will be shown in the next section. What is interesting in this plot are the DAMA/LIBRA and the CDMS-Si area of possible signal events. Furthermore is also interesting the neutrino limit region trend for low WIMP masses.

Noble liquid detectors Noble liquid gas (Xe, Ar) detectors have achieved the most stringent constraints on "high mass" WIMPs (above 10 GeV) interactions. These noble gases are excellent scintillators and can be ionized easily. Krypton and Neon are avoided for different reasons; the former, although it has the same properties of Xe and Ar, has a high intrinsic background from its long-lived isotopes. Neon instead has a low mass number and its functionality would be limited to the low-mass region. Since the XENON experiment [31, 64], which is based on these kinds of detectors, represents the main topic of this work, a detailed description of both the Xe properties and the detection principles deserves a dedicated section (Section 2). In summary, one can say that dual-phase (liquid and gas) Time Projection Chamber (TPC) detectors allow for the simultaneous measurements of the primary scintillation and the ionization electrons drifted through the liquid. This combination allows for discrimination between nuclear and electron recoils as well as for 3D position reconstruction within the detector. This detection strategy is employed by XENON [1, 65], LUX [30] and PandaX [66] experiments with the Xe, and by DarkSide50 [67] with Ar. The worldwide best result comes from the XENON1T [1] experiment which sets the cross-section limit for SI interactions with a minimum of 4.1×10^{-47} cm^2 at for a WIMP mass of 30 GeV/c^2. One of the best features of these detectors is the relatively easy scalability; thus future multi-ton LXe experiments as XENONnT (Section 2.4), LUX-Zeplin (LZ, upgrade of LUX) [68], and DARWIN are expected to improve the sensibility by up to three orders of magnitude (Figure 1.18).

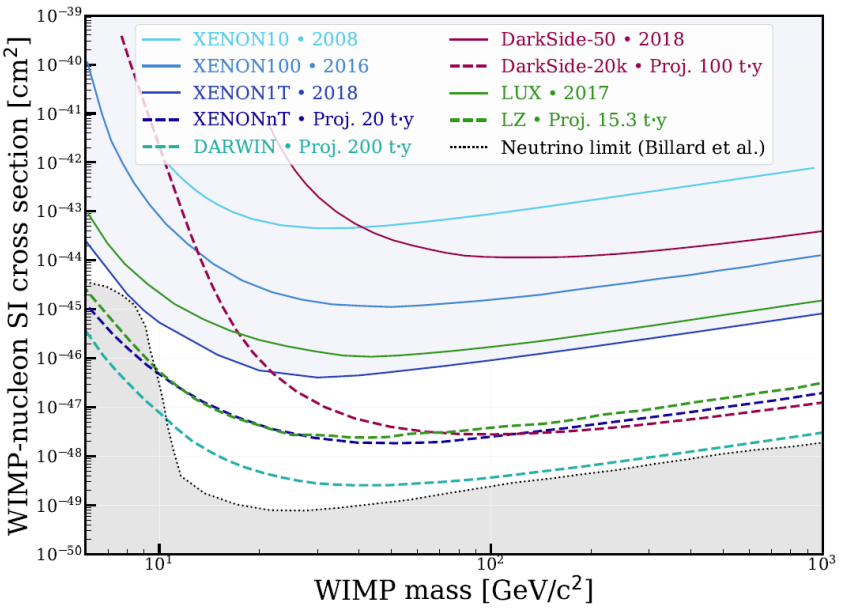

Figure 1.18: Current limits on the spin-independent cross-section for WIMP-nucleus interaction. In this plot are shown only the dual-phase TPC detectors. The excluded parameter space is highlighted in blue and is defined by the best exclusion limit set by XENON1T [1]. In addition, the projections of future results with noble liquid detection strategy are shown. The gray area marks the neutrino limit. Plot from [69].

1.3.2 Indirect detection experiments

The indirect detection technique is based on the detection of the annihilation products of WIMP that can occur in DM high-density regions; products of their annihilation include neutrinos, gamma rays, positrons, antiprotons, and antinuclei. Depending on the nature of the particles searched, different detection techniques are employed. These methods are complementary to direct detection since they are able to explore higher masses and different regions of the DM parameter space. Regarding the indirect detection, both monoenergetic photons from WIMP annihilation in space as well as GeV neutrinos coming from the center of the Sun or the Earth are considered "*smoking gun*" signals; the latter would be a clear evidence of WIMPs being slowed down, captured and trapped in celestial objects, enhancing their density and annihilation probability.

y-rays probe Gamma rays could be produced by WIMP annihilation that can occur in a variety of ways; among them, direct annihilation to gamma rays and internal bremsstrahlung (Figure 1.19) yield spectral feature that could constitute signal impossible to explain by other means than Dark Matter. These signatures have to be compared to the common power-law features of conventional astrophysical gamma-ray sources. In the energy range between about $\sim$ 100 MeV and several 100 GeV, gamma rays are observed by pair-conversion inside tracking detector and electromagnetic calorimeter on satellites. The main experiments in this area are **EGRET** [70] and **Fermi-LAT** [71]. The size of the signal depends strongly on the halo model, but of course the most prominent is expected near the Galactic Center

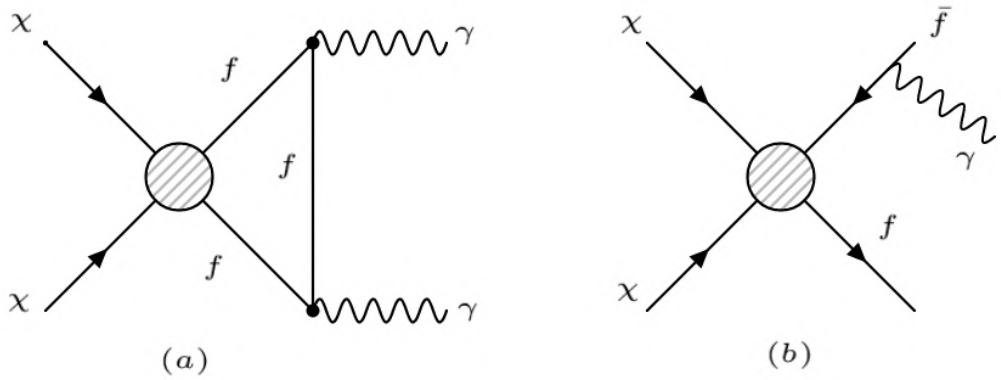

Figure 1.19: Feynman diagrams for direct annihilation into photons (left) and internal bremsstrahlung (right). For both diagrams f are SM fermions.

(GC) [72]. However discovering a WIMP signal in this channel is complicated due to the presence of unexpected background; indeed, Fermi-LAT data revealed the extended source of GeV photons near the GC, the so-called *Fermi Bubbles* [72]. Despite the difficulties faced by the experiment, the data claimed excess of events in the few GeV range around the GC consistent with most of the WIMPs interpretations. Due to the strong dependency of the analysis from the fit model, Fermi-LAT did not claim a signal but used these data to constrain the contribution from WIMP annihilation. Complementary to the observation with space telescopes there are the ground-based experiments which exploit the Cherenkov light produced by the shower originated from the interaction of primary γ with the atmosphere. The *Imaging Air Cherenkov Telescopes* (IACTs) currently running are **MAGIC** [73], **VERITAS** [74] and **HESS** [75]; finally the new generation telescope **CTA** [76] is also planned. Figure 1.20 shows the current limits and the projections on the cross-section of WIMP annihilation $\chi\chi \to b\bar{b}$. The strongest limits were obtained by a combined analysis of dwarf galaxies made by Fermi-LAT and MAGIC [77].

Charged cosmic-ray probe Anti-proton and positron channel constitutes the main signature for DM from charged cosmic rays. Anti-particles are very rarely produced in secondary processes and even a small addition of anti-particles produced in WIMP annihilation could give rise to a detectable signal with a much less astrophysical background. What is generally observed is the positron-to-electron or the antiproton-to-proton ratio in order to cancel systematics which should affect particles and antiparticle similarly. Anomalies using charge cosmic rays as probes are searched with ballon-type detectors, ground-based telescopes (**Pierre Auger Observatory** [78], **Telescope Array** [79]) and experiments on satellites such as **PAMELA** [80], **AMS-02** [81] and Fermi-LAT. An excess of high-energy positrons over the standard secondary production from inelastic cosmic-ray interactions has been established by several experiments; the highest statistics were reached by AMS-02 [82]. The excess has been ascribed to DM annihilation even if it could be explained by astrophysical sources due to the impact of the magnetic field configuration in the positron trajectories. More recently the antiproton flux measured by AMS-02 shows feature referable to DM annihilation; the robustness of

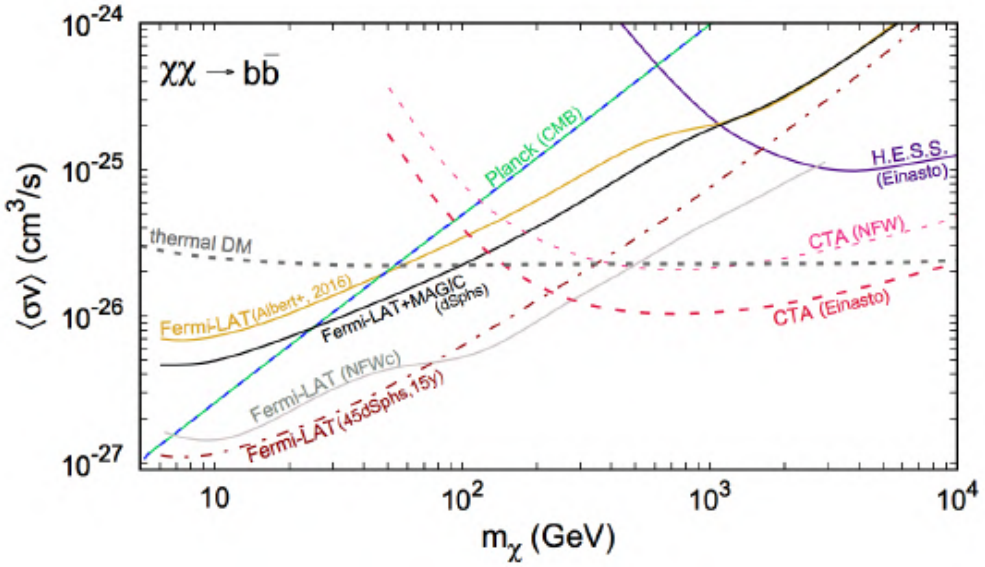

Figure 1.20: Limits on the cross-section for DM particles annihilation in the $b\bar{b}$ channel. The strongest limit is set by FERMI-LAT [71] and by the combined analysis with MAGIC [77]. In this plot are shown also the future projections from the CTA collaboration.

such claim is limited by all the systematic uncertainties in cosmic rays production and transport [83]. Finally, antinuclei, such as anti-deuterium and anti-helium, could provide information on DM annihilation or decay. Using these probes would grant a high signal-to-noise ratio since the kinetic energy of antinuclei from the hadronization of DM-initiated jets is not forced to high value from baryon number conservation, as instead occur for antinuclei produced in inelastic CR processes. Thus the detection of a single low-energy antinucleus would have a considerable impact on the WIMPs search.

Neutrino probe The DM captured in celestial bodies such as the Sun, the GC and Earth itself can annihilate or decay, and produce Standard Model particles. The amount of DM accumulated in this way depends of course on the DM model, the DM mass, the incident flux on the celestial body considered and the DM-nuclei scattering cross-section. The SM annihilation products are trapped inside the celestial body causing its heat up[6]. A different fate lies with neutrinos that escape and can reach detectors, providing a unique signature. For this detection, water Cherenkov telescopes as **ANTARES** [84], **IceCube** [85], and **SuperKamiokande** [86] are employed. Currently they are able to provide the most stringent constraint on WIMP-nucleon SD cross-section under limits on the neutrino flux for DM annihilation from the Sun. Improvements are expected from planned neutrino telescope as HyperKamiokande [87] and KM3Net [88].
The **Super-Kamiokande** detector (Figure 1.21) is the world's largest imaging water Cherenkov detector operating for more than 20 years since 1996. Located in the Kamioka mine in Japan, Super-K has provided many clues in the experimental

[6]From the comparison with heat production models in planets, anomalous warming can give constraint on the DM trapping.

understanding of neutrino's physics and eventually led to the discovery of neutrino oscillations in 2001 [89].

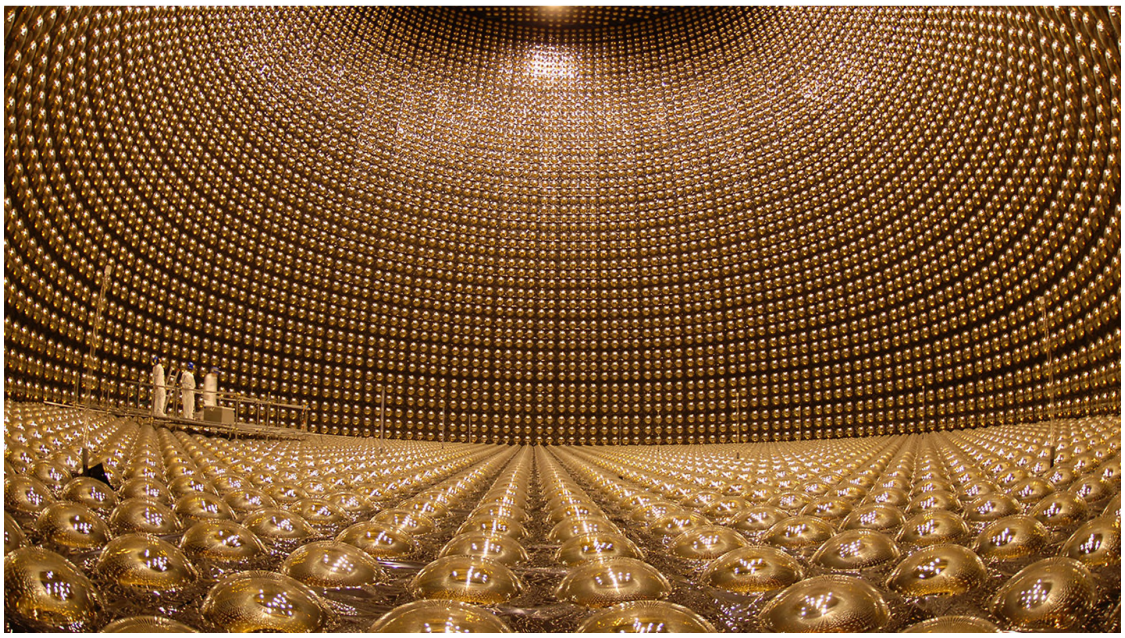

Figure 1.21: Internal view of SuperKamiokande [86] water Cherenkov detector with its 11.146 photomultiplier tubes immersed in 50 kton of pure water.

The detector is also able to search indirectly DM through the detection of upward-going-muons excess; these muons would be generated by interaction with the surrounding rock of muon neutrinos from the DM annihilation in the Sun. Up to now, no significant excess over the expected background has been found. Recently, for the SK-Gd upgrade, was proposed the introduction of gadolinium (Gd) ions (at 0.2% loading) into the detector to enhance the neutrons capture efficiency giving both a handle on antineutrinos through inverse beta decay, and the possibility of a background reduction. The Gd properties are discussed in section 3.1 since the XENONnT Neutron Veto takes its cue from the Super-K system as well as from the EGADS (Evaluating Gadolinium's Action on Detector System) prototype [90–92].

1.3.3 The pursuit of dark matter at colliders

In most DM scenarios, the energy scale expected for WIMP coupling and mass overlaps with the electro-weak symmetry breaking scale. Therefore high energy colliders, LHC in particular, are viable experimental venues for DM detection being able to produce dark matter and to probe most basic DM–matter interactions. They are subjected to different systematic uncertainties, thus can be considered a useful complementary dark matter search strategy. The models used for the interpretation of the constraints on production cross-section imply the discovery of two particles: the dark matter particle and the mediator one. Thus, collider dark matter searches can be broadly distinguished into two categories: searches in final states with and without dark matter itself. In both cases, the DM signature in hadron collisions would be a large amount of missing energy associated with

the discovery of one or more visible particles, in a channel characterized by highly energetic jets or leptons. An interesting signature occurs when the WIMP pair is boosted in an opposite direction with respect to the visible particle(s); this leads to the *mono-X* signature (Figure 1.22).

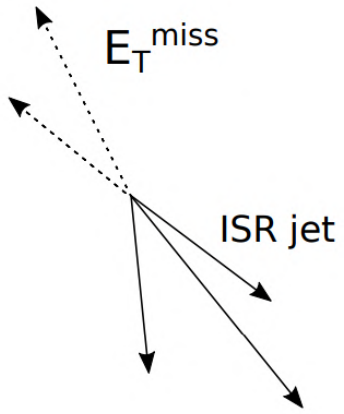

Figure 1.22: The mono-X signature. The generated WIMP pair is boosted into the same direction but opposite to the visible initial state radiation (ISR).

The angle between the missing energy beam and the visible one is $\Delta\phi(\not{E}_T, X) \approx \pi$. Here X can be a multitude of particles such as γ, g, q, W, Z, H, and others. While collider constraints are not competitive with those from direct detection for the spin-independent WIMP-nucleon interaction, interpretations of LHC signals in terms of spin-dependent cross-section, assuming an axial-vector mediated model, are more powerful over a wide range of WIMP masses [93].

Chapter 2

The XENON project

The XENON project aims to detect the interaction of dark matter elusive particles within a xenon dual-phase time projection chambers (TPCs). The project is hosted at the Laboratori Nazionali del Gran Sasso (LNGS), in Italy, which is the largest underground laboratory of the world under 3600 m.w.e. of rock. Since its birth, it has undergone several phases consisting of the upgrade of the detectors used. An initial search was performed with the XENON10 detector [94], installed in 2005, where 14 kg out of 25 kg of xenon were used as the active target. Already with this phase, conceived to test the feasibility of the dual-phase detector in the dark matter field, it turned out to be competitive worldwide establishing the best upper limits on both SI and SD WIMP-nucleon cross-section. The support of the good results achieved led to the planning of a larger detector, XENON100 [31], based on the same detection principle but with an active mass of 62 kg. Although no evidence of DM has been found, once again the experiment has published the best limit for both types of interactions in 2012. The XENON100 phase represented a very important step since it allowed us to investigate also other physics; among these, it is worth mentioning the search for axions, for leptophilic dark matter, for low mass WIMP and the research of an annual modulated signal. All of this paved the way for the next generation of multi-ton scale detectors with XENON1T [65] (Section 2.3), which contained 2.0 t of active mass, and with the XENONnT upgrade under construction, that will host 8 t of LXe mass, 6 t of which contributing to active mass. All the results achieved by XENON detectors for the constraint on the WIMP-nucleon interaction cross-section are summarized in Table 2.1.

Phase	σ_{SI} [cm^2]	σ_{SD}(neutron) [cm^2]	WIMP mass [GeV/c^2]
XENON10 [95, 96]	4.5×10^{-44}	5×10^{-39}	30
XENON100 [97, 98]	1.1×10^{-45}	2.0×10^{-40}	50
XENON1T [1, 99]	4.1×10^{-47}	6.3×10^{-42}	30

Table 2.1: Results, in the form of minimum of the WIMP cross section limits for SI and SD interaction, obtained by the various XENON phase. The corresponding WIMP mass is also reported.

Figure 2.1 shows the limit curves obtained by the XENON100 and the XENON1T phases. In this chapter the detection principle used in the XENON project is drawn

with particular regard to the of XENON1T (Section 2.3) and XENONnT (Section 2.4) experiments.

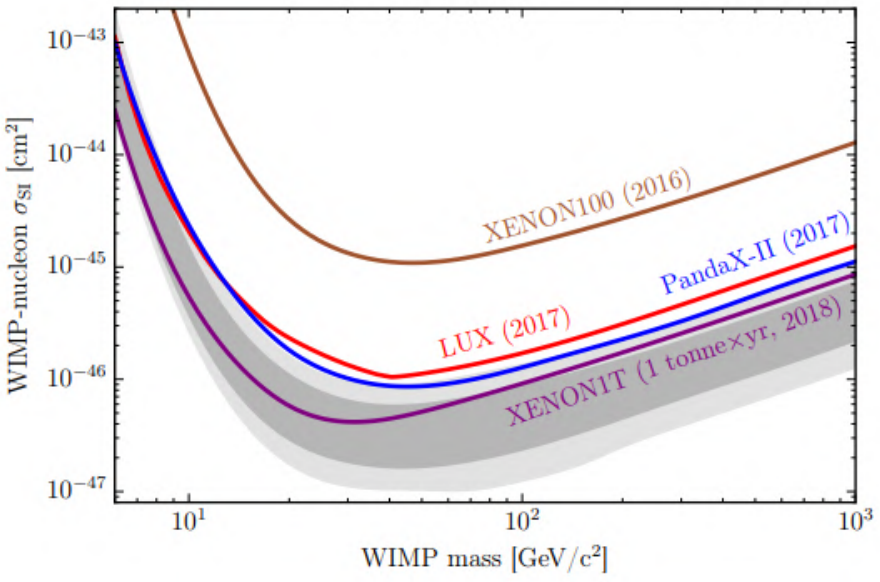

Figure 2.1: Exclusion limits from different dark matter experiment among which the XENON100 and XENON1T experiment. The results from a one tonne-year exposure of XENON1T are shown [1].

2.1 Detection with a xenon dual-phase TPC

In the XENON experiment, the WIMP detection principle is based on a *dual-phase Time Projection Chamber* consisting of xenon in the liquid phase (LXe) and, above it, a small gap of gaseous xenon (GXe). In Section 2.1.1 the main xenon physical properties are discussed, while in Section 2.1.2 the detection principle is explained.

2.1.1 The choice of xenon as target

Using LXe as active target in the context of DM direct detection has a number of advantages. First of all, its high atomic number $A = 131$ ensure, with respect to the other noble-gases, higher interaction rate for WIMP-nucleus interaction (for low energy recoil, in particular, see Figure 1.13), due to the spin-independent cross-section, which is proportional to A^2 as expressed by Eq. (1.26). Additionally, the natural xenon isotope composition shows several features worth mentioning. Table 2.2 shows all the known Xenon isotopes; with the exception of the artificial ones, all isotopes are stable or with very long-lived.

^{A}Xe	Abundance (%)	Half-life	Decay mode
^{124}Xe	0.095	1.8×10^{22} y	ECEC
^{126}Xe	0.089	stable	
^{128}Xe - ^{132}Xe	80.3	stable	
^{134}Xe	10.43	stable	
^{136}Xe	8.8	2.2×10^{21} y	$\beta\beta$

Table 2.2: Natural xenon composition. Only two of the natural isotopes are unstable but with half-life greater the age of the Universe.

Indeed, ^{136}Xe is radioactive and is a potential candidate for $2\nu\beta\beta$ decay searches; this type of decay, being characterized by a $\sim 10^{21}y$ half-life [100], has a rate of events low enough to not interfere in the search for DM search. However, its contribution to the ER background could become significant by switching to a detector with a larger mass as in the case of XENONnT. The ^{124}Xe isotope instead, decays via $2\nu ECEC$ (two-neutrino double electron capture), which is a second-order weak-interaction process with half-life $\mathcal{O}(10^{22}$y) that surpasses the age of the Universe (Figure 2.2); this decay was directly observed in the XENON1T detector [101].

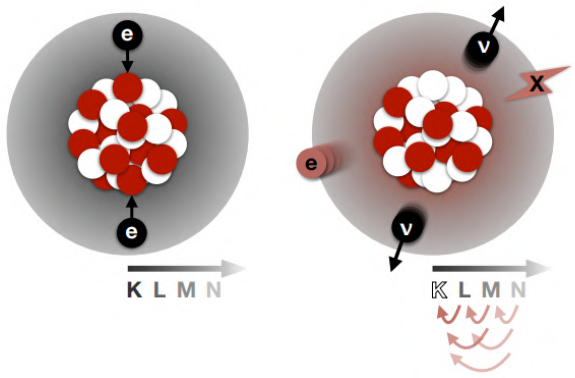

Figure 2.2: The 2νECEC process consists of a nucleus that captures two atomic shell electrons (black), most likely from the K-shell, and simultaneously converts two protons (red) into neutrons (white). Two neutrinos (black) are thus emitted in the nuclear process, which carry away most of the decay energy while the atomic shell is left in an excited state with two holes in the K-shell. A cascade of X-rays (red X) and Auger electrons (red e) are emitted in the atomic de-excitation.

Furthermore the presence of two isotopes with non-zero spin as the ^{129}Xe (spin 1/2) and ^{131}Xe (spin 3/2) allows to investigate spin-dependent interactions. Other xenon properties are:

- its high charge number $Z = 54$ implies a high stopping power and in general, a *self-shielding power* against the external background;
- its high density $\rho = 2.96$ g/cm^3 allows for building compact detectors with large active mass;

- considering that its boiling point is at 178K (at a pressure of 2 bar), it does not require a complex and dispensing cryogenic system.

Finally, xenon acts both as an excellent scintillator, since it emits about 5×10^7 photons per keV deposited, and as a good ionization medium, yielding $\sim 6 \times 10^7$ electron-ion pairs per keV. Thus an interaction produces a relatively large amount of both charges and photons. Furthermore, xenon is also transparent to its own scintillation light, which is emitted with a wavelength of $\lambda = 177.6$ nm; thus, since λ is in the sensitive region of the PMT installed in the TPC, there is no need to use wavelength shifters, which can lead to a worst resolution[1]. Speaking about the scintillation mechanism in liquid xenon, it is ruled by de-excitation of the excited dimers Xe_2^* produced after recoil events through two different processes: *direct excitation* or *recombination* of ionization products. In the first case one starts with an excited xenon atom (Xe^*) followed by the scintillation process:

$$\begin{aligned} Xe^* + Xe &\rightarrow Xe_2^* \\ Xe^* &\rightarrow 2Xe + h\nu \end{aligned} \tag{2.1}$$

The second case instead involves ionized xenon atoms Xe^+.

$$\begin{aligned} Xe^+ + Xe &\rightarrow Xe_2^+ \\ Xe_2^+ + e^- &\rightarrow Xe^{**} + Xe \\ Xe^{**} &\rightarrow Xe^* + \text{heat} \\ Xe^* + Xe + Xe &\rightarrow Xe_2^* + Xe \\ Xe_2^* &\rightarrow 2Xe + h\nu \end{aligned} \tag{2.2}$$

The transparency to the emitted radiation is due to the different configuration of energy levels of dimers and atoms.

2.1.2 Working principle of the Xe dual-phase TPC

A dual-phase time projection chamber detector allows the independent measurement of light as well as charge signals. The detector consists of a cylindrical vessel made of PTFE to ensure high reflectivity, with the top and bottom surfaces covered with Photomultiplier Tube (PMT) arrays, and it is filled with LXe up to a certain level and with the GXe above. A schematic of the detector and the signal production is illustrated in Figure 2.3. An incident particle releases energy in the form of LXe recoil. Thus a light signal and ionization electrons are produced according to Eq.(2.1) and Eq.(2.2); the light signal, which is referred to as S1, is promptly detected by the two arrays of PMTs. On the other hand, the presence of a uniform drift field E_{drift}, generated by two meshes called *cathode* (set at negative potential) and *gate* (set at ground potential), tends to separate a fraction of the created electron-ion pairs[2]. The electrons follow the field lines until they reach the

[1] This feature can not be exploited using liquid Argon where the scintillation light is characterized by a $\lambda = 128$ nm. In that case (*e.g.* in DarkSide-50 [67]) wavelength shifters are employed to convert λ into a wavelength range detectable by the PMTs.

[2] while the other fraction tends to recombine, contributing to the S1 signal

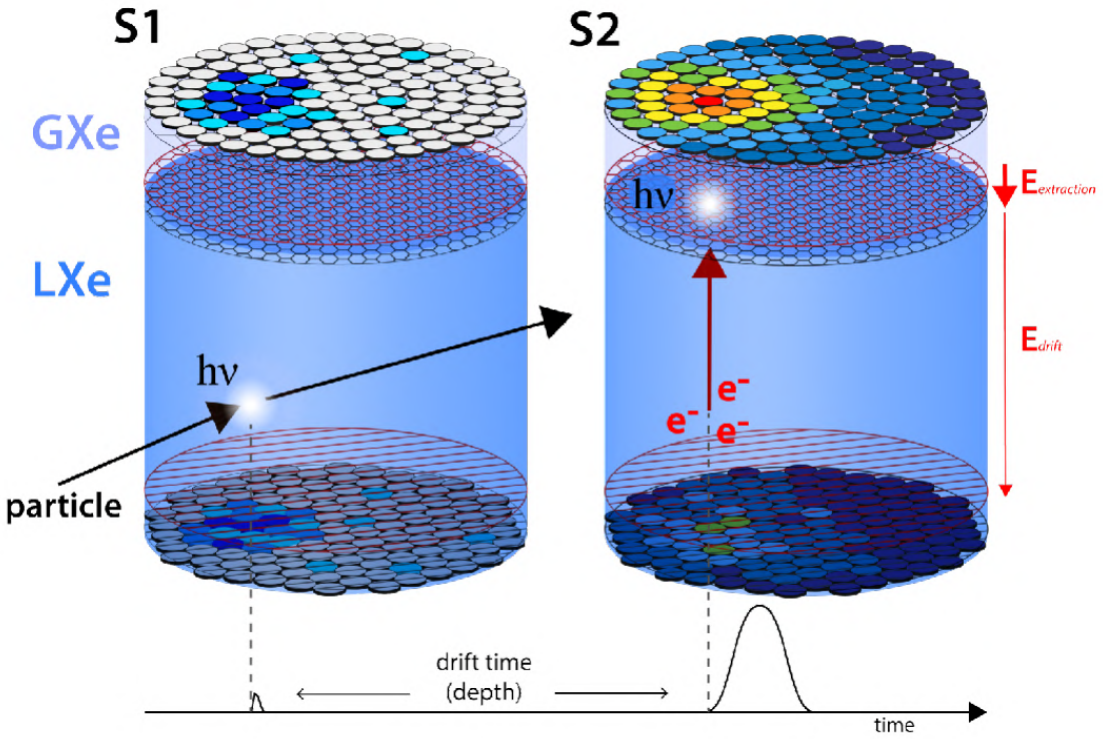

Figure 2.3: Working principle of a xenon dual-phase TPC. After the interaction of a particle inside the active volume a first prompt light signal S1 is produced (left) followed by the delayed one, called signal S2, that is caused by the charges in the GXe. Exploiting the drift time and the hit pattern on the PMT array, a 3D reconstruction is possible.

gate, where they are extracted from a second stronger electric field $E_{extraction}$ $\mathcal{O}$(10 kV/cm) between the gate mesh and the anode (at positive potential); this field accelerates the electrons in the GXe where proportional scintillation occurs. The light signal, delayed by the electrons drift time, is referred to as S2. All the steps described are summarized in Figure 2.3. Once the drift velocity of the electrons is obtained by measuring the time difference between the S1 and the S2 signals, it is possible to calculate also the z-coordinate of the interaction point. On the other hand, the (x, y)-coordinates of the event are determined from the hit pattern of the S2 signal in the top PMT array. Thus the TPC allows for a full 3D position reconstruction. In addition, the self-shielding property of xenon is exploited to define the so-called *Fiducial Volume* (FV); it is defined as the inner volume used for reconstructing the position of the interaction. The FV definition leads to a remarkable reduction of the background whose majority of the events are expected at the edge of the TPC (Section 2.2). The combined analysis of the S1 and S2 signals not only allows us to reconstruct the energy of the event but also allows us to discriminate between the two different recoil processes of the xenon atoms. The **Electron Recoil** (ER) is linked to γ- and β-particles that scatter off the electronic shell of the atoms, while the **Nuclear Recoil** characterizes the interaction of heavier particles, such as WIMP or neutrons, with the nucleus itself. The importance of the discrimination between the two components is therefore evident since WIMPs are expected to produce NRs while most of the background produces ERs. The

different signatures of ER and NR emerge from the ratio between S2 and S1 signals:

$$(S2/S1)_{NR} < (S2/S1)_{ER}\,. \tag{2.3}$$

This is due to the different stopping power (dE/dx) of the particles involved; thus, in an NR the recombination rate is higher with respect to the ER situation and the recombination process contributes to S1. The discrimination between ER and NR is achieved through the identification of the corresponding bands as shown in Figure 2.4. The different background sources with the corresponding mitigation strategies are the topic of the next section.

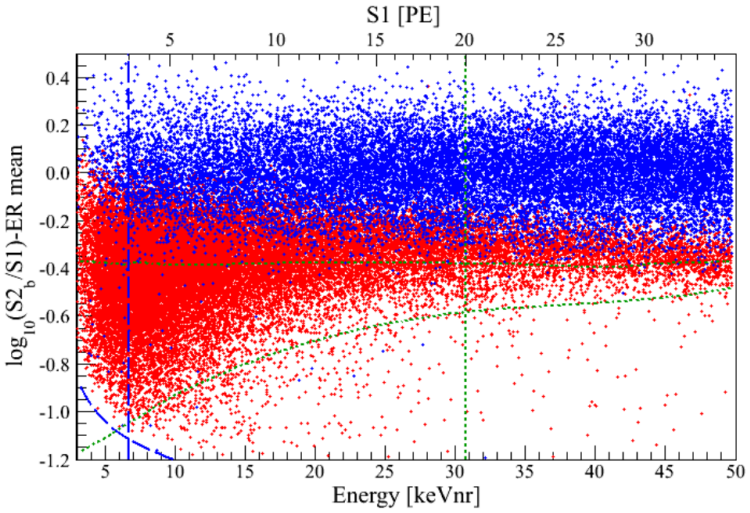

Figure 2.4: Discrimination of nuclear and electronic recoils achieved with the XENON100 experiment [31]. On the y-axis is reported the S2-to-S1 ratio; a smaller ratio is associated with NR (red dots) while higher values with ER (blue dots). Commonly the y-axis is shifted with respect to the mean of the ER band.

2.2 Background sources and reduction

In the dark matter search, a low rate of events is expected. This requires, in addition to having a detector with a large target mass, the best possible sensitivity, achievable by reducing the background. This operation is crucial and comes in parallel with the complete characterization of the background itself. The known sources of background in LXe based detectors are listed in Table 2.3.

Background component	Source	Recoil type
Environmental γ-radiation	^{137}Cs ^{40}K ^{60}Co U/Th decay chain	ER
Muons	Cosmic Rays	ER, Target Activation[3]
Cosmogenic neutrons	CR spallation	(multiple) NR
Radiogenic neutrons	(α, n) reactions Spontaneous Fission	(multiple) NR (multiple) NR
Neutrinos	Solar Diffuse supernovae (DSN) Atmospheric	ER/NR NR NR
Internal background	^{85}Kr (β, γ) ^{222}Rn (α) + daughters (β, γ) ^{136}Xe $(2\nu\beta\beta)$	ER

Table 2.3: Common background sources in xenon underground detectors for DM with signal released in the detector. Table from [102].

It is useful to distinguish between:

- Internal background;
- Intrinsic background;
- External background.

Internal background The internal background refers to the detector materials radioactivity. The most dangerous radiogenic nuclides that lead to γ emission come from the ^{238}U and ^{232}Th chains and from the decay of ^{40}K, ^{60}Co and ^{137}Cs which can be found in the PMTs materials or in Stainless Steel (SS). It is known that photons' interaction with matter depends on their energy. Low energy photons $\lesssim \mathcal{O}(100\text{keV})$ can contribute to the ER background via their photoelectric effect, while Compton scattering is more likely to occur for higher energies up to several MeV; finally the pair production mechanism dominates at higher energies [46]. All three processes lead to the release of energy within the xenon and to a recoil signal in the keV range which overlaps to the *Region Of Interest* (ROI) of the WIMP search. The latter is typically below 100 photoelectrons of S1 signal size, including

even high mass WIMP expected signals. The energy spectrum of this background in the XENON1T experiment for 1 tonne FV is shown in Figure 2.5; from this plot is clear that the highest contribution is due to the SS shells and flanges of the cryostat, mostly due to ^{60}Co contamination, and from the PMTs.

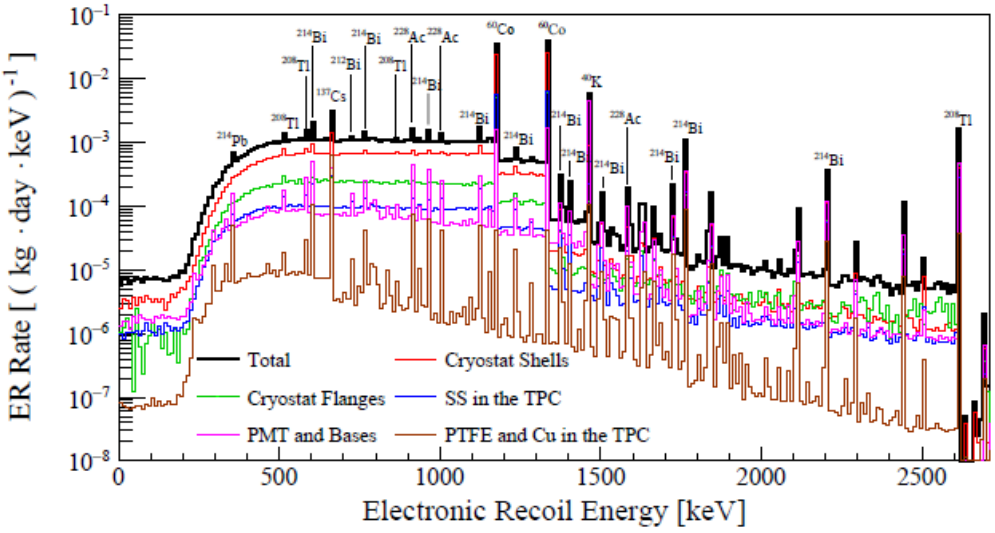

Figure 2.5: Energy spectrum of γ background. It is continuous and at low energy is almost flat while at higher energy the photo-absorption peak are visible. Plot from [103].

Regarding the NR background, the major contribution is represented by the *radiogenic neutrons* generated in the MeV energy range through spontaneous fission of ^{238}U,^{235}U and ^{232}Th and through (α, n)-reactions started by α-decaying daughter nuclei. Radiogenic neutrons can lead to multiple interactions. Their discrimination is linked to the detector efficiency in separating two close scatters.
From the start, the internal background can be avoided by a detector component selection in terms of high radio-purity following an extensive screening campaign [104]. In XENON1T this was possible thanks to one of the most sensitive facility based on Germanium detectors and mass spectrometry techniques available at Laboratori Nazionali del Gran Sasso. Secondly, the self-shielding property of LXe, and a correct selection of the Fiducial Volume can be exploited.

Intrinsic background Inside the LXe, radioactive noble gases, namely ^{85}Kr as well as the Radon isotopes ^{220}Rn and ^{222}Rn, contribute to the intrinsic ER background, for which the reduction through volume fiducialization is not effective. In order to handle this situation, one can use a proper purification system and minimize the emanation of contaminants into the xenon reservoirs. Xenon is obtained from air separation with the Linde cycle; thus a small portion of natural krypton is contained within the xenon with a typical concentration of $\mathcal{O}(ppm)$. The krypton isotope ^{85}Kr has a natural abundance of $^{85}\mathrm{K/K_{nat}} \sim 10^{-11}$ and is anthropologically released in the atmosphere after its production in nuclear reprocessing plants. It is a β-emitter with an half-life of 10.76 y; thus it has to be removed before starting the experiment and the reduction of its concentration in

LXe is usually achieved with a dedicated *cryogenic distillation column*.
Regarding radon isotopes, they are continuously emanated from detector materials. While ^{220}Rn has a half-life of 56 s and thus is not able to deeply penetrate the TPC, the ^{222}Rn diffuses homogeneously with a half-life of 3.8 d. Its decay chain consists of α-emitters, whose released energy is easily identifiable, and β-emitters; among these, ^{214}Pb decays in the ground state ^{214}Bi without the emission of further radiation, thus it contributes to the low energy ERs background. Even in this case, the approach for radon mitigation is based on the selection of materials with low emanation as well as a continuous radon removal system with cryogenic distillation. Finally, we have also the already mentioned isotope ^{136}Xe, which is a double-beta emitter with a half-life of $2.17 \times 10^{21}y$; with its low decay rate, its contribution to the final background is negligible.
Although electronegative impurities such as H_2, O_2, N_2, CO/CO_2 or H_2O cannot be considered background sources for the dark matter search, they are intrinsic contaminant since they capture free electrons and absorb scintillation light reducing both the ionization and the light yield. Their mitigation is achieved by continuously circulating LXe through a purification system.

External Background The external background accounts for several contributions:

- radioactivity of the materials contained in the surrounding rock as well as in the concrete of the experimental hall;
- neutrons inducted by cosmic muons;
- coherent scattering of astrophysical neutrinos.

Some of the isotopes already mentioned, like ^{238}U and ^{232}Th are present in the detector materials as well as in the environmental materials. Thus, low energy γ and neutrons contribute also to the external background component. Their reduction is easier to achieve, since it is based on the employment of a shield: in XENON1T, for example, the water layer inside the *water tank* shields the detector, with the result of lowering the γ flux of a factor 10^5 and the neutron flux of a factor 10^6 (in the MeV energy scale).
The strategy adopted to mitigate the contribution of neutrons induced by cosmic muons is instead different. These neutrons can have energy up to tens of GeV and they might cross the water tank, penetrate inside the TPC and mimic a WIMP-like interaction, contributing to the NR background. In this case, the *Muon Veto* (Section 2.3.1) exploits the Cherenkov light emitted along the muon path and detected by the PMTs; at this point, one has tagged a muon event, and this is used as veto during the data acquisition.
Apart from neutrons, astrophysical *neutrinos* can cause NRs as the result of the *Coherent Elastic ν-Nucleus scattering* (CEνNS). The CEνNS is a Standard Model process difficult to detect and it constitutes an irreducible background for noble liquid TPC-based experiments; as shown in Figure 1.17 it is the ultimate limitation to the WIMP sensitivity regarding the direct detection experiments. Figure 2.6 shows the most relevant contributions considering solar neutrinos, diffuse

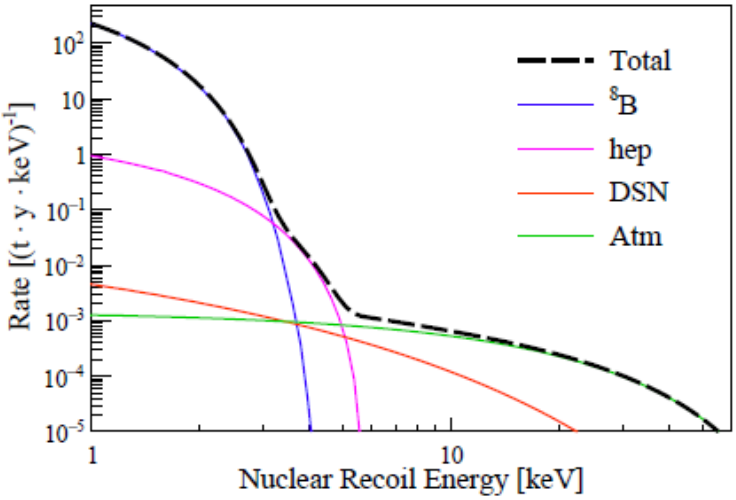

Figure 2.6: Various neutrino contributions to the NR background induced by via coherent neutrino-nucleus elastic scattering. Solar neutrinos (^{8}B, hep), as well as diffuse supernovae (DSN) and atmospheric (Atm) neutrinos, are considered (colored lines). The ROI is defined as the range [4,50] keV which includes the whole neutrino spectrum [69].

supernovae and atmospheric neutrinos. Solar neutrinos, even if with a subdominant contribution, are considered also as an ER background source as they can scatter off electrons of xenon atoms, causing a single low energy recoil.
The recoil energy spectrum of the NR background obtained for XENON1T in 1 tonne FV is shown in Figure 2.7. From the plot is clear that the dominant contribution to the NR background comes from radiogenic neutrons (internal background); thus emerges very naturally the need for a Neutron Veto.

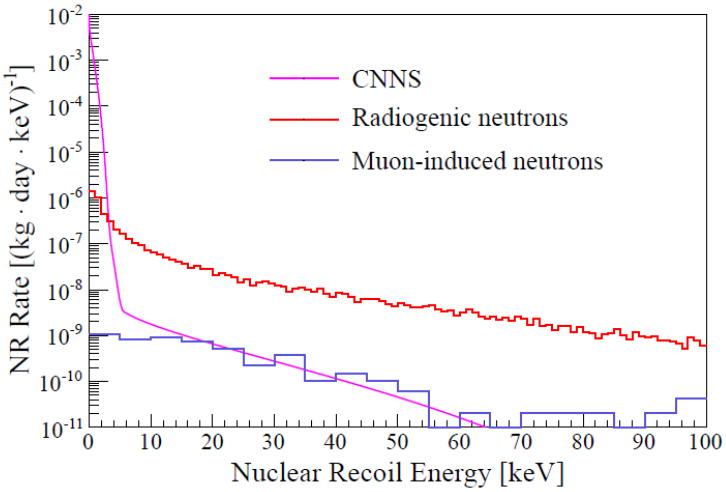

Figure 2.7: NR energy spectrum for backgrounds in 1 tonne fiducial volume. Considering that the ROI is defined in the [4, 50] keV range the dominant background contribution comes from radiogenic neutrons (red). Approaching the XENON1T lower energy threshold the contribution from the CNNS is higher. The one induced from muons is lower thanks to the Muon Veto [69].

2.3 The XENON1T experiment

The XENON1T experiment [105] (Figure 2.8), operational from 2016 until 2019, was the third phase of the XENON project, as well as the first liquid xenon detector with a target mass above the ton-scale. With 1 t·y of exposure, XENON1T reached a sensitivity of 4.1×10^{-47}cm^2 for WIMP with mass 30 GeV/c^2 [1]. The dual-phase xenon TPC (Figure 2.9) was enclosed within a double-walled vacuum cryostat and located in the center of a large cylindrical water tank. The suit of the experiment (Figure 2.8), entirely located in the Hall B of the LNGS underground laboratory, includes also a three-floor building which hosts the system to cool, purify and store the xenon gas, the cryogenic distillation column for the Kr removal, the data acquisition, and the slow control systems to monitor the entire experiment. Starting from the core of the experiment we have the cylindrical TPC of 97 cm height and 96 cm diameter, as shown in Figure 2.9. The TPC enclosed 2 t of LXe active mass, while an additional 1.2 t were used as a passive shield. Inside the TPC, an electric field of about 117 V/cm was applied between the cathode and the gate meshes while, inside the GXe region, an extraction field > 10 V/cm allowed the S2 signal production. To have an electric field as uniform as possible, 74 field-shaping electrodes with high thermal conductivity connected by resistor chains have been installed.
The detection of the signals is achieved with two arrays of photomultipliers (PMTs) positioned in the upper and lower sides of the TPC. In total there were 248 PMTs: 127 in the top array and 121 in the bottom one (further information on the PMTs used can be found in Section 4.3.1).
Moving out from the TPC, we find the double-walled, cylindrical stainless steel

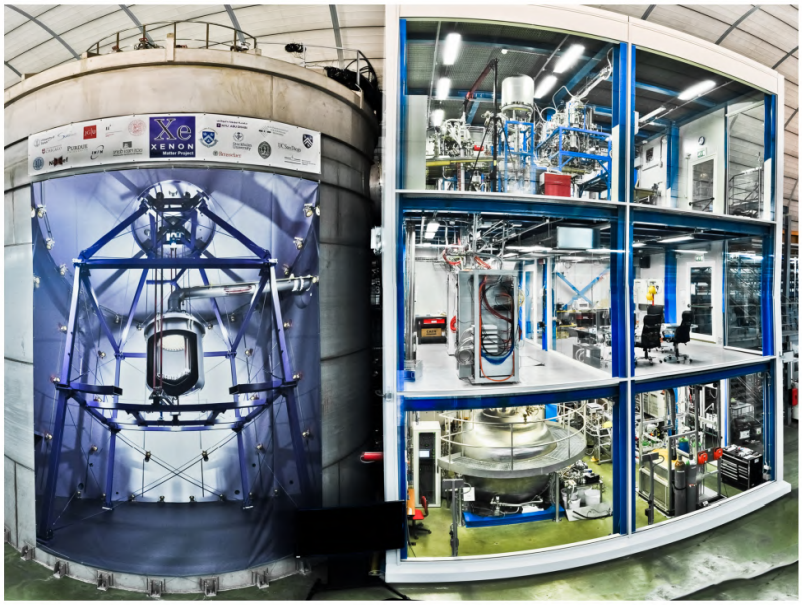

Figure 2.8: Picture of the XENON1T building, placed at LNGS. On the left, the Muon Veto (MV) water tank containing the TPC; on the right the Service Building which hosts the cryogenic and purification systems (top floor), the DAQ and slow control equipment (middle floor), the cryogenic distillation column and the ReStoX system.

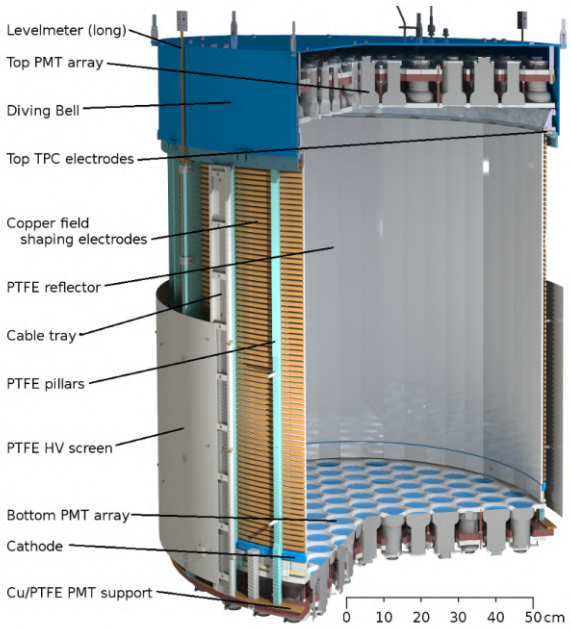

Figure 2.9: Illustration of the XENON1T TPC. The top and bottom PMT arrays are instrumented with 127 and 121 Hamamatsu R11410-21 PMTs, respectively [105]

cryostat made of low radioactivity material. To reduce the radon emanation the inner wall in contact with the LXe was electro-polished. The cryostat was designed to be already large enough to accommodate the detector of the upgrade stage XENONnT. Furthermore, the tilt of the cryostat and thus the orientation of the electrode planes with respect to the LXe surface can be adjusted from outside the suite by changing the length of three tie bars.
The outer shell of the experiment consists of the walls of the 10.2 m in height and 9.6 m in diameter water tank. Being the latter instrumented with 84 PMTs, it not only acts as a passive water shield for γ-radiation and neutrons from natural radioactivity, but also as an active water Cherenkov detector for cosmic muons.
Concerning the complex xenon handling system, this can be summarily divided into a cryogenic system, a purification system and a storage system called ReStoX (REcovery and STOrage Xenon). All these components are shown in Figure 2.10. The cryogenic system interfaces with the cryostat through a vacuum-insulated cryogenic pipe and deals with the extraction as well as the injection of the xenon, contributing to the purification loop. The purification system handles the task just mentioned, making use of getters to get rid of electronegative impurities. The xenon storage and recovery are finally addressed to the ReStoX system, which consists of a vacuum-insulated stainless steel sphere with 2.1 diameter, with a total capacity of 7.6 t xenon.
The calibration and the characterization of the detector response are essential for any experiment. Of course, this procedure was also present in XENON1T, where, the main calibration systems, were developed to study and monitor the PMTs functioning with LED sources, as well as to calibrate and to model the spatial response to physical interaction both for NR (with neutron sources) and ER (with ^{222}Rn) types.

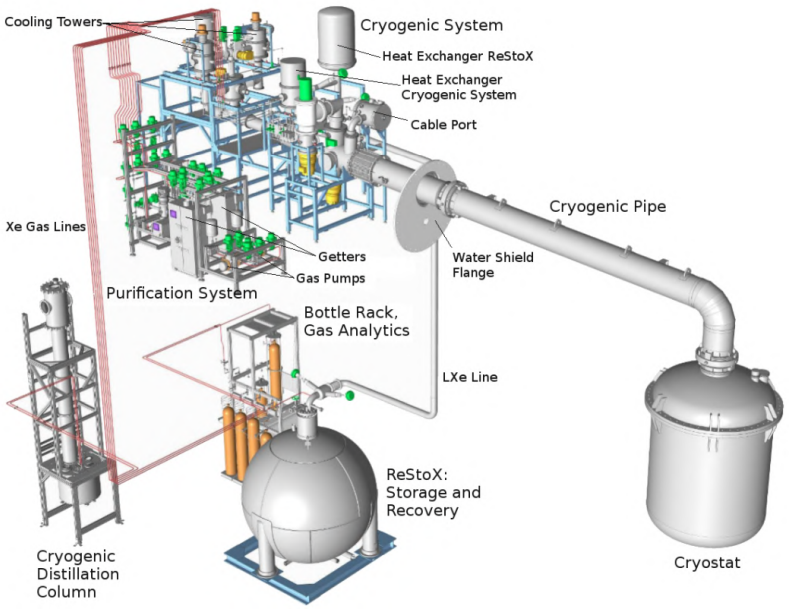

Figure 2.10: The xenon handling system of XENON1T consisted of the cryogenic system (cooling), the purification system (online removal of electronegative impurities), the cryogenic distillation column (^{nat}Kr removal), ReStoX (LXe storage, filling and recovery) and the gas bottle rack (injection of gas into the system) [105].

In Section 2.2 there was a detailed description of all the dangerous background sources. The only point left open concerns the mitigation strategy of the krypton isotope ^{83}Kr, which can not be simply reduced by purchasing high purity xenon (which has a ^{nat}Kr/Xe < 0.02 ppm). To reach a reduction of a factor 10^5 compared to the starting concentration, a 2.8 m tall distillation column was employed in XENON1T. This system allowed us to reach a concentration < 0.02 ppt demonstrating that it also met the requirements of the future XENONnT.

2.3.1 The Muon Veto system

Although mentioned several times throughout this chapter, the Muon Veto system deserves a more detailed description for several reasons. First of all, it is instrumented with photomultipliers (PMT) that are very similar to those that will be mounted in the Neutron Veto of XENONnT (Section 2.4) and they have undergone similar tests to those of which this thesis work deals. Furthermore, its design, construction, and calibration was under the direct responsibility of the Bologna research group. Building on the experience gained from that work, the group is also developing entirely the mechanics of the XENONnT Neutron Veto which is also part of the subjects of this thesis work.
Looking over the information of the PMTs installed in the Muon Veto (that will be presented in Section 4.3.2), it is interesting to dwell on the functioning of the detector itself. As already mentioned the Muon Veto operated (and will operate in XENONnT) as a Cherenkov detector with 700 t of de-mineralized water as medium. The detected particles are cosmic muons which have a flux of $(3.32 \pm 0.03) \times 10^{-8}\text{cm}^{-2}\text{s}^{-1}$ with an average energy of ~ 270 GeV in Hall B of the LNGS [105]. Muons are expected to emit Cherenkov light along their path inside the water tank. To improve the photon detection efficiency the inner surface of the water tank was cladded with reflective foil featuring a reflectivity $> 99\%$ at a wavelength between 400 nm and 1000 nm [106]. In addition, the foil acts also as wavelength shifter for a small fraction of the UV photons produced, which are shifted towards higher wavelengths to match the PMT quantum efficiency peak.
Following the Monte Carlo study indications, the 84 PMTs were deployed in five rings along the circumference of the water shield at different heights. The bottom and the top surfaces host 24 PMTs each, evenly spaced, while 12 PMTs were installed in the three intermediate rings. In Section 2.2 was mentioned the possibility of muons passing inside the water tank and leaving the standard Cherenkov signal (*muon event*), but they can also pass outside the water tank and in that case the detected Cherenkov radiation is produced by the charged particles of the shower generated (*shower event*). The latter case is, of course, harder to detect and can occur $\sim 2/3$ of the times [107]. Considering these two different occurrences, and the fact that the distribution of the γ arrival times to the PMTs is wider for shower-events (Figure 2.11), the resulting optimal trigger was to request the coincidence of 8 PMTs above the threshold of 1 photoelectron within 300 ns. All these details can be useful for understanding the detection strategy that will be adopted in the Neutron Veto system of XENONnT.

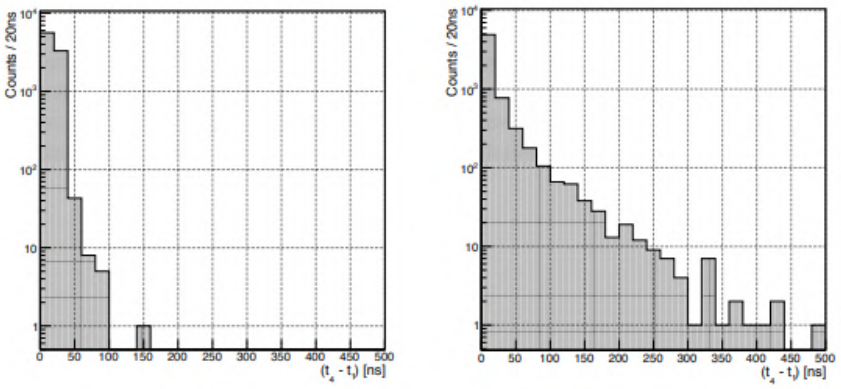

Figure 2.11: Distribution of the maximum time difference of photons arriving on the PMT photocathodes in a 4-fold coincidence [108].

2.4 The XENONnT upgrade

Ever since XENON1T planning, the concept was of a detector whose subsystems could accommodate the next phase. The cryostat outer vessel, as well as its support structure, were conceived so that a quick upgrade can be achieved, thus contributing to the detector scalability. The collaboration is now finalizing the XENONnT upgrade (Figure 2.12), whose new TPC will be placed in the same water shield and will be serviced with more or less the same infrastructures. However, the aim of improving the sensitivity of one order of magnitude, expanding the physics reach and the WIMP discovery potential, requires more than a larger target. Thus, in addition of LXe mass increase to 8 t, 6 t of which will be used as active target, it is foreseen a bigger TPC instrumented with more PMTs (494 instead of 248) as well as a further reduction of the internal background (achieved by a careful material selection). The background mitigation involves also the intrinsic component with a new online Rn-removal system; its functionality is based on the fact that, at this point, results essential to remove the Rn before it decays. Additionally, the ReStoX system inherited from XENON1T does not have the capability to accommodate the amount of xenon needed for the upgrade. Therefore an additional system ReStoX-II is required.
The real novelty of the project is the **Neutron Veto**, a veto detector to tag the radiogenic neutrons from detector materials, which come out from the TPC after leaving a single scatter nuclear recoil signal. The detection strategy, as well as the detector configuration, are described in the next chapter.
The upgrade currently under construction will enable us to achieve a sensitivity to the dark matter cross-section of $\sim 10^{-48}\text{cm}^2$, lowering of one order magnitude the XENON1T results (Figure 2.13) [103]. This result can be achieved also thanks to the Neutron Veto which will lead to the reduction of the number of background events from neutrons to about 1 event in the whole 20 t·y exposure (which means a reduction of the total NR background by a factor 6) [69].

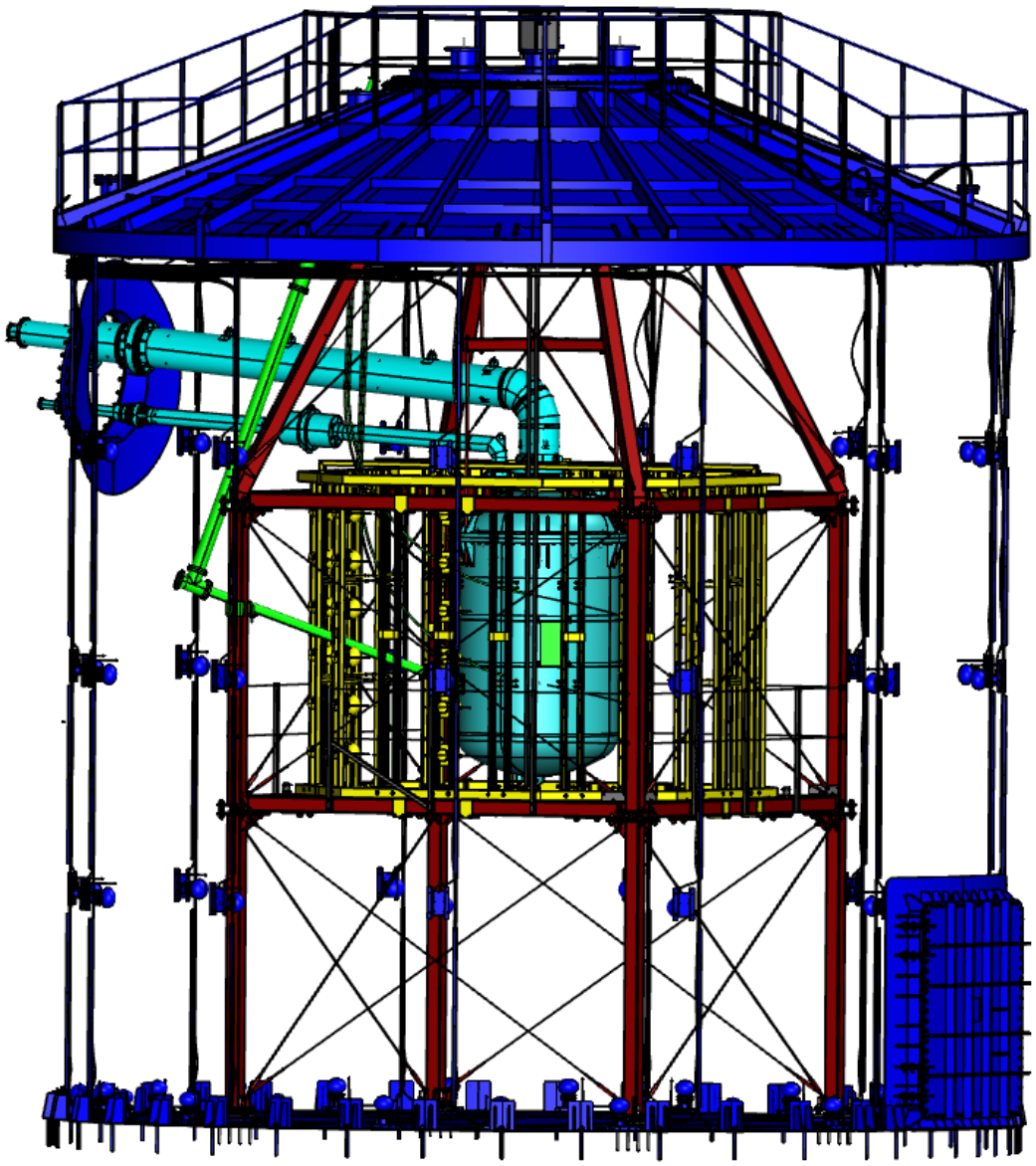

Figure 2.12: Drawing of the XENONnT detector. The various subsystems are highlighted with different colors. Starting from the outside we find the Muon Veto water tank (dark blue) with the 84 PMT installed. Then there is the support structure (red) of the cryostat (light blue). The Neutron Veto system is the real novelty of the experiment. Here in yellow is drawn only the nVeto support structure. A detailed discussion of the latter as well as of the other components not shown is the topic of section 3.3. Finally in green are highlighted some components of the calibration system.

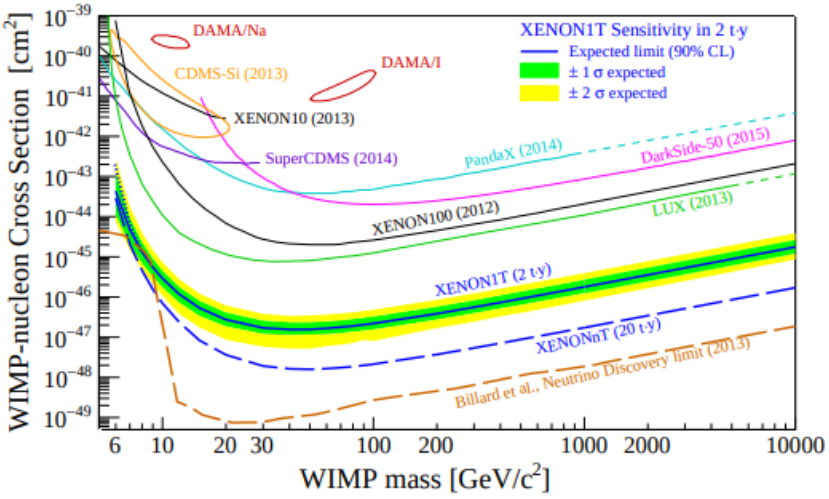

Figure 2.13: Plot of the spin-independent WIMP-nucleon interaction cross-section limits: the XENON1T sensitivity (90% C.L.) is highlighted with the solid blue line that represents the median value, while the 1σ and 2σ sensitivity bands are indicated in green and yellow respectively. The XENONnT predicted sensitivity is shown with the dashed blue line [103].

Chapter 3

The Neutron Veto system

In XENONnT the NRs background induced by radiogenic neutrons is not negligible, with an expected rate of about 1 event/yr in 4 t of fiducial volume. Thus arises the need of a neutron detector surrounding the TPC outer cryostat to tag neutrons from the detector materials, scattering inside the fiducial volume and leaving a WIMP-like signal. Furthermore, in order to increase significantly the DM discovery potential, the neutron tagging system should have an efficiency $> 85\%$.

The neutron detection is based on the following processes:

- thermalization of the neutrons in water;
- emission of the gamma-rays due to the neutron capture;
- Compton scattering of γ on the electrons;
- detection of the Cherenkov photons emitted in water from the electrons with $E_e \gtrsim 0.8$ MeV.

The neutron capture process has already a given probability to occur in water. However, in order to enhance the cross-section, it is foreseen the employment of the gadolinium loading technology. The Gd features the highest cross-section for thermal neutron capture among all elements as shown in Table 3.1. The Cherenkov photons emitted are then detected by an optimized number of photomultipliers which constitute the detector itself. A detailed description of the Gd technology

Isotope	σ [mb]	Q-value [MeV]
^{1}H	332.6	2.2
^{12}C	3.53	4.9
^{16}O	0.19	4.1
^{157}Gd	2.45×10^{8}	7.9

Table 3.1: Cross sections and Q-values (*i.e.* total energy of the emitted photons) for radioative thermal neutron capture (n, γ) reaction on nuclei that can be usually found in liquid organic scintillators and water Cherenkov detectors. The Gd isotope has the highest cross section and can be added both in liquid scintillator and water, in the form of Gd-salt. Table from [109].

can be found in Section 3.1 while the discussion on the Neutron Veto design and the description of the various challenges faced in its finalization are the topics of Section 3.2 and 3.3.

3.1 Neutron detection with Gd

Gadolinium ($^{A}_{64}$Gd) is a rare element on Earth. Its natural composition ^{nat}Gd consists of 7 isotopes. Their abundance ratio and the corresponding neutron capture cross sections are shown in Table 3.2. The Gd, in particular the ^{155}Gd and the

Isotope	Abundance (%)	σ [b]
^{152}Gd	0.2	735
^{154}Gd	2.18	85
^{155}Gd	14.8	60.9×10^3
^{156}Gd	20.47	1.8
^{157}Gd	15.65	25.4×10^4
^{158}Gd	24.84	2.2
^{160}Gd	21.86	1.4

Table 3.2: Thermal neutron capture cross sections of the various Gd isotopes that can be found in nature. Their abundance in ^{nat}Gd is also reported. The two isotopes which are exploited for their high (n, γ) cross section are the ^{155}Gd and ^{157}Gd.

^{157}Gd isotopes, has a resonance state in the thermal energy region in the neutron capture reaction (Figure 3.1). The capture process is resolved in the excitation of the Gd, which returns to the ground state emitting approximately 3-4 γ [109]. The process for the ^{155}Gd reads:

$$n + {}^{155}\text{Gd} \rightarrow {}^{156}\text{Gd}^* \rightarrow {}^{156}\text{Gd} + \gamma' s \tag{3.1}$$

Thus the γ-ray energy can be calculated via mass difference:

$$E_\gamma = M(^{155}\text{Gd}) + M_n - M(^{156}\text{Gd}) = 8.54 \text{ MeV} \tag{3.2}$$

where M_n is the neutron mass, while $M(^{155}\text{Gd})$ and $M(^{156}\text{Gd})$ are the mass of ^{155}Gd and ^{156}Gd respectively. Similarly, for the process involving the ^{157}Gd isotope, the γ energy is 7.94 MeV. Recently the natural gadolinium finds great application in the astroparticle physics experiment, particularly in the detection of the inverse beta decay process. Thus, it has become a common technique to dope liquid organic scintillator with a mass fraction of 0.1-0.2% of gadolinium (as already been done in the Double-Chooz experiment [110]). Another technique consists in adding Gd directly into water Cherenkov detectors. For instance, the Super-K experiment in its SK-IV [111] phase searches relic supernovae neutrinos exploiting the reaction:

$$\bar{\nu}_e + p \rightarrow n + e^+ \tag{3.3}$$

and the neutron capture on protons:

$$n + p \rightarrow d + \gamma \text{ (2.2 MeV)} \tag{3.4}$$

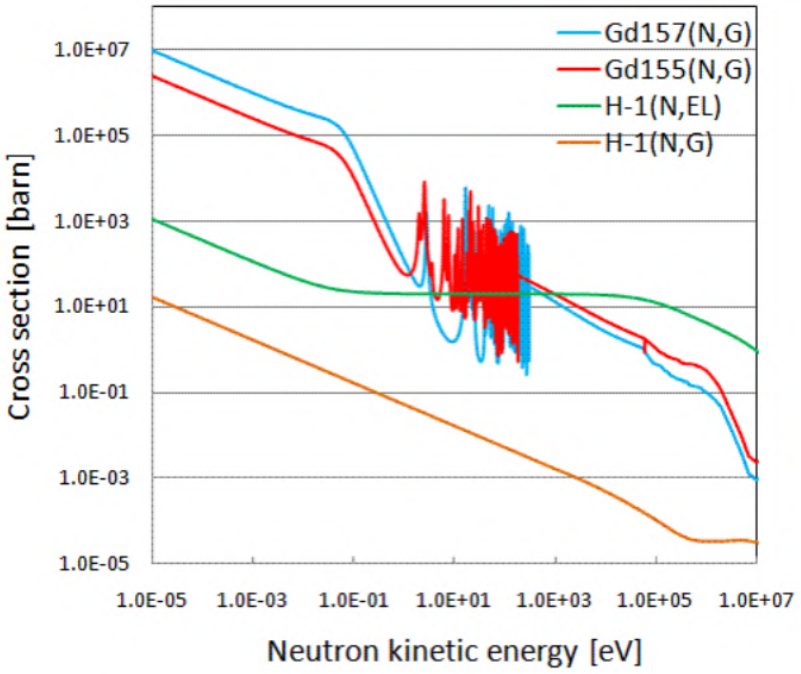

Figure 3.1: Trend of various cross section of the process involving neutrons and ^{1}H / ^{155}Gd / ^{157}Gd with respect to the neutron kinetic energy. The neutron-H interaction can occur as elastic scattering (green line) or as (n, γ) (yellow line). On the other hand the dominant process with the Gd isotopes is the (n, γ) (blue and red lines). The cross section for the Gd decreases with the energy but for values $\mathcal{O}$(eV) presents some resonant states.

which is characterized by a low detection efficiency. Thus it is planned Gd-doped SK in order to enhance the neutron detection efficiency. As an R&D project, the EGADS (*Evaluating Gadolinium's Action on Detector System*) prototype was built in 2009 with the aim to understand all the potential effects linked to the loading of gadolinium in water [91].

The XENONnT experiment, with the nVeto system, is the first DM experiment employing the Gd technology consisting in adding gadolinium in water. Thus, the attention is focused on the water Cherenkov detector flying over the scintillator case for now. Gadolinium is added in water by dissolving Gd ultrapure salts like $GdCl_3$, $Gd(NO_3)_3$ and $Gd_2(SO_4)_3$. Since the chlorine in $GdCl_3$ causes unwanted corrosion and the nitrate in the $Gd(NO_3)_3$ tends to absorb part of the Cherenkov light spectrum, the Gd-sulphate $Gd_2(SO_4)_3$ results to be the best candidate when it is octahydrate ($Gd_2(SO_4)_3 \cdot 8\,H_2O$), to enhance its solubility. It is used a concentration of $Gd_2(SO_4)_3$ of 0.48% which corresponds to about 0.2% concentration in mass of Gd. Figure 3.2 shows the fraction of neutron capture on Gd as a function of the concentration of gadolinium sulphate [112]. With a 0.2% concentration, the $\sim$ 90% of the neutrons are captured by the Gd, while the remaining part relies on the capture in water.
The nVeto of XENONnT will employ that concentration of Gd sulphate in order to reduce the NR background rate coming from the detector materials as shown in

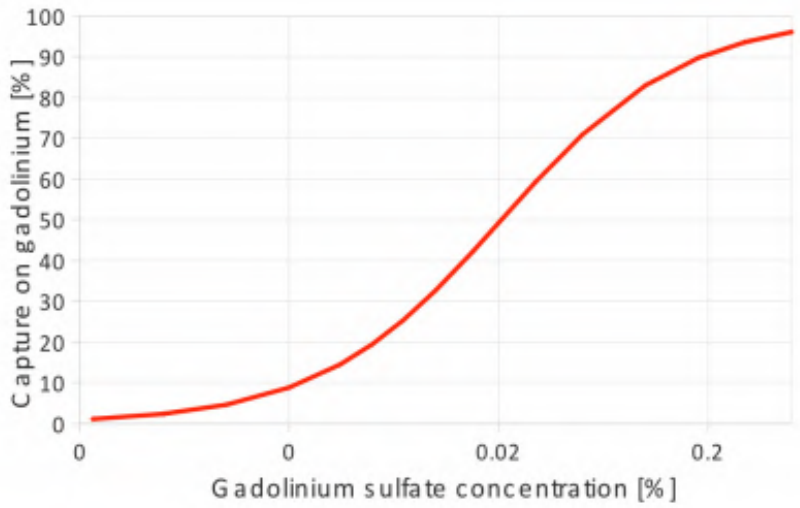

Figure 3.2: Fraction of neutron capture on Gd as a function of the $Gd_2(SO_4)_3$ concentration. With a 0.2% concentration, which correspond to a $\sim 0.1\%$ in mass of Gd, the $\sim 90\%$ of neutrons are captured by the Gd, while 10% are captured by protons as shown in Eq.(3.4). To reach the required neutron tagging efficiency in the nVeto, this concentration of Gd has to be loaded in water.

Figure 3.3. In addition that concentration is required to reach a neutron tagging efficiency $\geq 85\%$, which can be obtained by requiring a 10-fold PMT coincidence (Figure 3.4).

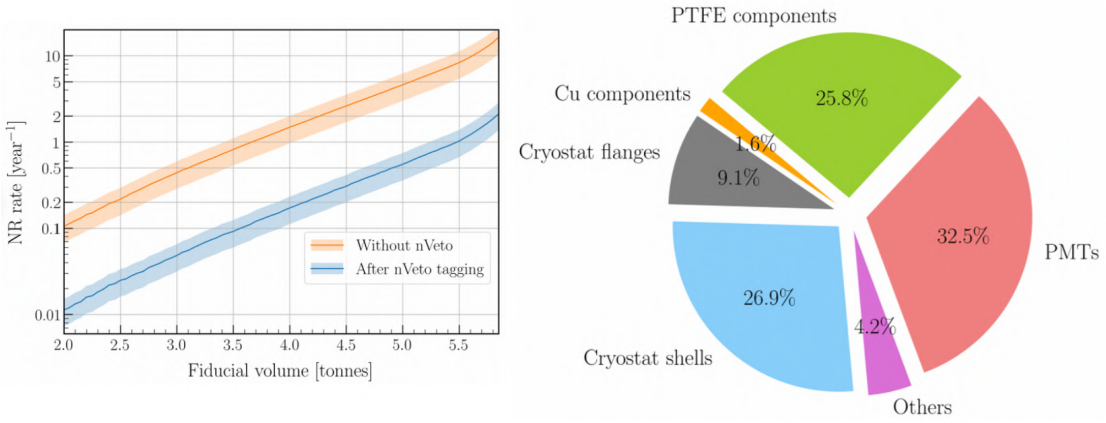

Figure 3.3: (Left) Nuclear recoil background reduction that will be achieved in XENONnT with the Neutron Veto operational (blue line). Considering a 4 t fiducial volume, the reduction factor is about 6. (Right) Diagram of the contributions to the NR background due to the detector materials. These are dangerous source since the emitted neutrons can give a WIMP-like signal inside the TPC [113].

As we will see in the next section the nVeto of the XENONnT experiment will consist of 120 PMTs oriented toward the cryostat to detect photons from neutron capture events.
The background induced by the materials that make up the nVeto (Section 3.3), is

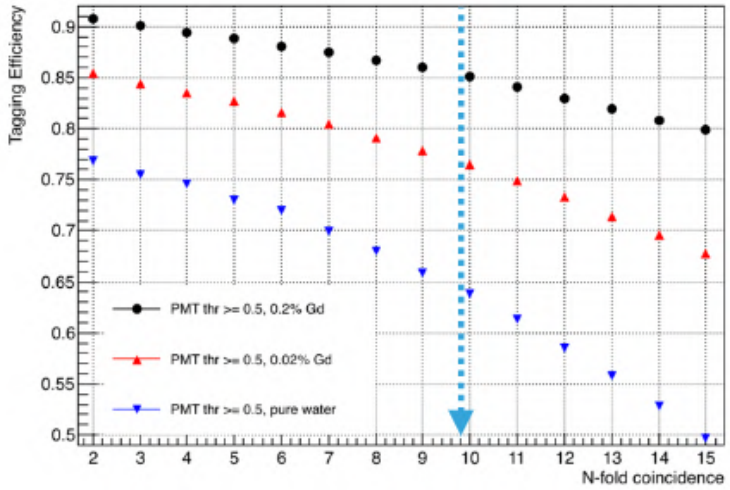

Figure 3.4: Neutron tagging efficiency as a function of the PMT coincidence for several nVeto configurations: (blue triangles) pure water nVeto, (red triangles) 0.02% Gd loaded nVeto and (black dots) 0.2% Gd loaded nVeto. With a 10-fold coincidence in the third configuration, the efficiency stands at $\sim$ 85% which is the requirement for the XENONnT purposes. In all the cases simulated the PMT threshold for the signal is at 0.5 photoelectrons. Thus it is important to study the characteristics of the PMTs such as the dark rate with this threshold.

summarized in Figure 3.5 (right).

that will not be dangerous for the TPC but for the nVeto itself is summarized in Figure 3.5. That background contributes to the fake event rate, that is about

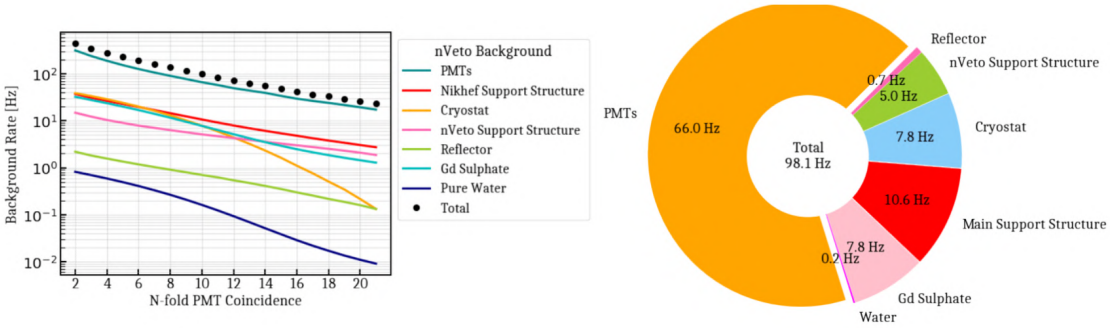

Figure 3.5: Background contribution to the fake neutron tagging. From simulations, the total fake rate stands $\sim$ 100 Hz.

$\sim$ 100 Hz for a 10-fold coincidence (Figure 3.5 (left)).

3.1.1 Gd-soak test

The general philosophy of the XENON experiments is that, in order to have an ultrapure detector, all the materials used in the various subsystems must pass the radioactivity screening test. This is also needed to have complete knowledge of all internal background sources. However, the addition of the gadolinium in the

XENONnT experiment requires more effort on the materials choice. As a matter of fact, the Gd added in water may corrode and quicken the material aging. Thus there is the need to perform also the so-called *Gd-soak test* on any detector material, to evaluate any potential deterioration and to choose more suited materials.
Such kind of tests, which consists of the immersion of the detector components in a Gd-water solution, were also carried out in view of SK-Gd (Section 1.3.2).
For XENONnT, we had to take into account those requirements, making the design and construction procedure harder to accomplish.
The Gd-soak test of each material provided also a transparency study of the corresponding water-Gd solution. Indeed, since the water in the nVeto acts as a Cherenkov medium, one has to avoid as much as possible the absorption of the photons emitted.
According to the SK experience materials like the stainless steel (AISI304), the PTFE, and the polyethylene are fine with the gadolinium solution. Those materials will be profusely used in the nVeto design. In addition, the XENONnT experiment will require more than a simple water purification system for the water tank; what is required is an external system that deals with both the purification of water+Gd and the gadolinium storage/recovery. The nVeto group is finalizing such a system thanks to the contribution of the Japanese groups, some of which are involved either in EGADS and SK (Section 1.3.2).

3.2 Story of the Neutron Veto design

The aim of the XENONnT experiment is to enhance the WIMP discovery potential by increasing the sensitivity obtained with the previous phase. Thus, the idea of a neutron tagging detector was born, aiming to mitigate the NR background due to radiogenic neutrons.
Since its initial proposal, several structural projects of the nVeto system were studied. A first idea was to use LAB liquid scintillator loaded with Gd as neutron radiative capture medium (Figure 3.6). The advantages of that solution were a great light yield and a relatively easy detector design. The reason why it was soon discarded in favor of the addition of Gd in water, is mainly related to laboratory safety aspects. The LZ experiment on the contrary adopted the idea of scintillator boxes for its neutron veto "outer detector" [68]. With the Gd-water proposal, adopted in XENONnT, one must live with the problem of the lower light yield due to the high Cherenkov threshold, about 0.8 MeV for electrons.
The general structural idea for the nVeto is that of an inner volume optically separated from the Muon Veto.
Several geometries for the PMT displacement were simulated:

- box shape;
- octagonal shape;
- cylindrical shape.

which are showed in Figure 3.7 (left); on the right is shown how the nVeto tagging efficiency varies with the required number of PMT coincidence signals, for the three

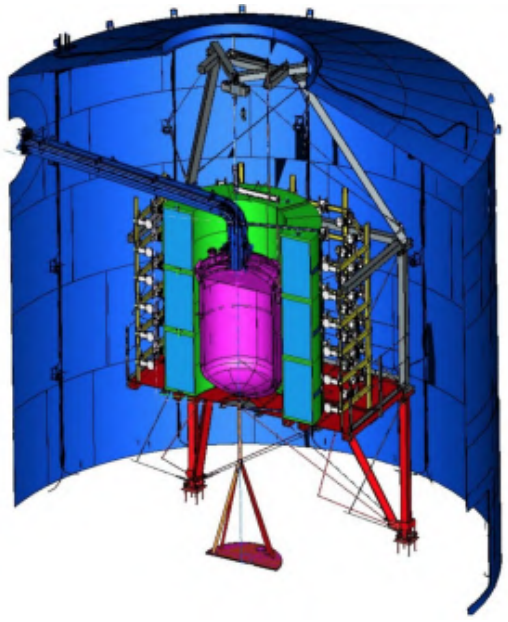

Figure 3.6: Image of the first design proposed for the nVeto system. It consisted of an external structure hosting the PMTs and liquid scintillator boxes (green/light blue) standing between it and the cryostat.

geometries. In each of the three cases, requiring a 10-fold coincidence, a tagging efficiency of $\sim 85\%$ was achieved. In the end, we opted for a non-regular octagonal structure for an overall design as shown in the top of Figure 3.8. The optical separation from the outside is achieved using ePTFE reflective sheet panels whose properties will be described later. The next section is dedicated to a more detailed look at the last nVeto structure design as well as to the preliminary work done in view of the future construction of the detector.

3.3 Final design and construction

The design of the nVeto detector is under the responsibility of the Bologna research group. We took care of the integration of the apparatus with the subsystems already present, up to the optimization of the initial design; a lot of efforts were made trying to solve all the interference mainly coming from the calibration system components and from the cryostat pipes. In the end we managed to get to a complete project, whose description is the topic of this section. The whole design can be split in two main components:

- **mechanical support structure** which represents the skeleton of the apparatus also including the holders of the PMTs instrumenting the nVeto system;

- **reflector panels** which define the nVeto volume around the cryostat. It contain, almost tightly, the light produced by the neutron capture events.

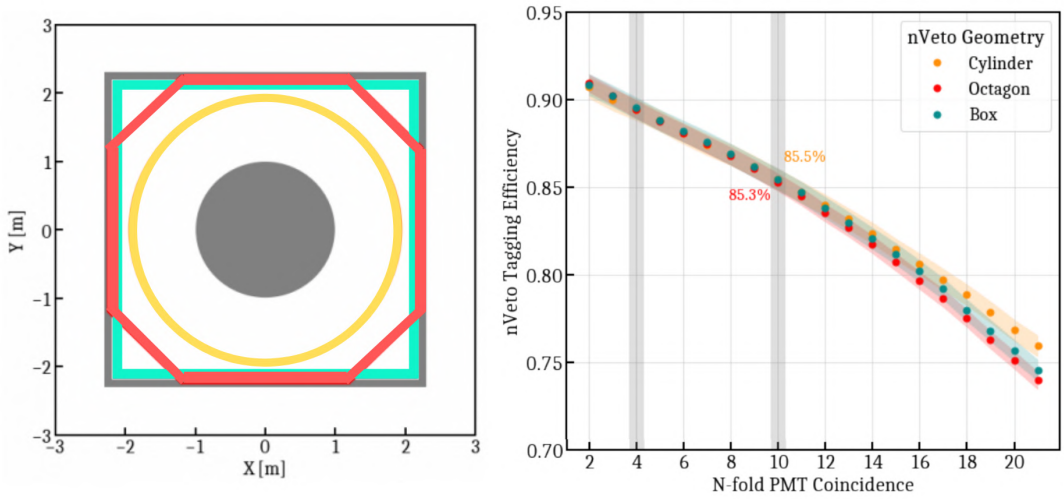

Figure 3.7: On the left, drawing of the solutions proposed for the nVeto geometry, *i.e.* the box, the octagonal and the cylindrical shape. On the right are reported the plots of the neutron tagging efficiencies for the various geometry as a function of the number of PMTs required in coincidence. The octagonal shape (red curve) has a good efficiency for low coincidences with respect to the cylinder (yellow curve). The box stands as a middle ground between the other two. However, for a 10-fold PMT coincidence, a neutron tagging efficiency of 85% is achieved with all the geometries.

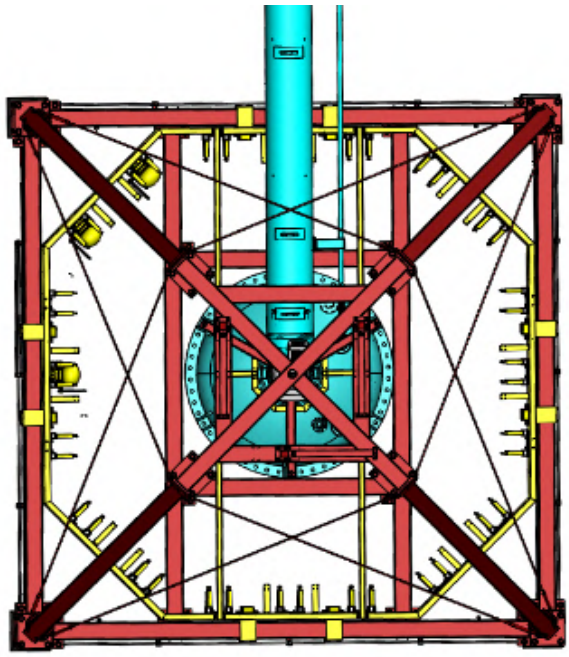

Figure 3.8: Image of a top view of the nVeto structure (yellow), the cryostat support structure (red), surrounding the cryostat (light blue). A view of the whole experiment, including the water tank, is shown in figure 2.12.

3.3.1 Mechanical support structure

Figure 3.9 summarizes the main design features of the nVeto stainless steel mechanical support structure. The structure, anchored to the pillars sustaining

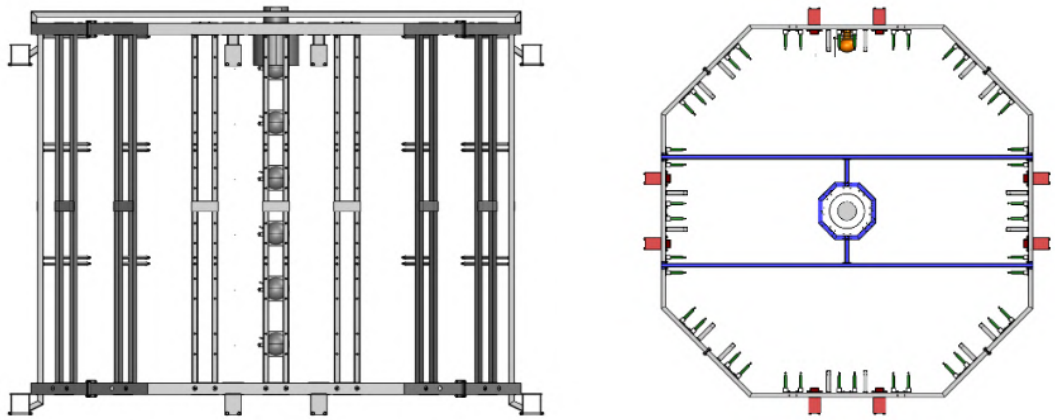

Figure 3.9: Drawings of the 3.3 m tall mechanical support structure. (a) Lateral view. The longer sides of the octagon are 2.2 m length while the shorter ones are 1.4 m lengths. (b) Top view where some elements are highlighted. The two horizontal bars serve to support the roof made by reflector panels. The red holders instead accomplish the anchoring to the cryostat support structure. The outgoing green spacers will support the side panels instead.

the cryostat, has to support the reflective panels as well as the PMTs. The nVeto structure has an irregular octagonal shape with four longer (2.2 m) and four shorter (1.4 m) sides. All around the structure, there are vertical pillars to hold both the PMTs (as shown in Figure 3.10) and the reflective panels. Six photomultipliers can be arranged on each pillar. In the end the structure can host 120 PMTs. On the top of the structure, there are two horizontal bars (Figure 3.9b) that support the reflective roof panels and provide a small inclination to drain the water (when emptying the water tank).

3.3.2 Reflector Panels

Reflectivity plays an important role in achieving a high tagging efficiency. In particular, the expanded-PTFE (ePTFE) results to be the best candidate to be employed in the nVeto, enhancing the light collection efficiency of the Cherenkov photons as well as their containment. The lateral walls of the nVeto will be realized by assembling several reflective panels. The latters are made of polyethylene frames on which reflective sheets of ePTFE are fixed, as shown in Figure 3.11. Due to the fact that the PMT themselves are a background source, we arranged the panels in such a way to have only the photocathode emerging from the holes (as shown in Figure 3.12) . Indeed, it has been seen from the simulations that, passing from the reflective sheet behind the PMT body to the PMT window equator, a

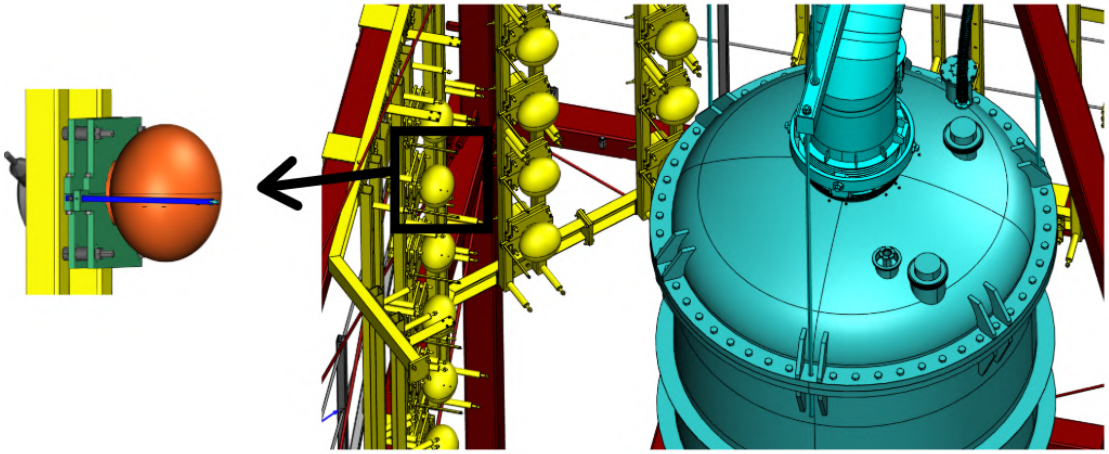

Figure 3.10: View of the nVeto from the top. The PMTs mounted on the structure (yellow) as shown in the left zoom, point in direction of the cryostat (light blue) which is sustained by the structure colored in red.

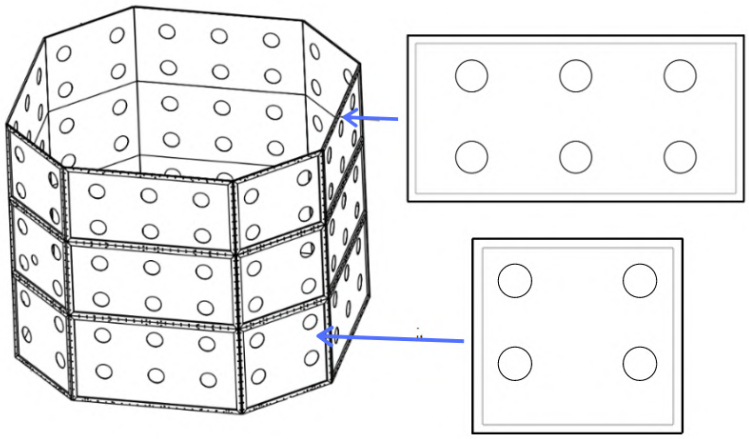

Figure 3.11: Drawing of the entire lateral surface of the nVeto as composed by several reflector panels. On the right the two main panel typologies are reported (long and short sides). Each panel is designed with holes in correspondence with the PMT positions.

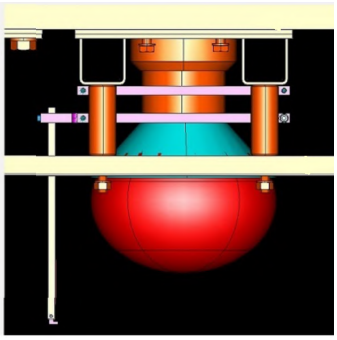

Figure 3.12: Drawing of one PMT mounted on the nVeto support structure shown as a reference. The PMTs will come out from the reflector panel up to its equator.

background reduction of $\sim 70\%$ was achieved. Thus, the final configuration is the one represented by Figure 3.12 and can be seen also in Figure 3.13, which is a picture from the prototype that we built in Bologna (discussed in detail afterward).

(a) (b)

Figure 3.13: Photos of the nVeto structure prototype with the five PMTs and the reflector panel mounted. (a) view from inside the structure. (b) view from behind.

The design of the panels that make up the side surface is different from those that constitute the roof and the floor of the nVeto reflecting panels. The shape of the latters are designed to take into account all the interferences (mainly on the roof), related to the calibration elements and the cryostat pipes; thus we came to the solutions shown in Figures 3.14 and 3.15.

Furthermore, the reflective foil has to be installed also on the cryostat surface. As shown in the plot of Figure 3.16, this is necessary in order to have the required neutron tagging efficiency. The cryostat wrapping will be achieved by shaping the reflective foil as the five sectors highlighted with different colors on Figure 3.16 (left).

Moreover, since the reflectivity of the ePTFE foil is fundamental for neutrons detection, it has to be monitored during the nVeto operation. Indeed, even if the reflectors have not shown any visible deterioration of the surface during the soak test, there might be longer-term effects of Gd-sulfate water on the reflectivity of the surface. For instance, the corrosion of some other materials in the water tank may produce particles that stick to the reflector surface or accumulate on the bottom reflector. Thus a reflectivity monitor system, based on the injection of LASER light, has been foreseen (Figure 3.17). The light is sent through quartz optical fibers towards both the top and the bottom nVeto reflectors in order to compare

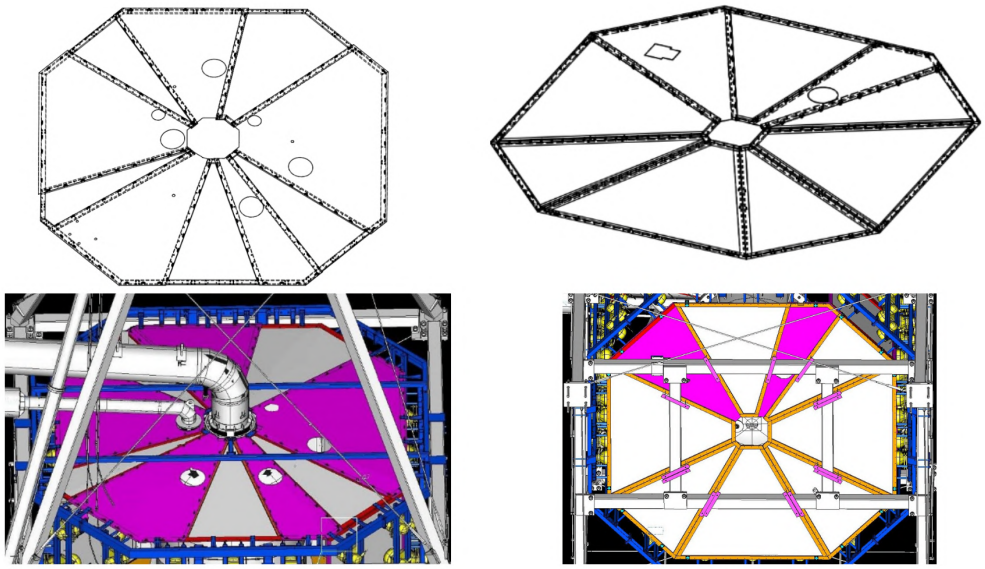

(a) **Roof** (b) **Floor**

Figure 3.14: Drawing of the nVeto roof (a) and floor (b) with both the 2D view (above) and 3D view (below). To solve the interferences, the top reflectors are designed with holes for the elements in correspondence of the calibration elements, as well as for the pipes of the cryostat. Some interferences from the calibration are always present on the floor panels. The pink reflective foils are the one designed with the holes.

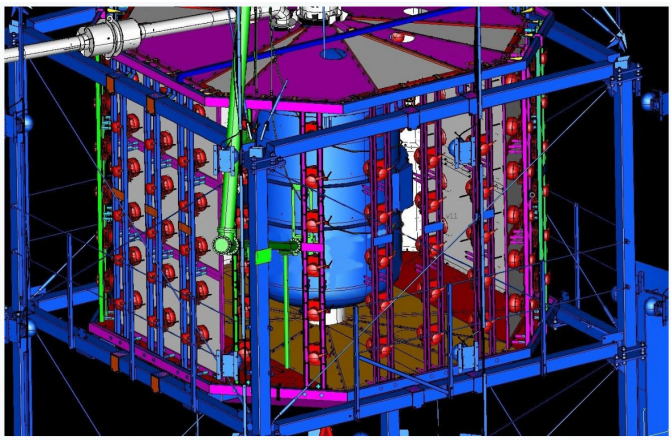

Figure 3.15: View of the Neutron Veto with most of the reflectors installed. The various incoming elements that create interference with the walls are also shown.

the two reflectivity measurements[1].

The main operations to be carried out in order to be ready for the construction of the nVeto were the design of the entire apparatus (described so far) and the test of the photomultipliers. To date, these tasks have been completed, and the discussion regarding photomultipliers is the subject of the second part of this thesis work.

[1]The expected deterioration would involve mainly the bottom reflectors.

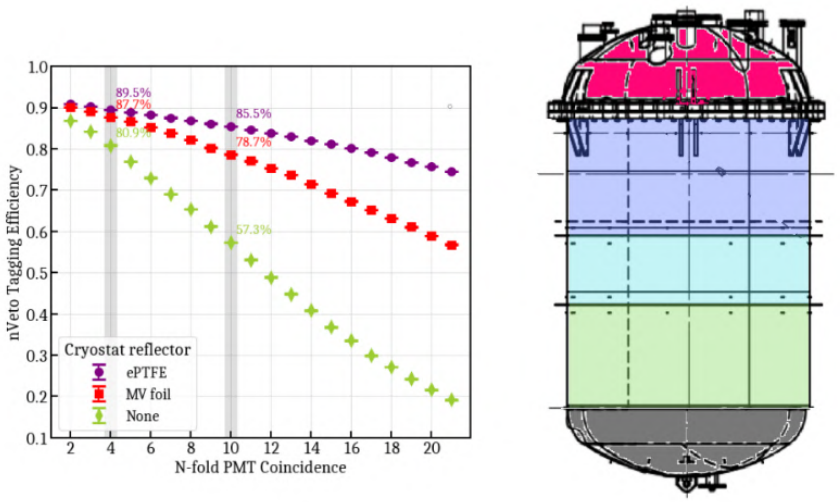

Figure 3.16: (Left) Plot of the neutron tagging efficiency as a function of the PMT in coincidence with various options for wrapping the cryostat; it is clear the need to cover it with a reflective layer. In addition, with 10-fold coincidence, an efficiency higher than 80% is achieved only employing the ePTFE as reflector, rather than the one covering the water tank walls. The coverage of the cryostat will be realized by shaping the reflective foil according to the five sectors individuated (right).

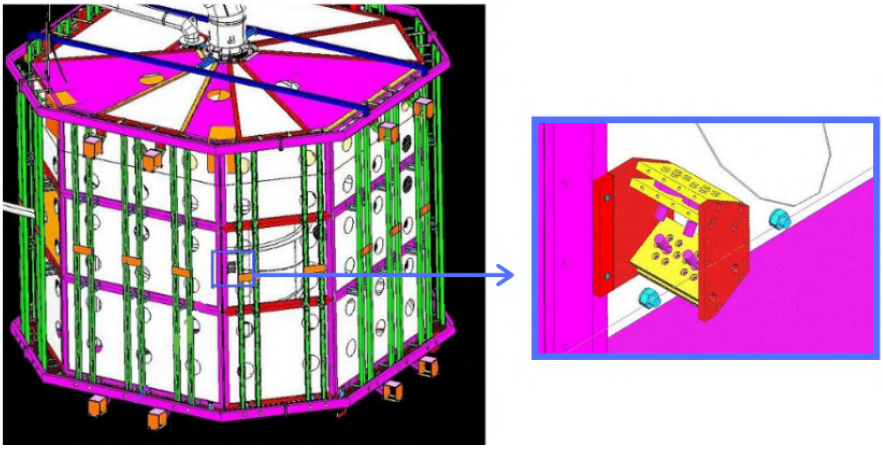

Figure 3.17: Drawing of the polyethylene support for the fiber of the reflectivity monitor system (right) and location inside the nVeto (left).

Prototype and mounting test As already mentioned, we built a quarter of the nVeto support structure, in a room of the Physics Department of Bologna University in September. This was done to test the mounting procedure as well as to optimize some details of the design. We installed some PMTs and with them the reflector panel (Figure 3.13). We had to take care also for the mounting of the panel, by fixing the ePTFE foil to the frame with plastic screws.

In the end, we managed to obtain the reflector panel shown in Figure 3.18 and starting from that we used a paper template to cut the sheet (Figure 3.19).

This exercise represented an attempt to establish an assembly procedure for the reflective sheets as well as for the structure. While the latter will then be installed directly in the detector at LNGS, the frames and the reflective sheets will

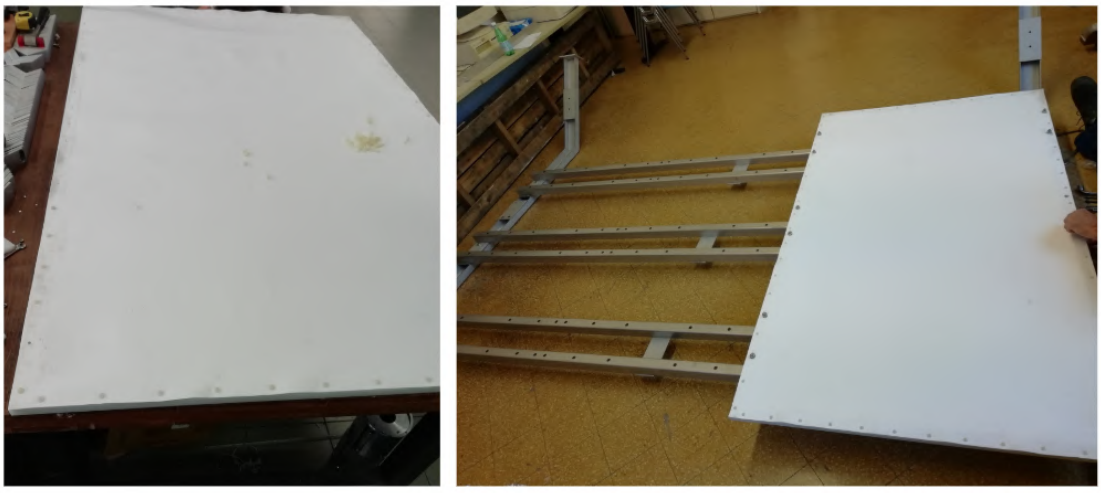

(a) (b)

Figure 3.18: Photos from the mounting phase of the reflector panel with the plastic screws (a) and of its fixing on the support structure (b).

be entirely produced and assembled in Bologna, respecting the cleaning conditions in view of a quick installation in the nVeto.

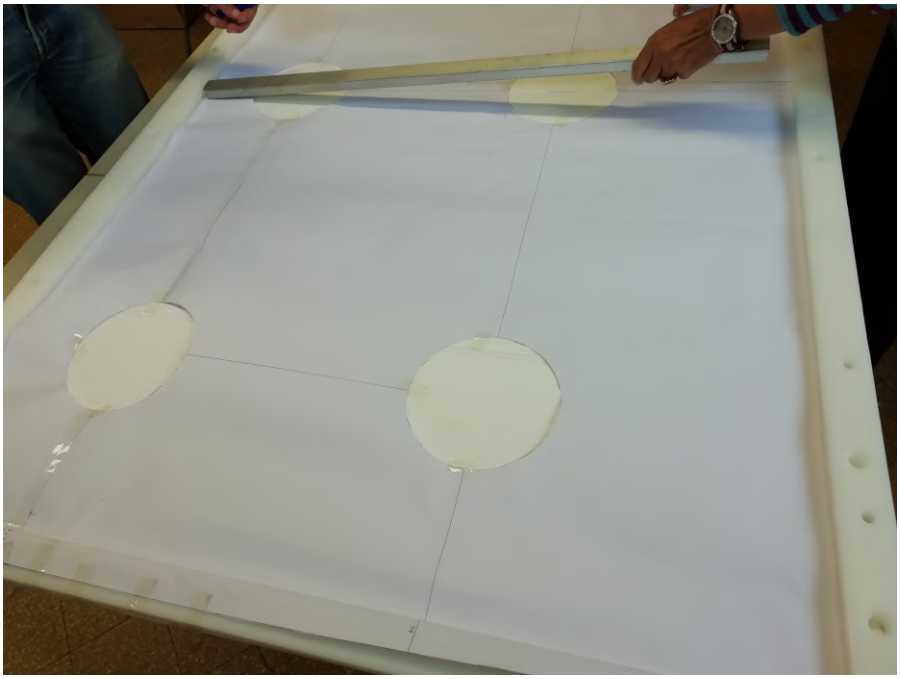

Figure 3.19: Photo of the preparation of the reflective foil to accommodate the PMTs mounted on the structure. By means of a paper template we made the circular cut on the reflective foil.

Chapter 4

Photomultiplier tubes

A Photomultiplier Tube is a vacuum tube that converts a light signal hitting an input window, called *photocathode*, into an amplified electrical current. These devices are extremely sensitive, fast and thus widely used in High Energy Physics. In this chapter the main characteristics of PMTs are discussed; furthermore it will be discussed their role in the whole XENON Project.

4.1 Structure and functioning

Figure 4.1 shows the essential elements of a typical photomultiplier:

- a *photocathode* made of photosensitive material which converts light flux into electron flux;
- an *electron-optical input system* which focuses and accelerates electrons flux;
- an *electron multiplier* subsection or dynode string, which consists of a series of secondary-emission electrodes called *dynodes*;
- an *anode* which collects the electron flux and supply an output signal.

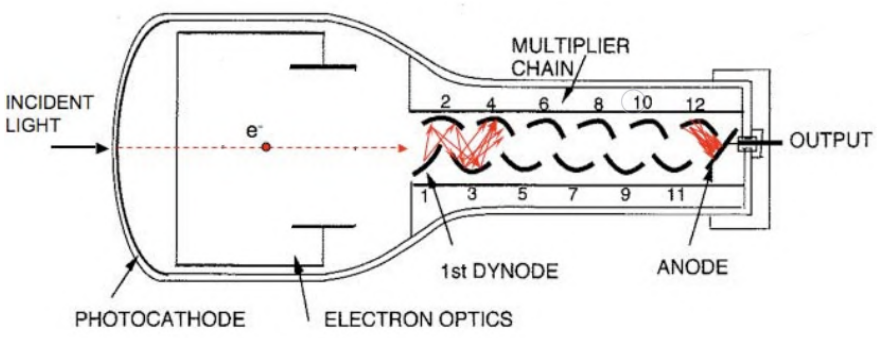

Figure 4.1: Schematic of a photomultiplier tube (PMT) with the main component highlighted.

During operation, a high voltage is applied to the elements such that a "potential ladder structure" is set up along the PMT. When an incident photon with frequency

ν and wavelength λ hits a material with extraction potential Φ, it emits an electron, via photoelectric effect, with energy :

$$E = h\nu - \Phi \tag{4.1}$$

Not all the incident photons lead to electron emission; the photoelectric conversion efficiency is a function of the wavelength as well as of the composition and thickness of the photoemissive material. The ratio

$$\eta(\lambda) = \frac{\text{number of released electrons}}{\text{number of incident photons}(\lambda)} \tag{4.2}$$

is called *Quantum Efficiency*.

Because of the applied voltage, the electron is focused by the electron optical input system and accelerated toward the first dynode where, upon striking, it can cause emission of secondary electrons via secondary emission process. The number of electrons emitted in this way is given by:

$$\delta = \frac{\text{number of secondary electrons emitted}}{\text{number of primary electrons}}, \tag{4.3}$$

which is called *secondary emission coefficient*. These electrons are accelerated towards the second dynode and so on; an electron cascade is thus created. The latter is collected by the anode to give a current which can be amplified and analyzed.

4.2 Fundamental characteristics of photomultipliers

In the usage of the photomultipliers one refers to certain parameters (whose values are usually reported in the data-sheets) that resume their efficiency and their functioning in various conditions. This section describes the fundamental characteristics of the PMTs operation.

Collection efficiency The collection efficiency is defined as the ratio between the number of photoelectrons reaching the first dynode and the number of electrons emitted from the photocathode. Since it is a function of the initial velocity of the electrons, it varies with wavelength. The collection efficiency depends also on the voltage applied between the cathode and the first dynode. Furthermore, this parameter affects the single photoelectron (pe) resolution and the *detection efficiency*. The latter is defined as the ratio of the detected signal to the input signal of a photomultiplier tube (Figure 4.2) and is given by the product of the quantum efficiency and the collection efficiency.

Gain The gain (G) is defined as the ratio between the anode current and the cathode current. For a phototube in an N-stage dynodes multiplier with g_i gain on

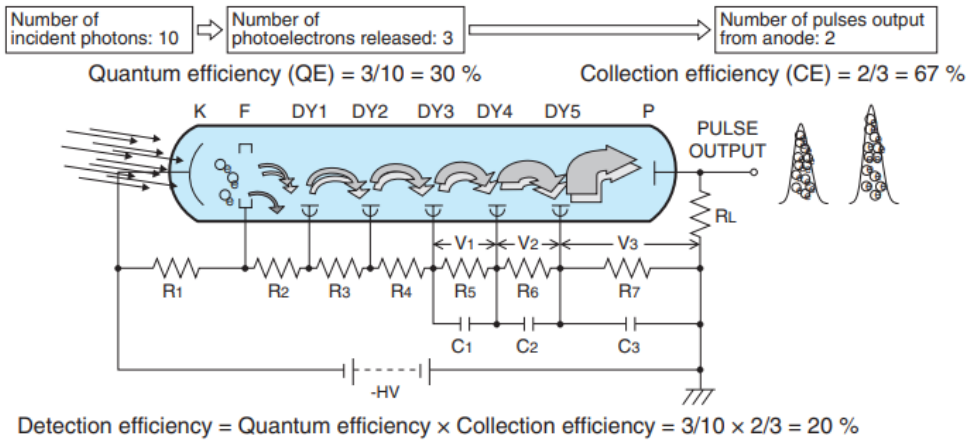

Figure 4.2: Explanation of the detection efficiency concept in a specific case where 10 photons hit the photocathode. Considering a realistic quantum efficiency of 30%, 3 photoelectrons are produced. Finally, the collection efficiency for the whole dynodes chain gives the number of electrons collected at the anode. Thus the detection efficiency is given by the product of the two efficiencies.

the i-th stage (given by the collection efficiency of the i-th dynode α multiplied for the secondary emission coefficient δ), one has that the anode current I_{anode} is:

$$I_{anode} = I_k \alpha \prod_{i=1}^{N} \delta = I_k \prod_{i=1}^{N} g_i. \tag{4.4}$$

Thus, the gain is given by

$$G = \frac{I_{anode}}{I_k} = \prod_{i=1}^{N} g_i. \tag{4.5}$$

Usually the multiplication region contains 10 to 14 stages with a total overall gain of $\sim 10^7$. If the collection efficiency α of all stages approaches to 100%, the gain becomes equal to the product of all the secondary emission coefficient. Therefore since one has:

$$\delta \propto (V^a_{dynode}) \tag{4.6}$$

with V_{dynode} equal to the intra-dynode voltage and $0.7 \leq a \leq 0.8$, the relation between the gain and the applied voltage is:

$$G = \prod_{i=1}^{N} k_i V^a_{i-dynode} = K V^{Na}_{hv} \tag{4.7}$$

For a ten stage PMT, for instance, the gain increases as the 7th power of the supply voltage V_{hv}.

Going back to the amplification process, the electrons are accelerated and focused by an intra-dynode electric field that is established with a voltage divider across the terminals of a high voltage supply 4.3. Since the most sensitive part of the chain is the coupling of the electron-focusing system and the first dynode, a higher voltage is often applied between the first two/three dynodes.

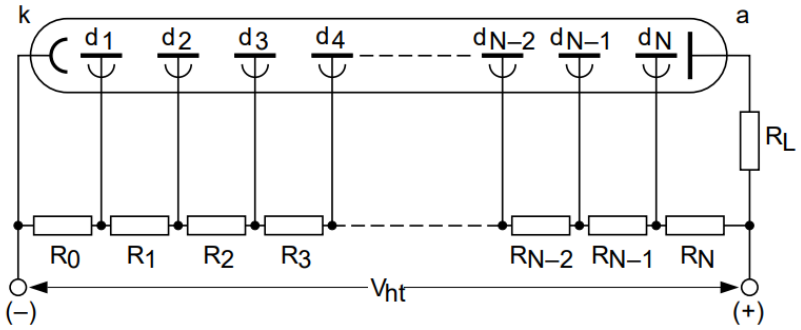

Figure 4.3: Typical scheme of the voltage divider for the high voltage supply. With k is indicated the cathode and with a the anode [114].

Single photo-electron spectrum When the usage of the PMT is oriented towards the detection of very weak signals, such that the pulses are generated by single photoelectrons (p.e.), the concept of single p.e. spectrum becomes important. It is described as the distribution of the amplitudes of the signals and can be described by several parameters:

- Peak-to-Valley Ratio (P/V)
- Single p.e. resolution: defined as the FWHM of the single p.e. peak divided by its mean value[1].
- Mean value of the peak: this is directly correlated to the gain of the Photomultiplier.

Because of the statistical nature of the secondary-emission process, the single p.e pulses show very large amplitude fluctuations. A contribution to the lower part of the single pe spectrum is given by sub-amplified photoelectrons, which are backscattered by the first dynode and therefore skip some steps of the amplification chain.

4.2.1 Time Characteristics

The photomultiplier tubes are photodetectors with a fast time response. The latter is determined mainly by the transit time required for the photoelectrons to reach the anode after the amplification; also the transit time spread between each photoelectron, under certain conditions can be significant. At the structural level, the dynode type determines mainly the time response, which depends also on the supply voltage.

In figure 4.4 is shown a typical setup for the measurement of the main time characteristics, i.e. *Transit Time* (TT) and the *Transit Time Spread* (TTS). These parameters are theoretically defined as the response to a delta-function light pulse; this means that the light pulse used for the calibration must have a FWHM much

[1]in case one approximates the statistical description of the PMT behavior with a Gaussian distribution.

lower than the time spread that has to be measured. Usually, these quantities are $O(1)$ ns, so they can be measured using light pulses of 0.1 ns width; thus the usage of a LASER is mandatory. Furthermore, the timing parameters depend on the illumination level, being minimum that is why they are usually single p.e. conditions.

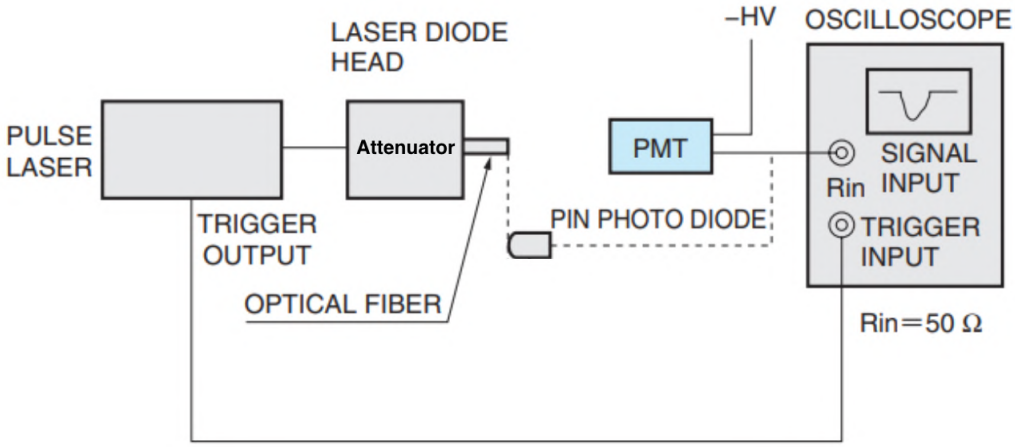

Figure 4.4: Schematic of a hypothetical setup for the PMT transit time measurement. Starting from left we have a LASER whose light is sent to a PMT via an optical fiber. Since the light coming out from the LASER is collimated, in order to avoid the damaging of the input window, the light is filtered by an attenuator; in this way, one can select the proper incoming amount of light (to have the single pe condition). The attenuator is also useful to spread the light so that can reach a photodiode used to measure the t_0 time (reference time). Knowing t_0, the transit time of the PMT is obtained as $t_f - t_0$ where t_f is the instant when the PMT signal is observed under the oscilloscope (which as to be fast)[115]. A similar setup was used also during the XENONnT PMT test.

Transit Time (TT) The Transit Time is the time interval between the arrival of a light pulse at the photocathode and the appearance of the output pulse. Its mean value t_{TT}, evaluated over a statistically large number of pulses, varies with the inverse square root of the high voltage [115]. From the definition, it is clear that in order to measure the real Transit Time one has to know the time instant of the arrival of the light pulse at the cathode. This can be done using a PIN photodiode at the same position of the photocathode as a reference: the zero time is the time at which the PIN detects a light pulse. However usually one is interested in the Transit Time difference between several PMTs used. For this purpose, one can use an arbitrary reference (for example the time of the acquisition trigger of the DAQ system).

Transit Time Spread (TTS) The Transit Time Spread (also known as *time jitter*) is the TT fluctuation observed within the same illumination conditions. The TTS is usually expressed as the FWHM of the pulse-time distribution (the same distribution from which one estimates the TT). The TTS limits the accuracy of

photomultiplier-based time measurements. The nature of these fluctuations has two main components. The first one is a "*chromatic* component" due to the initial velocity spread of electrons originated at the same point; considering two velocity components i.e. normal (v_n) and tangential to the cathode (v_t), both contribute to the transit time spread with the quantities:

$$\Delta t_n = \frac{1}{e\xi}\sqrt{2m_e\Delta E_n} \quad \Delta t_t \approx \frac{r}{v} \tag{4.8}$$

where ξ is the electric field strength (so the high voltage supplied), r is the radius of the electron scatter and v is the impact velocity on the first dynode. The second component is the *geometrical* one for electrons originated from different points on the cathode. The other contributing factor is the inhomogeneity of the electric field in the focusing region. The arrival time difference of two electrons emitted with zero initial velocity and guided by an electric field ξ along paths of length L and $L + \Delta L$ is:

$$\Delta t = \Delta L\sqrt{\frac{m_e}{2e\xi L}} \tag{4.9}$$

From equations (4.8), (4.9) it is clear that the TTS can be decreased by increasing the electric field strength at the cathode surface or by minimizing the electron path differences; the latter is achieved employing concave cathode or more focusing electrodes that create shaped electric field lines. Increasing the voltage applied to the PMT can be also an easy way to increase the electric field at the photocathode. Indeed the TTS varies as the inverse square root of the HV.

4.2.2 Dark Rate

The PMT background noise present even in the condition of total darkness is the Dark Current. It is important since it imposes limitations on the detection of very low energy radiation. Observation of the Dark Current reveals several pulses: these are the Dark pulses and can be caused by

- **Thermionic Emission** of electrons from the photocathode and from dynode; the dark pulses are of the single p.e. type. This is the predominant cause of dark current and determines the dependence of the dark rate from temperature as shown in figure 4.5;
- **Field Effects** linked to the emission of some electrons because of the inevitable roughness of the electrodes;
- **Leakage Current** due to the surface conductivity of the electrodes;
- **Background Radiation**: high energy charged particles (*e.g.* cosmic muons) can give rise to Cherenkov radiation on the tube window. The produced photons can eventually cause the photoemission. Due to the relatively high light yield of the Cherenkov effect the consequent pulses have high amplitude. The background radiation can be caused also by the radioactivity of the PMT material (presence of ^{40}K).

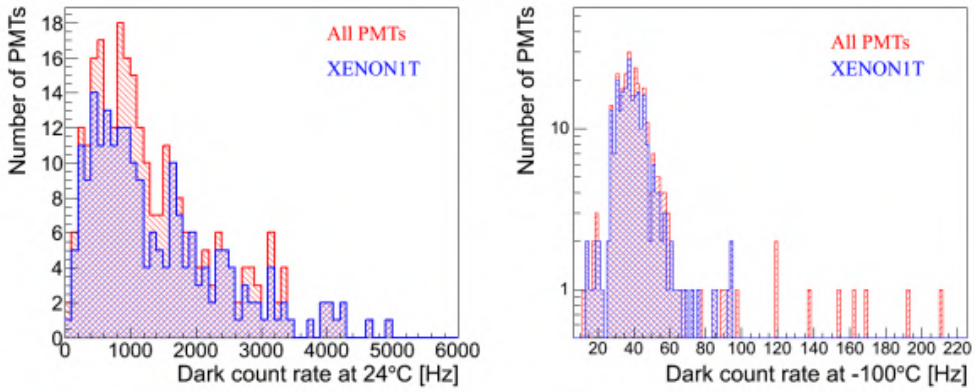

Figure 4.5: The distributions of the dark counts for the XENON1T PMT installed inside the TPC show the dependency of the DR from the temperature. These PMTs were tested both at room temperature (left) and at -100°C (right) in view of their future installation inside the cryogenic LXe. The thermionic emission is the main component of the DR which is drastically reduced operating at low temperature (right) [105].

The rate of the Dark Current pulses *i.e.* the *Dark Rate* (DR), is an important PMT characteristic that is always reported in the data-sheet; it is measured at a specific HV, temperature and with reference to a specific threshold (usually expressed in terms of a fraction of photoelectrons). The DR varies also according to the tube's history, *i.e.* the past storage and illumination conditions. Indeed, the exposure to uncontrolled light e.g. the ambient light tends to increase the dark rate because of the excitation of the photocathode itself, even without supplied voltage. However, the dark rate returns to the nominal value after storage in a dark state for one or two hours; in any case, the exposure to extremely intense light should be avoided since it can cause unrecoverable damage. The DR can be used to give an estimation on the fake coincidence when one operates with N PMTs, with the same Dark Rate R_{DR} for a given threshold *e.g.* 0.5 photoelectrons. By requiring a coincidence of k PMT within a time interval Δt the fake-rate is :

$$R_{fake} = \frac{N!}{(N-k)!\ k!}\ k\ R_{DR}^{k}\ \Delta t^{k-1} \tag{4.10}$$

For example, in the XENON1T Muon Veto conditions, with a trigger of 4 PMT in coincidence within $\Delta t = 300$ ns and an average DR (in the single p.e. threshold) of 1.26 kHz [107], the fake-coincidence rate was around ~ 0.6 Hz [69]. Using the same time window but with a PMT dark rate of 2.37 kHz (which is the DR value of the nVeto PMTs, see section 5.4) the rate of PMT fake coincidence as a function of the PMT multiplicity for the nVeto are shown in figure 4.6. Thus in order to have a fake event rate of the order of 1 Hz we need to require at least 5 PMTs in coincidence. In the nVeto it is planned to require a 10-fold coincidence to reach a tagging efficiency at least of 85%. Thus the dark rate contribution to the fake rate will be negligible (Section 3.1), considering the dark rate value that comes from the PMT test (discussed in the next chapter) and the main contribution to the fake events will come from the nVeto background (Figure 3.5).

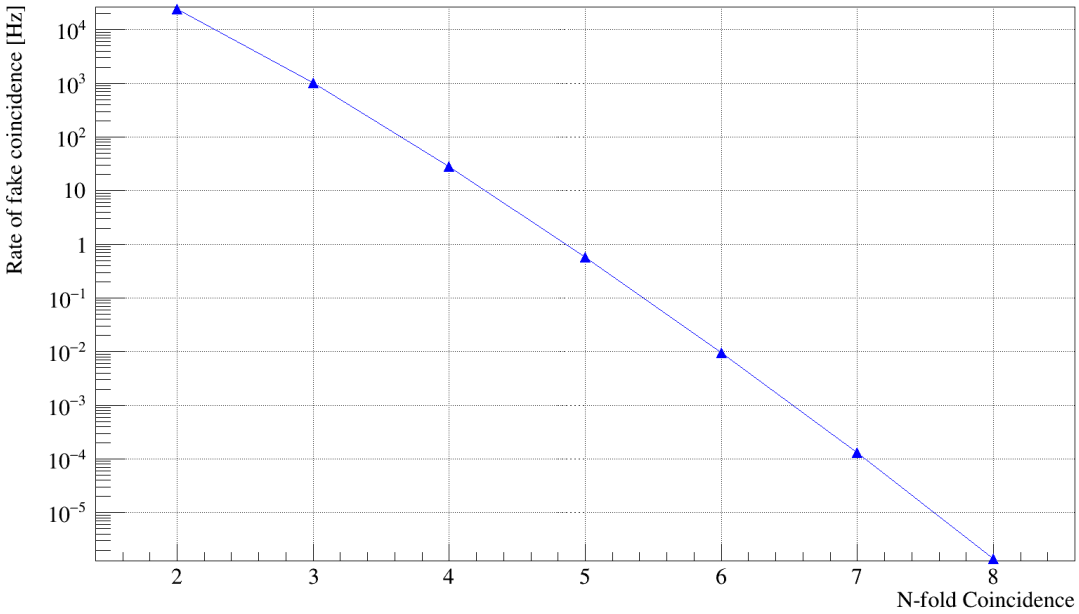

Figure 4.6: Rate of fake events [Hz] as a function of the number of PMTs required in coincidence. The rate values are calculated from Eq.4.10 with a $R_{DR} = 2.37$ kHz which is the mean DR of the nVeto PMTs obtained by the Small Water Tank measurements (Section 5.4).

4.2.3 Afterpulses

The afterpulses are spurious pulses that can appear after the signal output pulse (for these reasons are called *after*-pulses). In the recognition of afterpulse is important the time with respect to the main pulse. Even if often some pulses come with a very short delay[2], in general with "afterpulses" one refers to the long-delayed ones, which are originated by the ionization and drift of the residual gas inside the tube. The presence of this residual gas inside the PMT, although the efforts in creating the vacuum inside, is mainly due to the materials of the structure or to the helium that penetrates through the glass. Ions like H_2^+, He^+ and CO_2^+ are generated by primary photoelectrons in the optical input region and drift towards the photocathode, where they can cause emission of additionally delayed photoelectrons [115]. The transit time of these ions depends on the mass-charge ratio and thus from the afterpulse time one is able to distinguish the molecule of gas that caused it. Usually, the time distance between the main pulse (also called *prompt*) and the afterpulses is on the order of $\mathcal{O}(\mu s)$ and is given by

$$t = \int_{s_0}^{L} \frac{1}{v} ds = \sqrt{\frac{m}{2q}} \int_{s_0}^{L} \frac{1}{\sqrt{V(s_0) - V(s)}} ds \approx \sqrt{\frac{2m}{qV_0}} L \tag{4.11}$$

where L and V_0 are respectively the distance and the high voltage between the cathode and the first dynode, while s_0 is the ionization point where the ion generating the afterpulse is created. The last approximation is linked to the assumption that

[2]originated by photons, emitted by the collision of the electrons with the electrodes, hitting the photocathode.

$V(s) = V_0(1 - \frac{s}{L})^2$ which is valid for a hemispherical PMT. Furthermore, for this assumption, the arrival time of the afterpulse is independent of the ionization position.

4.2.4 External Factors

Environmental factors, such as the temperature, the presence of magnetic fields and the background radiation can affect the PMT operation.

Temperature The temperature variations can affect different characteristics of the PMTs, such as the spectral response, the gain and the dark rate. In general, inside the limits specified by the data-sheet, it is a reversible effect. However, in some cases, it is possible to operate PMTs (properly designed) in extreme temperature conditions: this is the case of the photomultipliers inside the XENON Time Projection Chamber. The temperature is not the only parameter that can affect the performances; also the humidity and the ambient pressure must be taken into consideration and monitored.

Magnetic Field The presence of a magnetic field, even as weak as the Earth's one (which is around 0.5 G [116]) affects the PMT performances. This effect can be seen by rotating the PMT main axis horizontally[3] as shown in figure 4.7. This influence is due to the effect of the field on the electron trajectories and the

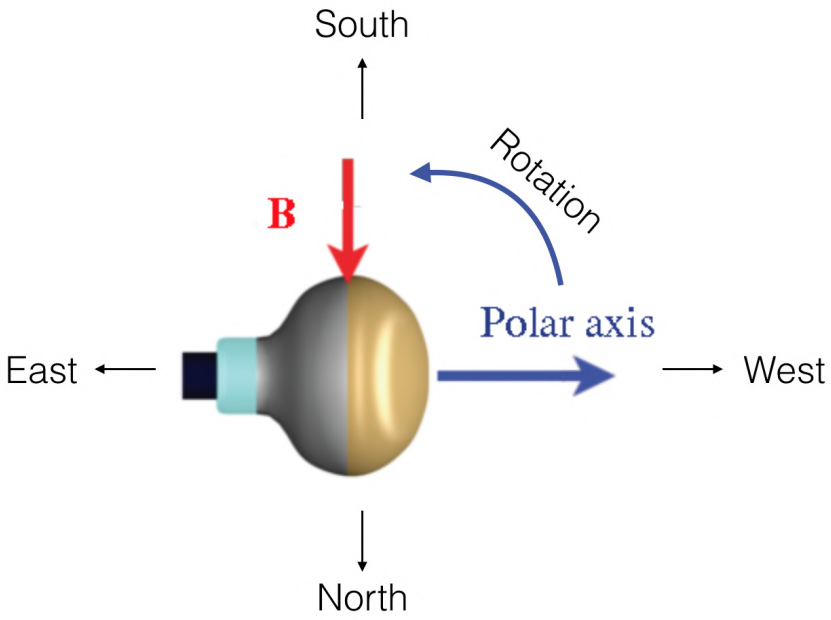

Figure 4.7: Draw of the PMT rotation around the main axis. Changing the direction of the polar axis towards the cardinal point, effects on the PMT performance can be measured [117].

[3]even if small performance variations can be measured with the rotation about the Polar axis

corresponding variation of collection efficiency in all stages; however the major contribution is expected in the electron optical input region. The magnetic field influence depends mainly on the voltage across the input system; as it increases, the electrons energy increases and so the sensitivity decreases. In order to reduce and eventually remove at all the magnetic field influence, it is possible to install a mu-metal shield around the PMTs [115, 117]. A study of this application was done for the Neutron Veto PMTs following a similar procedure employed in some tests performed for the Daya-Bay experiment [118].

External Radiation An usage of the PMT in the presence of ionizing radiation gives rise to secondary effects as the dark rate increase. The background radiation has two causes: the *scintillation* due to the interaction of α or β radiation (emitted by the material of the glass) with the glass itself, or the *Cherenkov effect* of charged particle traversing the input window. Another contribution is linked to the so-called *spallation noise* of cosmic rays that interact with structural material. In the most common applications of the PMTs in underground experiments, this effect is negligible.

4.3 Photomultipliers in the XENON experiment

Photomultipliers are widely used in XENON detectors. They can be found inside the Time Projection Chamber, the Muon Veto and, in XENONnT are the key component of the Neutron Veto System. These PMTs have disparate characteristics in order to accomplish the different requirements and operative conditions.

4.3.1 PMT R11410-21 for the Time Projection Chamber

The signals from the XENONnT TPC are recorded by a total of 494 Hamamatsu R11410-21 PMTs, installed both on the top array and the bottom array similarly to the XENON1T case showed in 4.8.

Figure 4.8: Picture of the top (left) and bottom (right) array of PMTs before the installation in the XENON1T detector [105].

The highly radiopure PMTs have 3-inches diameter and were jointly developed by Hamamatsu and the XENON Collaboration [119]. All the PMTs that are mounted in the XENONnT TPC have been tested in liquid Xenon in terms of

gain calibration, afterpulses, dark count rates and stress tests (in order to calibrate the high illumination response). The PMTs photocathode is made of bialkaly-LT. Furthermore, they feature an average quantum efficiency $\geq 28\%$ at 178 nm and a 90% of collection efficiency for that wavelength [105]. The gain of all the 12 dynodes PMTs is around $\sim 6 \times 10^6$ at 1500 V of HV, the DR is negligible because of the temperature conditions (Figure 4.5), which are around $-110°C$. In the characterization of these photomultipliers a key role is represented by the analysis of the afterpulse rate and their evolution; the appearance of Xenon lines in the afterpulse spectrum indicates the presence of small leaks. Based on the test performed and on the specification provided by Hamamatsu the tubes will be distributed inside the XENONnT TPC into arrays following the same criteria of the XENON1T TPC; the PMTs are placed in order to have higher Quantum Efficiency at the center where most of the photons are supposed to arrive [105].

4.3.2 PMT R5912-ASSY for the Muon Veto

The photomultipliers of the Muon Veto (Figure 4.9) are of different dimensions and characteristics. The MV water Cherenkov detector is instrumented with 84 PMTs Hamamatsu R5912-ASSY with 8-inches of diameter (Figure 4.10) [107].

They feature a high quantum efficiency (around 30% in the wavelength range $[300, 600]$ nm) and a typical gain of 6×10^6 at Nominal High Voltage. All the PMTs that are installed in the Muon Veto have been tested both in air and water in 2013 at the Laboratori Nazionali del Gran Sasso with the so-called *Small Water Tank test* (further details in the next chapter). Also in this tests the afterpulses were monitored in order to verify the absence of water leak. During the XENON1T data-taking, each PMT was weekly calibrated at the single pe level; the same

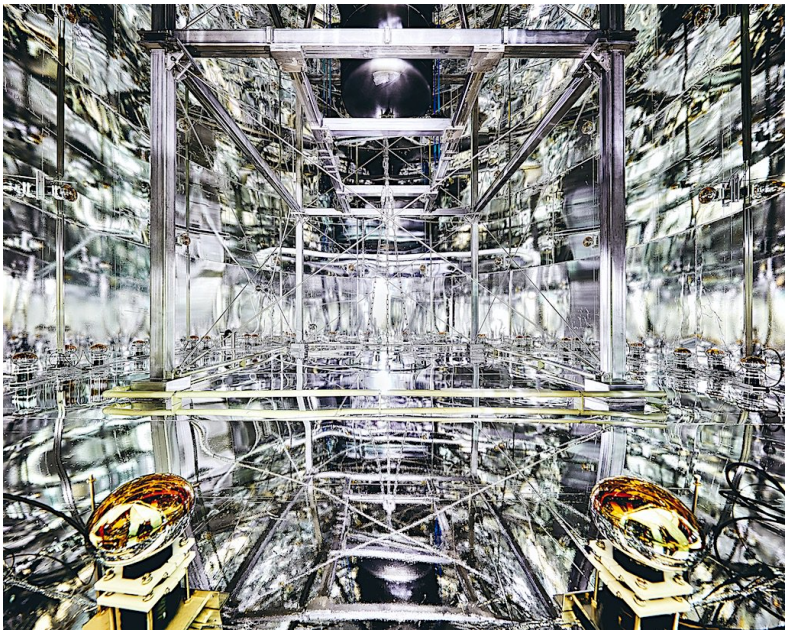

Figure 4.9: Picture inside the Muon Veto covered with the reflective foil and with some PMTs visible.

procedure will be adopted for the XENONnT operations.

4.3.3 PMT R5912 for the Neutron Veto

The 120 PMTs that will be mounted in the Neutron Veto share similar characteristics to the ones already installed in the Muon Veto (Figure 4.11).

However, there are some differences, like:

- Coaxial cable with separate grounding for signal and high voltage cable;
- Higher quantum efficiency (Figure 4.12);
- Lower radioactivity (Table 4.1);
- Different dumping and protective resistors which are used in the resistors chain: this allows for reducing the reflection of the signal and for slightly improving the gain.

PMT Radioactivity [Bq/PMT]						
	Without glass		Standard glass		Low Rad. glass	
	Nominal	LNGS	Nominal	LNGS	Nominal	LNGS
^{40}K	0.6	0.08	4.7	2.4	0.8	0.6
U-series	<0.1	<0.05	2.4	2.26	0.4	<0.6
Th-series	<0.1	0.008	2.0	1.58	0.3	0.425

Table 4.1: Comparison between the values of the PMT radioactivity stated by Hamamatsu and measured with the Ge detector available at LNGS. In particular, the glass of two broken PMTs (featuring different glass material) was isolated from the PMT body for the measurement. The values, expressed in [Bq/PMT], for the ^{40}K and the U/Th-series are shown. The employment of a low radioactivity glass in the nVeto PMTs, will mitigate the radioactive background.

As for the MV case the location of the PMTs on the nVeto structure was decided with Monte Carlo studies (Section 3.2). The nVeto PMTs have had to pass the

Figure 4.10: Picture of a R5912 PMT from [120].

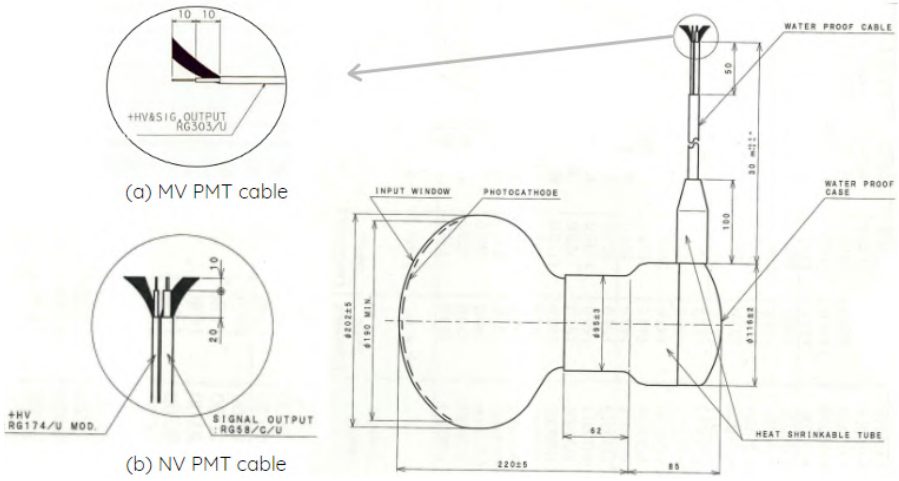

Figure 4.11: Schematic of the PMT R5912 from Hamamatsu data-sheets. Together with the components and materials of the PMT it is shown also the configuration of the cables. Each PMT has a signal and a high voltage cable. The Muon Veto PMTs features a common ground between signal and HV (top left) while in the nVeto case the two cables have separated coaxial ground (bottom left); the latter configuration tends to reduce the electronic noise (which mainly comes from the HV modules).

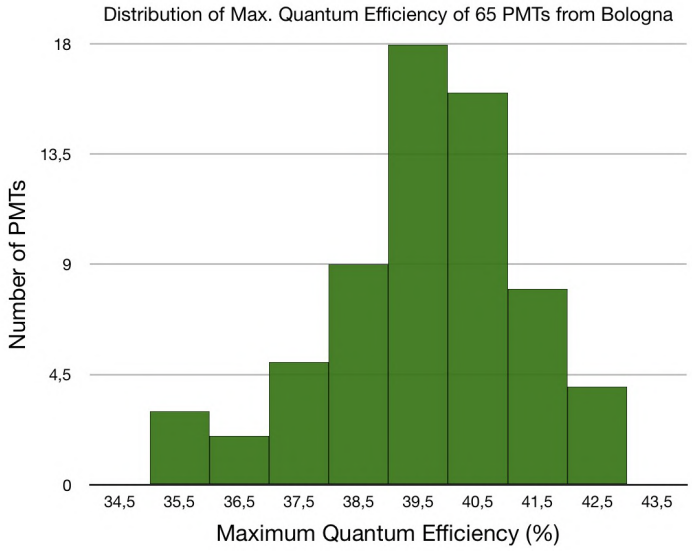

Figure 4.12: Distribution of the maximum Quantum Efficiency of 65 nVeto PMTs (which are those bought by the Bologna group and whose values were provided by Hamamatsu). The mean value is attested around 40.5%.

same Small Water Tank test conceived for the Muon Veto PMTs; the gain, the dark rate, the afterpulses, and the timing characteristics, *i.e.* transit time and the transit time spread have been measured. The detailed description of the experimental setup and the results of these tests is the subject of this thesis and is the topic of the next chapter.

Chapter 5

The Small Water Tank test

The Neutron Veto photomultipliers are the key components of a part of the XENONnT experiment necessary to complete the radiogenic background mitigation. Indeed, the Neutron Veto (nVeto) will be instrumented with 120 high-QE low-radioactivity Photomultiplier tubes (PMT) to detect the Cherenkov light emitted after the neutron capture on gadolinium and water. 125 PMTs were bought in order to have at least 5 spare PMTs.

While the information about these PMTs are reported in the section 4.3.3, the setup and the measurements performed are discussed in this chapter. The tests were done at Laboratori Nazionali del Gran Sasso with the aim of characterizing and calibrating the XENONnT nVeto PMTs. All the PMTs were tested both in air and in water with the so-called *Small Water Tank* setup (Section 5.2).

5.1 Test of 125 photomultipliers for the Neutron Veto system

In view of the future installation of the R5912 Hamamatsu PMTs inside the nVeto of the XENONnT experiment, tests were carried out to characterize the PMTs' response. By characterization of photomultipliers we intend to measure the main operating parameters (Section 4.2) such as:

- the gain and its stability over the time;
- the dark counts rate at different thresholds.

Even the afterpulses were monitored and the analysis is almost completed. As it will be reported in Section 5.2.3, during the tests, very fast digitizers were used; thus we were able to perform some non-trivial measurements like:

- the transit time difference between the PMTs;
- the transit time spread.

Additionally, we were able to quantify the Earth's magnetic field influence on the PMTs behavior and to study whether this influence can be mitigated by the installation of a mu-metal magnetic shield.

5.2 Experimental setup

The tests of the 125 Hamamatsu PMTs were performed in a dedicated area, the so-called *Hall di Montaggio* (Figure 5.1), in the above-ground site at the Laboratori Nazionali del Gran Sasso (LNGS). In this section it is described the setup for all the different kind of measurements performed.

Figure 5.1: Photo of the area in the Laboratori Nazionali del Gran Sasso dedicated to the nVeto PMT test. The white tank in the middle is the light-tight Small Water Tank used to contain the PMTs.

5.2.1 The Small Water Tank

The *Small Water Tank* (SWT) is a cylindrical polypropylene light-tight tank of 1 m height and 1.7 m diameter (Figures 5.2, 5.3) with the inner surface covered by a black PVC layer for the light absorption.

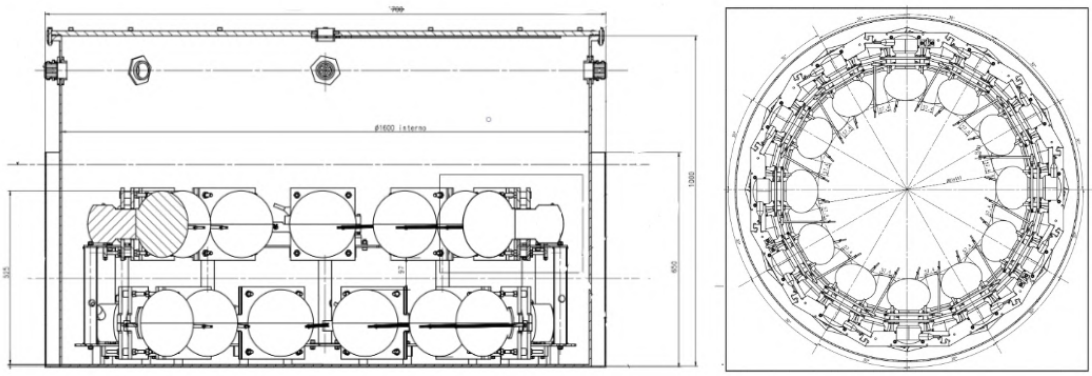

Figure 5.2: Drawings of the Small Water Tank with the PMT structure inside.

It was designed and manufactured in Bologna on the occasion of the Muon Veto PMT tests [107] performed in 2013; basically most of the procedures and some of the setup components, as the tank itself, have been inherited from that test. On the lateral side of the SWT there were several *feed-through* (Figure 5.3 (right)), used to

Figure 5.3: Photo of the Small Water Tank with the zoom on the feed-through (right) used to pass the PMTs' cables.

pass both the 30 m PMTs' cables and the optical fibers for the LED calibration[1]. In addition, in the middle of the tank cover, there was a feed-through for the diffuser ball (see section 5.2.2). The SWT was also supplied with a connection for the filling/emptying of ultra-pure water; the latter was stored in the blue tank visible in figure 5.1.

Support Structure Inside the Small Water Tank a stainless steel support structure was used in order to accommodate the PMTs (Figure 5.4).

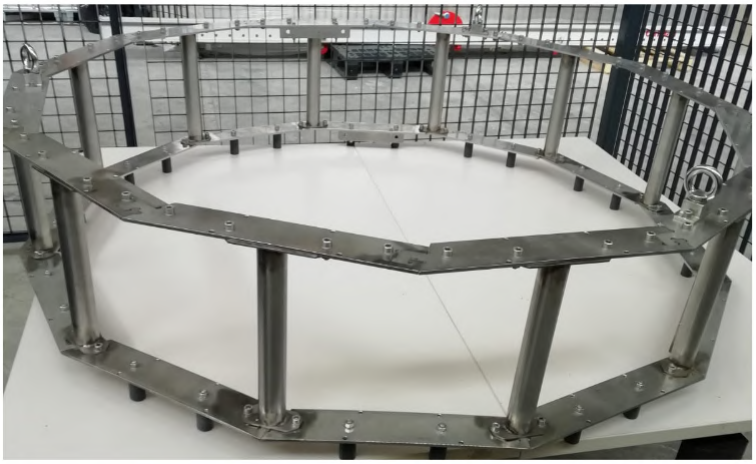

Figure 5.4: Photo of the stainless steel support structure.

The structure (also designed by INFN Bologna) could accommodate, with a two ring disposition, 24 photomultipliers at a time, which were mounted on dedicated polyethylene PMT holders (Figures 5.5, 5.6). Most of the work regarding the assembly and disassembly of the photomultipliers concerned the passage of cables

[1] and the additional ones were covered in order to ensure the light-tightness

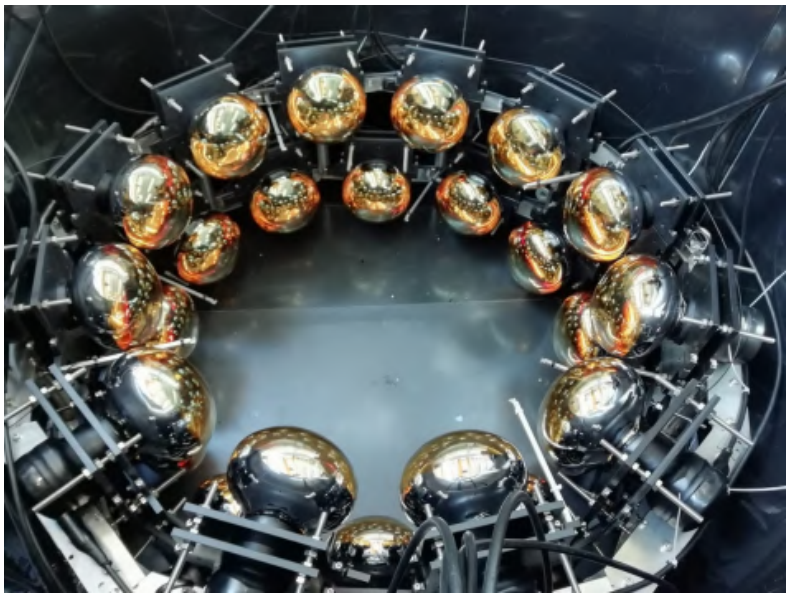

Figure 5.5: Photo of the stainless steel support structure with the PMT installed on their polyethylene holders. The whole system is inside the SWT.

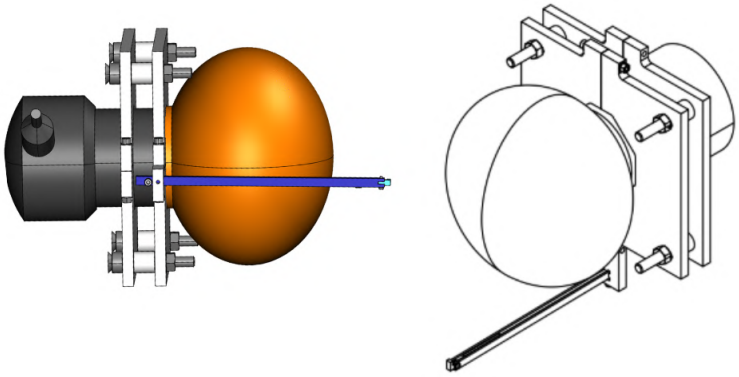

Figure 5.6: Drawings of the nVeto PMT with the polyethylene supports (white/grey) and the SS rod for the optical fiber (blue). At the end of the bar is located a small PTFE reflector (light blue) used to focus the light from the fiber on the PMT photocathode (orange).

through the feed-through and the raising/lowering of the structure in the SWT by means of a crane (Figure 5.7).

5.2.2 Calibration Setup

The calibration setup for the measurements of the spectral response of the photomultipliers exploits a *Diffuser Ball* paired with a LED box (emitting blue light with $\lambda = \sim 470$ nm). The diffuser ball is a 50 mm diameter PTFE hollow sphere filled with micro-glass bubbles (Figure 5.8); this property allows for a homogeneous diffusion of light inside the Small Water Tank. To make the PMTs receive the same amount of light, the diffuser ball was hanging in the middle of the structure. For the sake of measurement redundancy, optical fibers were installed on eight PMTs

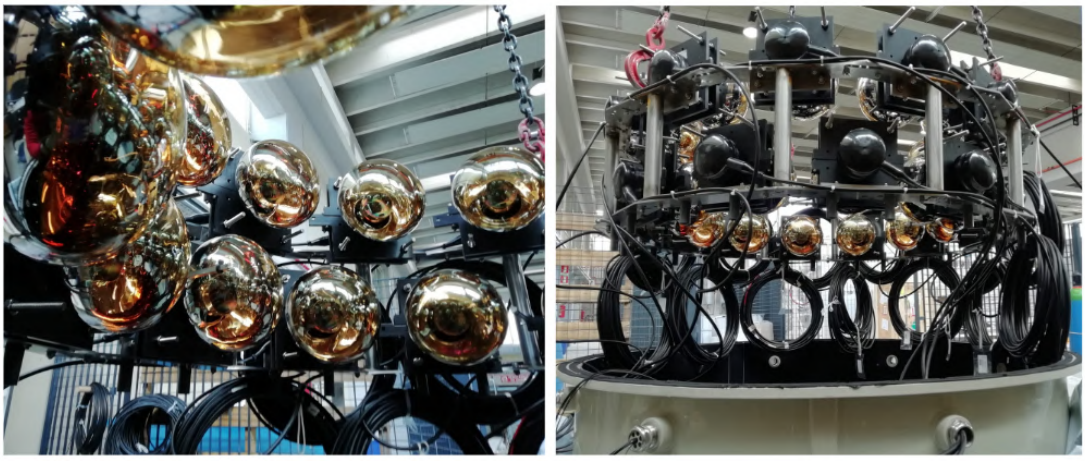

(a) (b)

Figure 5.7: Photos of the Small Water Tank with the PMT structure during the lowering operation.

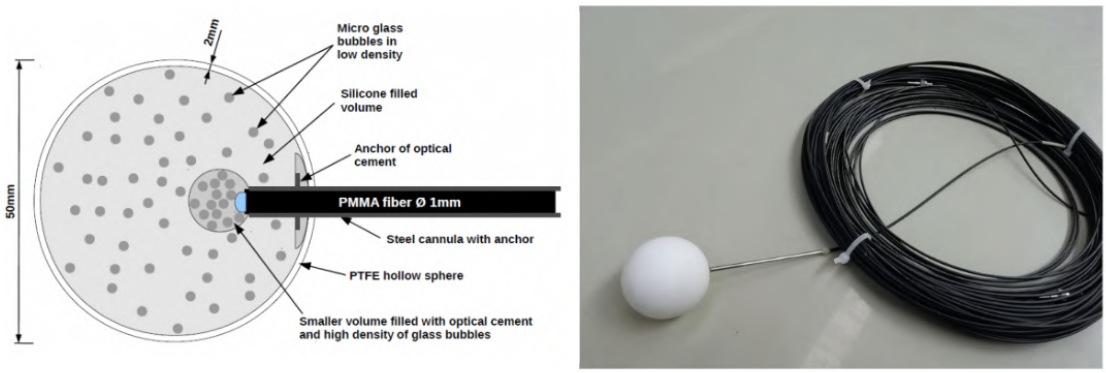

Figure 5.8: Scheme of the diffuser ball. A PMMA optical fiber goes inside the sphere and the light coming out from the fiber is diffused by micro-glass bubbles. It is possible to distinguish two areas of different bubble glass density.

using the interface shown in figure 5.6: a SS rod holds the optical fiber and at the edge, a PTFE reflector focuses light toward the PMT photocathode.

5.2.3 Electronics and DAQ

The electronics for the test, consisted of:

- One Mainframe CAEN Power Supply SY4527;
  - One Board A1535SP which provided 24 SHV Channels.
- HP PC Server with 2.2 TB storage disk;
- Pulser BNC Model 588 which provided both the signal for the LED and

the external trigger for the DAQ. It also sets the amplitude and width configurations for adjusting the light intensity from the LED;

  - 2 LED boxes (1 kOhm internal resistor, positive supply voltage).

- VME Crate;

  - one VME Crate controller through optical link card CAEN mod. A3818;
  - Four 8-channels Digitizer CAEN mod. V1751.

In figure 5.9 is summarized the electronic setup. The pulser (green on the top left) with its 8 programmable channels provided both the triggers to the LED boxes (connected to the two calibration systems) as well as the trigger for the DAQ. The TTL signal was first connected to a TTL-NIM converted module and the NIM output inserted in the TRG-IN channel of the first digitizer (Board 0 - Master Board). Thus the daisy chain of the TRG-OUT/TRG-IN distributed the trigger to the other boards. Even the internal clock of the Master Board is distributed through a daisy chain to the Slave Boards (board 1-3). Each board featured 8 channels; since we had 24 PMTs for each bunch, three board (0-2) would have been enough. However, in order to study the trigger delay/jitter between the boards, a fourth digitizer was employed. Its channels were filled with the trigger signal (see section 5.5). All the boards were connected via an optical link (grey lines) to the PC server. It should be noted that, although this scheme was used for the main measurements, in some cases, e.g. the study of the PMTs' time characteristics, it was employed a slightly different setup (Section 5.5). Further consideration

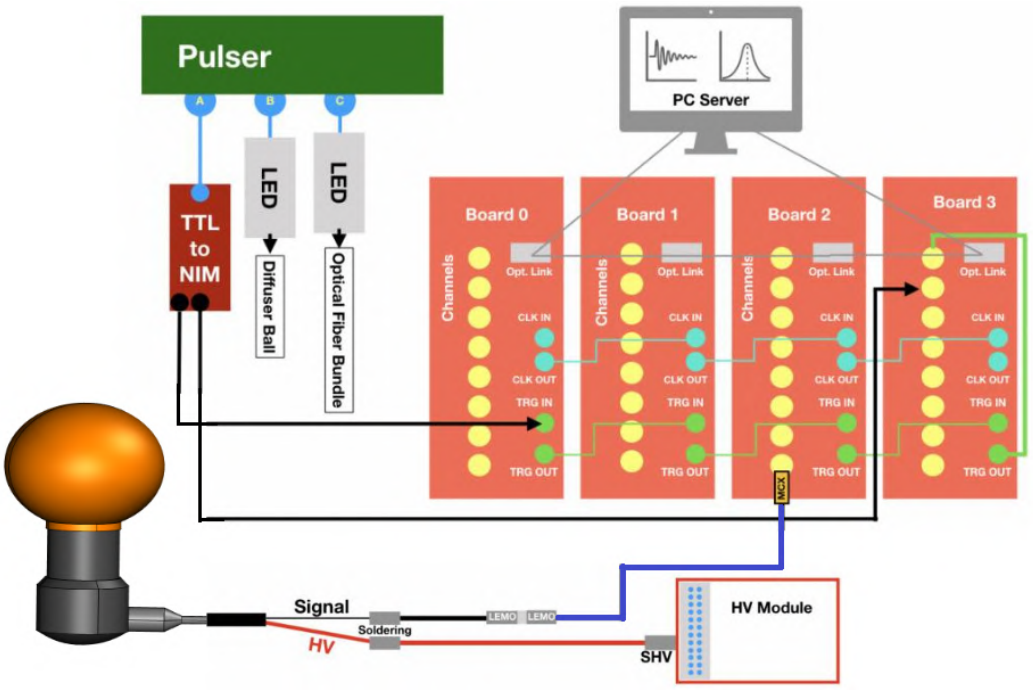

Figure 5.9: Schematic of the electronic setup employed for the main measurements in the SWT test.

regarding the preparation of PMT cables, the characteristics of the digitizers and the analysis software are necessary.

PMT cable preparation As reported in section 4.3.3 the cable of the PMT R5912 is a coaxial cable with different groundings for the signal and the High Voltage components. Several doubts have emerged regarding the best way to interface the signal and the power cables with the digitizers and HV board respectively since the PMTs came without any connectors. Due to technical difficulties related to the passage of PMT cables through the SWT feed-throughs, it was commonly decided to proceed as follows: starting from the PMT, its high voltage cable (red) was soldered to an SHV cable which had to be connected to the channel of the power supply module. On the other hand, the signal cable (black) was soldered with a lemo cable; in order to fit with the digitizer's channel, the lemo cable was extended with a lemo-MCX (blue) one. All these details are shown in figure 5.9. During the soldering operation, we paid attention that all 24 had the same length in view of the timing characterization of the PMTs.

Digitizer CAEN V1751 The digitizers CAEN V1751 employed for the data acquisition were the ones of the XMASS experiment provided by a Japanese group working either in Xenon and XMASS, and featured [121]:

- 1 GS/s (Giga-samples per second) of acquisition frequency;
- 10 bit resolution;
- 1 V_{pp} (peak-to-peak) of dynamic range;
- 125 MHz of internal clock frequency.

The amplitude resolution of these digitizers, given by:

$$\left.\begin{matrix}10 \text{ bit} \\ 1 \text{ V}\end{matrix}\right\} \Rightarrow 1 \text{ ADC Count corresponds to} \rightarrow \frac{1 \text{ [V]}}{2^{10}} = 0.97 \text{ mV} \tag{5.1}$$

is low but somehow compensated by the 1 ns time resolution when one integrates in order to obtain a charge signal; in that case the resolution becomes:

$$\Delta Q = \frac{0.97 \text{ mV} \times 1 \text{ ns}}{50 \text{ Ohm}} = 0.019 \text{ pC}. \tag{5.2}$$

The results of the test led to the decision regarding the digitizers to be used for the nVeto signals acquisition; in the end not being able to renounce to the temporal characterization of the neutron veto events and, wishing anyway to exploit a good resolution in terms of amplitude, we will install different digitizers. In the final configuration, it is foreseen the employment of the digitizer V1730 featuring 500 MHz of ADC frequency, 16 channels, 14 bit of resolution and a 0.5 and 2 V_{pp} selectable input dynamic range with programmable DC offset adjustment. For these tests, we exploited all the digitizer V1751 features, in particular for the timing measurements (TT, TTS). Another feature very useful of fast digitizers like the V1751, is the possibility of Zero Length Encoding suppression, which reduces the size of the RAW data by avoiding to keep the samples under a threshold.

Analysis Software The acquisition of the raw data of each board as well as their conversion into `rootfiles` ready for the analysis, was the task of a C++ software, which included CAEN libraries. After every measurement, we took care of a fast inspect of the data-quality through C++ scripts. We have also developed `bash jobs` with the aim of monitoring the behavior of PMTs, to be launched in dead times (at night or on weekends). Those jobs were responsible for starting acquisition runs in a loop (generally one run every 4 hours).

5.2.4 Test schedule and plan

The real test schedule started after a "setup preparation campaign" lasting approximately two weeks. The stainless steel structure inside the Small Water Tank could accommodate 24 photomultipliers; therefore we organized the 125 PMTs in several groups. We decided to keep monitoring two photomultipliers (the so-called *reference* PMTs) for the entire period of the test. Considering this, six bunches were tested in total, but during the last one, we tested just 13 new PMTs out of 24. Thus, the free holders in the sixth bunch were used to retest some PMT that had presented ambiguous behavior in the previous bunches and to carry out additional measurements (such as the influence of the Earth's magnetic field reported in section 5.6). Each bunch required almost two weeks of work between the mounting phase, measurements (in air and in water) and dismounting phase, for a total duration of three months from April to June. We managed to successfully observe the tight schedule planned by the XENONnT collaboration.

The assembly phase consisted of the following steps:

- mounting of the PMTs on the support structure using the polyethylene supports and coverage of the PMTs with black bags (to avoid intense lighting exposure);
- lifting of the structure with the crane on the top of the SWT (Figure 5.7a);
- passing the 30 meters of cables through the SWT feed-through;
- lowering of the structure inside the Small Water Tank and removal of the black bags;
- Small Water Tank lid closure and coating with a black sheet;
- cable preparation (welding) and connection to the power supply and to digitizers.

Of course, the mounting phase was preceded by the dismounting phase, characterized by more or less the same steps. The two phases required ~ 5 days. As soon as the assembly part was over and after the electronic check on the entire system, the measurement phase started with a duration of almost 9 days. An accurate description of the measurements performed is reported in the following sections.

5.3 Gain measurements

The gain is a key parameter for the characterization of the photomultipliers behavior. On the data-sheet of the R5912 PMTs purchased one can found the *Nominal High Voltages* (NHV) *i.e.* the high voltage values required for a gain of 1×10^7. However, due to the dispersion of the signal in the 30 m of PMT cable, the gain values measured at the NHV differed from the Hamamatsu stated ones. The gain measurements for every photomultiplier were also oriented to monitor the stability of this parameter and to check possible variations in water, in view of the installation in the long term final configuration inside the Neutron Veto. The high voltage dependence of the gain was also studied and the calibration curves measured; the latter will be very useful during the PMT installation in the final setup.

5.3.1 Single Photoelectron Run

We used to call *single photoelectron* runs the LED runs dedicated to the gain measurements. These were characterized by an illumination such that only one photoelectron is emitted at the photocathode. The illumination was mainly provided by the diffuser ball, but as a cross-check also the optical fibers were employed on eight PMTs. The acquisition characteristics were the following:

- Acquisition Window of 1 μs;
- Trigger Rate of 1 kHz;
- 100k Events;
- No Zero Length Encoding suppression.

For each event the waveform was produced; a typical single p.e. waveform is shown in figure 5.10. From the integration of the signal in the expected region, one obtains the charge of the event. The integration is made starting from the calculation of the *baseline* obtained averaging 100 samples before the signal integration region (red line in figure 5.10). In this way, we got rid of the low-frequency environmental noise that was constantly present in the Hall di Montaggio area. Since we knew the light pulse timing (from a check with the oscilloscope), it was easy to define a window for the peak finding algorithm: the peak was defined as the minimum value of the waveform inside the [650, 720] ns. Thus the integration window was defined as $[-10, +64]$ ns starting from the minimum (Figure 5.11).

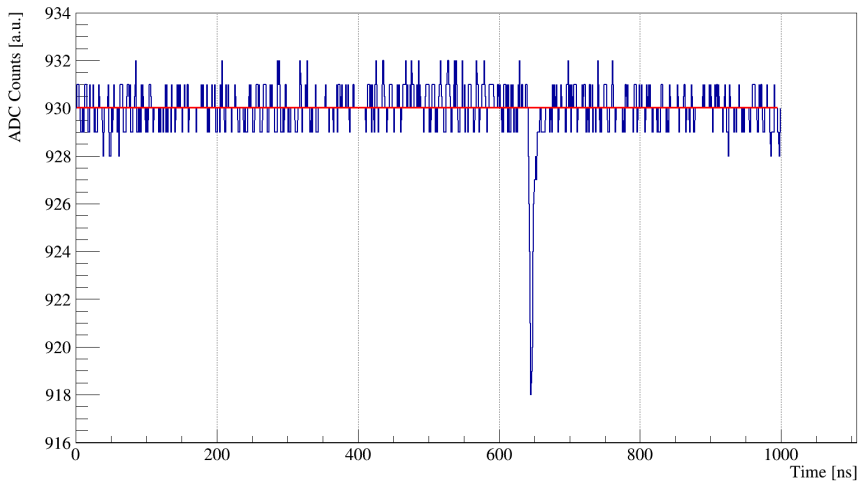

Figure 5.10: Typical signal waveform of one PMT recorded with a single p.e. run. The duration of each event was 1 μs. On the y-axis are reported the ADC counts but since we know that for the digitizer employed 1 ADC Count $\approx$ 1 mV it is easy to find the corresponding voltage value. On the x-axis instead should be reported the sample number, but since we had a time resolution of 1 ns, one sample corresponds to 1 ns; thus the time is reported. The red line indicates the mean baseline which is used for the integration algorithm.

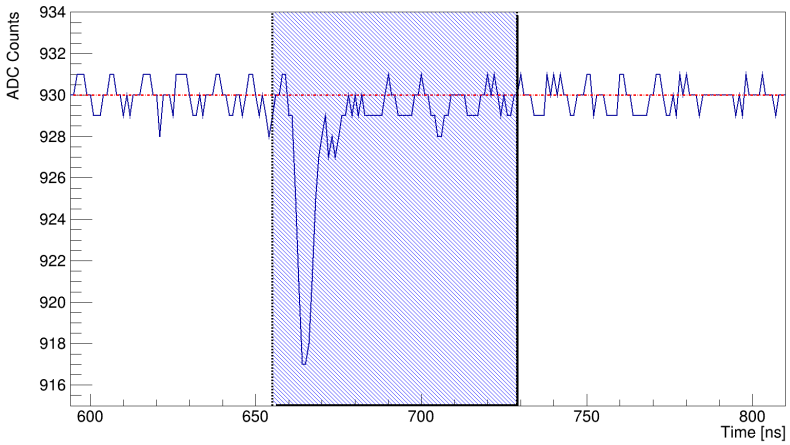

Figure 5.11: Zoom of the waveform shown in figure 5.10 with the [-10,+64] ns integration window highlighetd in blue.

The distribution of the integrating charge for all the 100k events, *i.e.* the single p.e. spectrum is shown in Figure 5.12.

We used to call this algorithm, used for the spe spectrum calculation, as the *SWT algorithm*. The integration window length came from an algorithm developed by XMASS colleagues to optimize efficiency in detecting a single pe. However, we have also studied the efficiency of the algorithm by changing the integration window. Figure 5.13a shows a comparison between two charge spectra obtained with two different windows and algorithms. In particular, figure 5.13a shows the comparison within the SWT algorithm of the windows defined by the extremes

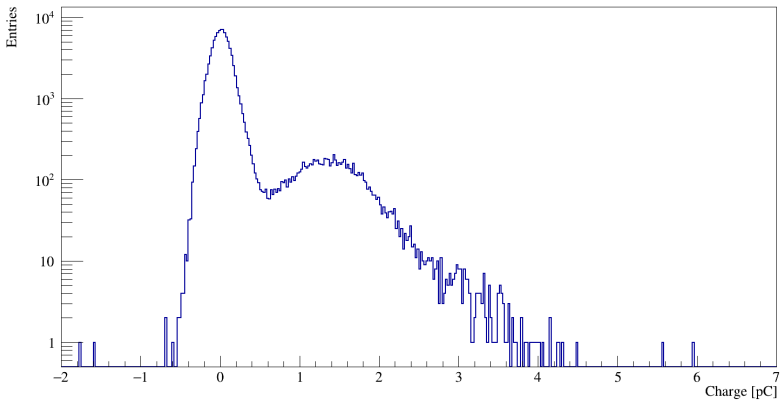

Figure 5.12: Charge spectrum of one PMT obtained by integrating all the 100k events of one run. The integration of the waveforms gives an (ADC Count × Sample) value; thus the charge is obtained by multiply the conversion factor {0.97 V/(50 Ohm × 1 ns)}

[-10,+64] ns (black) and one of [-6,+40] ns (red). On the other hand figure 5.13b shows the comparison between the SWT algorithm with [-6, +40] ns and the XMASS algorithm with [-10, +64] ns; the XMASS algorithm is different from the SWT one because of the presence of a threshold for the peak finding algorithm. Thus the charge spectrum shape results differently. From the comparison in figure

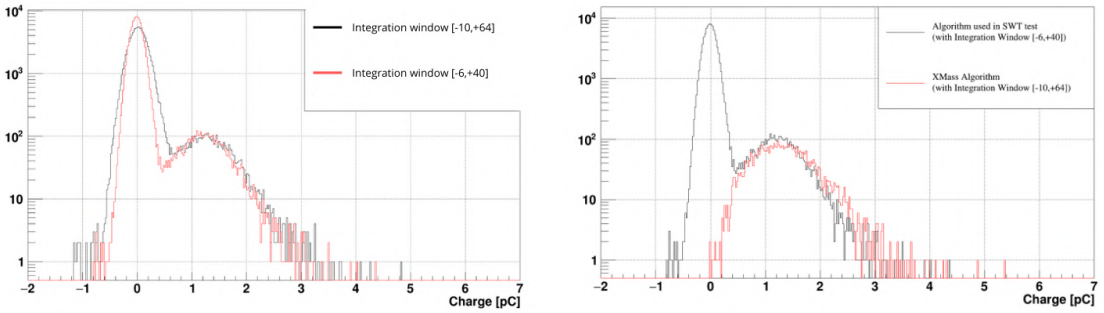

(a) (b)

Figure 5.13: (a) Comparison of two charge spectrum obtained with different integration windows (the SWT standard window [-10,+64] ns and the [-6, +40] ns window are shown as a reference). (b) Comparison between the SWT algorithm and the XMASS algorithm. The latter is used as a reference for evaluating the efficiency of the integration windows of the SWT algorithm. Here the comparison with the [-6, +40] ns is shown as a reference.

5.13b the efficiency of the integration window is evaluated by plotting the ratio between the black histogram and the red one:

$$\text{Efficiency} = \frac{\text{SWT histogram}}{\text{XMASS histogram}} \tag{5.3}$$

in each bin. Figure 5.14 shows, as reference, the plot obtained in this way for the window [-6,+40] ns. The plot is fitted with the *error function*:

$$f(x) = \frac{1}{2}\text{erf}\left(\frac{(x - p_0)}{p_1}\right) + 1 \tag{5.4}$$

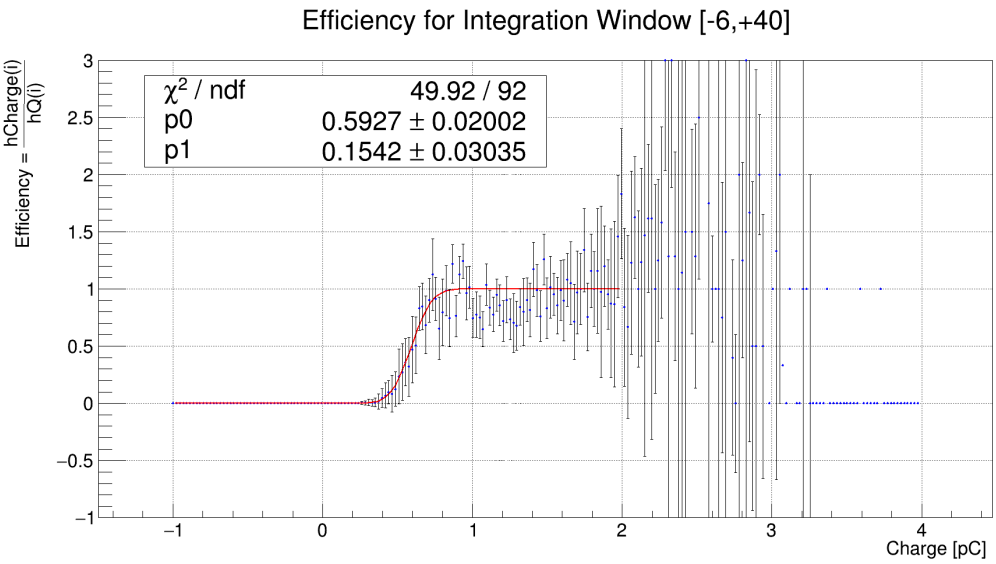

Figure 5.14: Plot of efficiency obtained from Eq. (5.3) for the integration window [-6,+40] ns shown as reference. The parameter of the red fit function (Eq. 5.4) are also reported.

with p_0 and p_1 free parameters. The results for almost all the windows tested are shown in figure 5.15. The most efficient time window (*i.e.* the "first curve" reaching

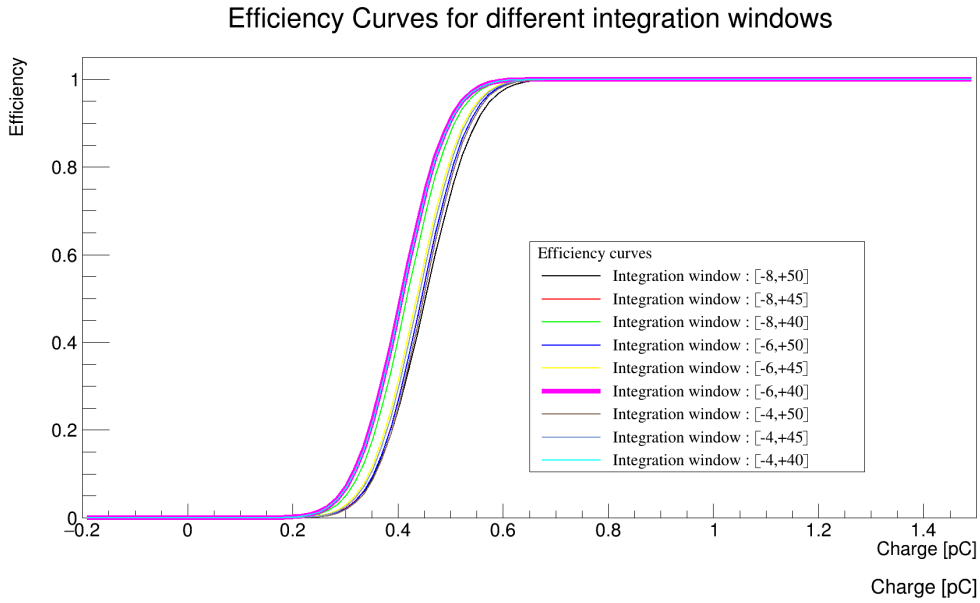

Figure 5.15: Graph of the error functions used for the fit for some of the integration window tested. In particular here were already selected the ones giving higher efficiency. The curve for the [-6, +40] ns window is highlighted, resulting to be the best from the comparison.

the maximum of efficiency) resulted to be [-6,+40] ns, highlighted in pink. This window was used for the next analysis (such as for the DR) while for the gain we kept the first algorithm.

Going back to the single pe runs, every single pe spectrum (Figure 5.12) was fitted by a proper function (Figure 5.16); it consists mainly of a gaussian noise, called *pedestal*, centered in 0 pC (due to the fact that we were triggering the DAQ in an external mode) and of a second gaussian centered around the single p.e. charge value. With growing illumination, it is possible to distinguish also a third

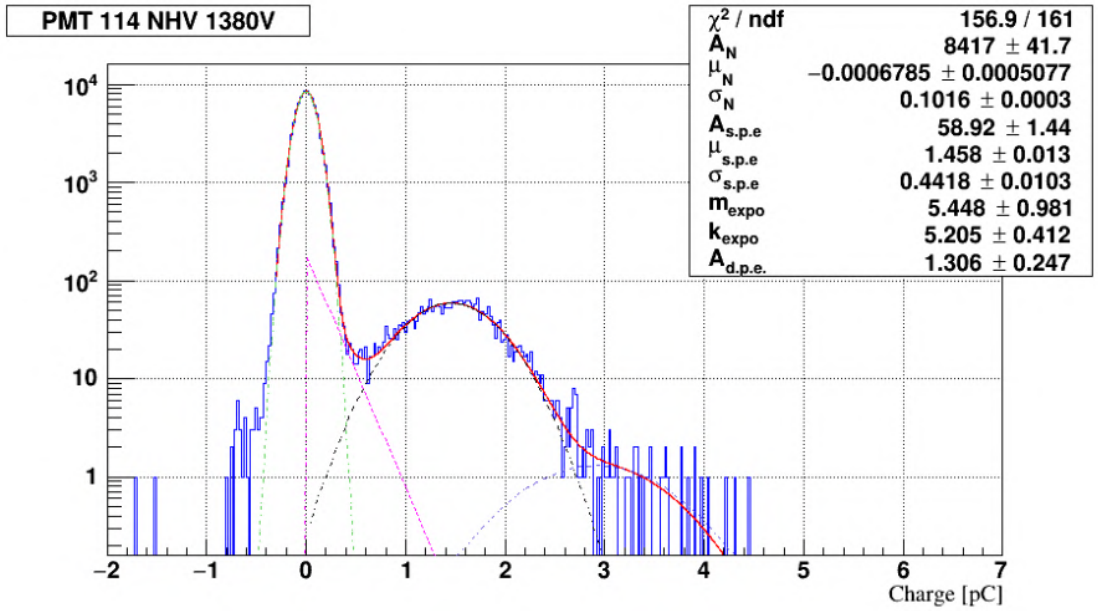

Figure 5.16: Fit of the charge spectrum of an spe run for the PMT 114, shown as a reference. The red curve is the fit function, convolution of the function reported with the colored dashed lines. The distribution shows at least two peaks. These are the spe peak, fitted with the black gaussian function, and the pedestal (noise) peak which is linked to the integration of the events without signals. The pedestal is fitted with the green gaussian function. Sometimes a third peak appears; it is linked to events where two photoelectrons are emitted from the photocathode, instead of one. The fitting function is again a gaussian highlighted in blue. In addition, there is an exponential function (defined for Charge ≥ 0) colored in pink, to account for the sub-amplified electrons. All the fit parameters and the χ^2 are also reported.

gaussian peak that takes into account the double photoelectrons contributions and whose parameters are constrained by the ones of the single pe function. Finally, the exponential function takes into account the sub-amplified electrons' contribution. Usually, it is associated with the photoelectron energy loss for the inelastic scattering on the first dynode; the electrons produced have low energy, causing a sub-amplified signal at the end of the chain. A similar effect is also caused by the photoelectrons that skip one dynode of the chain. The composed fit function reads

$$f(x) = A_{ped} e^{\frac{-(x-\mu_{ped})^2}{2\sigma_{ped}^2}} + \left(e^{-p_0 x + p_1} + A_{spe} e^{\frac{-(x-\mu_{spe})^2}{2\sigma_{spe}^2}} \right) \Theta(x) + A_{dpe} e^{\frac{-(x-2\mu_{spe})^2}{2(\sqrt{2}\sigma_{spe})^2}} \quad (5.5)$$

where:

- A_{ped}, μ_{ped} and σ_{ped} are the normalization constant, mean value and standard deviation of the pedestal ;

- A_{spe}, μ_{spe} and σ_{spe} are the normalization constant, mean value and standard deviation of the single p.e. peak;
- p_0 and p_1 are the exponential parameters;
- A_{dpe}, $2\mu_{spe}$ and $\sqrt{2}\sigma_{spe}$ are the double p.e. parameters, of which only the first one is a free parameter;
- $\Theta(x)$ is the Heaviside function.

The gain values are obtained from the fit parameters, in particular from the μ_{spe} and the μ_{ped}:

$$G = \frac{\mu_{spe} - \mu_{ped}}{e} \tag{5.6}$$

where e is the electron charge. The error associated is given by the error propagation:

$$\Delta G = \sqrt{\left(\frac{\partial G}{\partial \mu_{spe}}\Delta\mu_{spe}\right)^2 + \left(\frac{\partial G}{\partial \mu_{ped}}\Delta\mu_{ped}\right)^2} = \frac{\sqrt{\Delta\mu_{spe}^2 + \Delta\mu_{ped}^2}}{e}. \tag{5.7}$$

The distribution of the gain values for the 125 PMTs at their NHV is shown in figure 5.17.

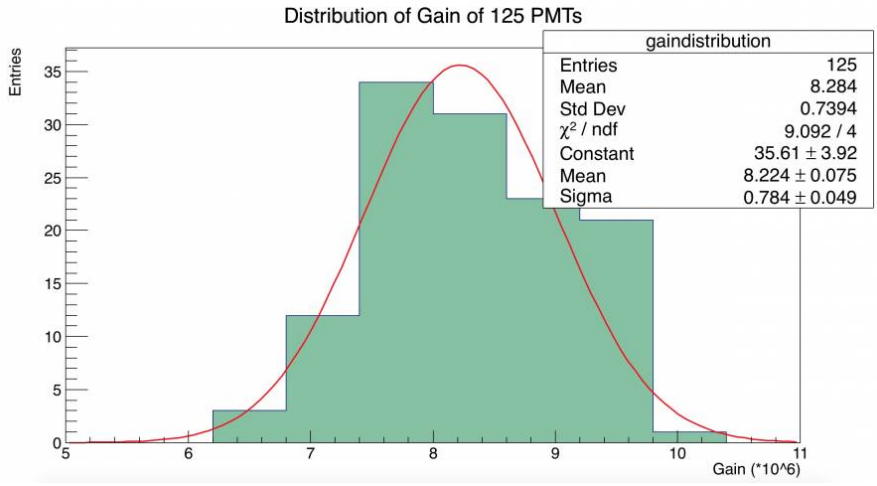

Figure 5.17: Distribution of the gain values at NHV for the 125 PMTs tested. The mean gain is $(8.22 \pm 0.07) \times 10^6$.

The calibration procedure also included the measurement of the single pe spectrum also with the optical fiber which were installed on 8 photomultipliers of each bunch. In figure 5.18 is shown as a reference the comparison between the charge spectrum obtained with the diffuser ball (blue) and the one obtained with the optical fiber (red) for the PMT 33 of bunch 3. From the comparison, the spectra are almost the same and the gain for the PMT 33 is:

- from the Optical Fiber spectrum (red): $(6.60 \pm 0.04) \times 10^6$;
- from the Diffuser Ball spectrum (blue): $(6.70 \pm 0.04) \times 10^6$;

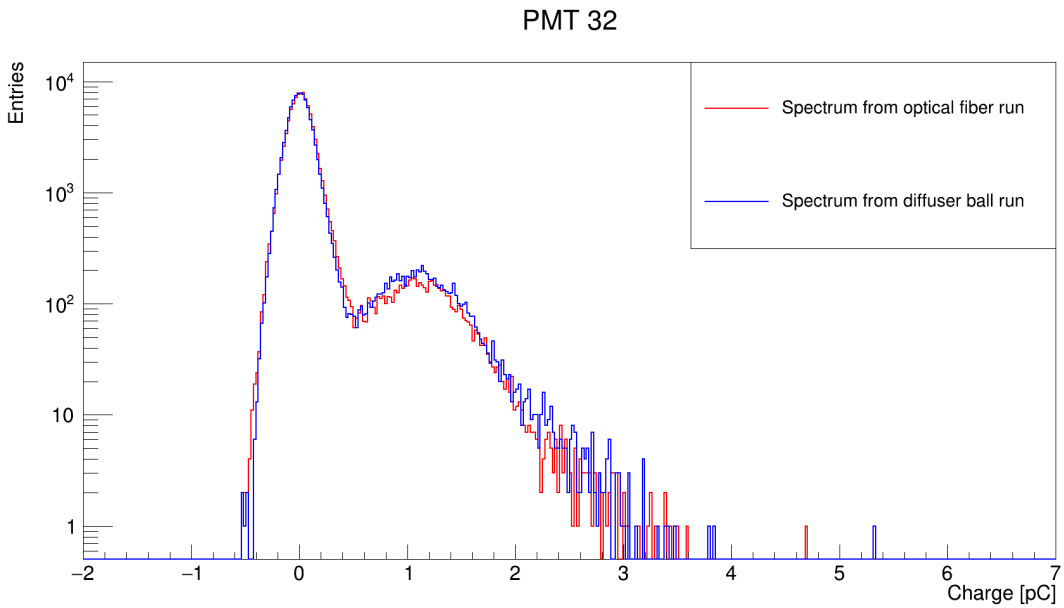

Figure 5.18: Comparison of a charge spectrum from a diffuser ball run (blue) and one from the optical fiber run (red), for PMT 32 of bunch 1 shown as a reference. There is almost the perfect overlapping between the two. The gain from the diffuser ball histogram (blue) is $(6.70\pm0.04)\times10^6$, while the value from the optical fiber histogram (red) is $(6.60\pm0.04)\times10^6$.

, which is the same within $\sim 2\%$. In each bunch, as already mentioned, only 8 PMTs were instrumented with the optical fiber. However, by checking the response of the photomultipliers closed to the PMTs involved, it was observed that they also received light (Figure 5.19). Therefore, we could deduced that the reflector spouts were acting as light diffuser.

The PMT characterization in terms of gain foresaw also the measurement with a different high voltage value, *i.e.* the voltage for which the PMTs are expected to have the same gain. In particular, we wanted to check the settings to have a gain equal to 6.24×10^6, which is the value of a single p.e. centered in 1 pC. To obtain the high voltage values that fulfill this condition, the Gain-High Voltage curves were needful.

Gain-HV curves The relationship between gain and high voltage (section 4.2) can be studied from gain measurements with different applied voltages. Thus we collected 7 points starting from the NHV and subtracting/adding 150 V, 100 V, and 50 V. The gain-hv curves for one bunch of photomultipliers are shown in figure 5.20 also in a double logarithmic scale (right); the trend is in correct agreement with the function expressed by Eq.4.7 suitably modified as follow:

$$G = KV^{\alpha} \Rightarrow \ln G = \ln K + \alpha \ln V \tag{5.8}$$

thus, the trend can be verified by a linear fit function. The resulting parameters and the relative errors are shown in the table 5.1 for 8 PMTs of bunch 6 as a reference. In that table are shown also the high voltage values in order to have a

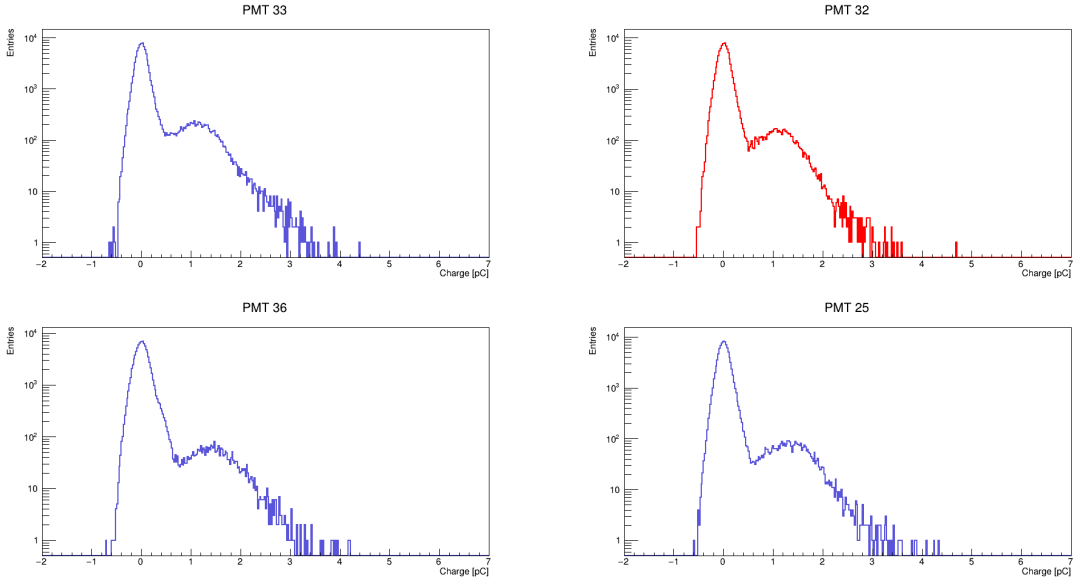

Figure 5.19: Charge spectra obtained from a spe run with the optical fiber bundle, for 4 PMTs of bunch 1 shown as a reference. Only the PMT 32 (red spectrum) is instrumented with the optical fiber. However also the other PMTs (blue spectra) positioned near the PMT 32 saw some light, as it appears from their spectra. This indicates that the reflector spout diffuses the light from the fiber in the SWT.

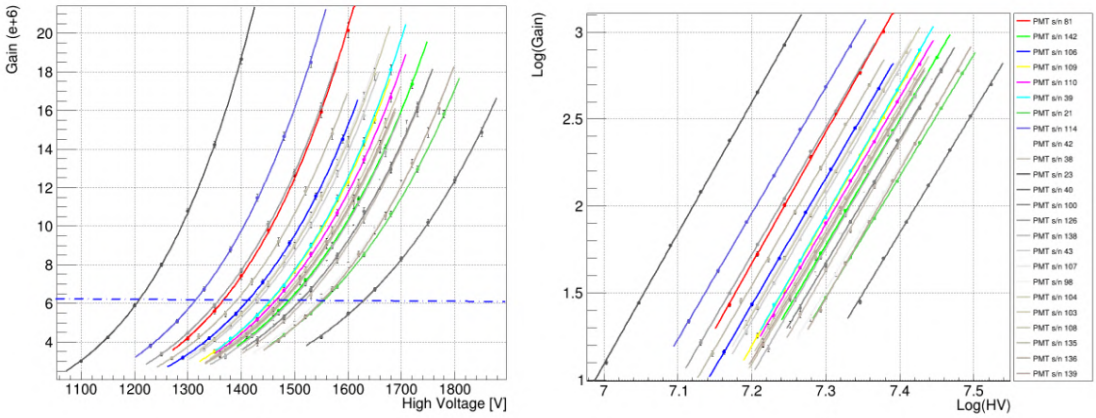

(a) (b)

Figure 5.20: Plot of the Gain-HV characteristics of 24 PMTs of the sixth bunch, shown as a reference. For each PMT we collected the 7 gain points at various HV. On the left is shown the exponential trend of the 24 PMTs, while on the right the values are reported on a double logarithmic scale, where they are fitted with a linear function (Eq. 5.8). On the left, the interception of the exponential curves with the blue dashed line (defined by $y = 6.24 \times 10^6$) gives for each PMT the corresponding "Same Gain" high voltage. The values, are calculated with Eq.(5.9) and are reported in table 5.1.

gain of 6.24×10^6. These were calculated reversing Eq.5.8:

$$\text{HV (same gain settings)} = \exp\left(\frac{\ln G - \ln K}{\alpha}\right) \tag{5.9}$$

where $\ln K$ and α are the parameters of the linear fit function.

PMT sn	$\ln K$	α	HV ($G = 6.24 \times 10^6$) [V]
81	(-52.8 ± 0.4)	(7.57 ± 0.06)	1368
142	(-50.8 ± 0.4)	(7.21 ± 0.04)	1491
106	(-50.8 ± 0.4)	(7.26 ± 0.05)	1415
109	(-52.3 ± 0.4)	(7.43 ± 0.05)	1459
110	(-51.2 ± 0.4)	(7.28 ± 0.05)	1466
39	(-52.7 ± 0.3)	(7.48 ± 0.05)	1457
21	(-49.4 ± 0.3)	(6.98 ± 0.04)	1557
114	(-50.3 ± 0.3)	(7.25 ± 0.04)	1316

Table 5.1: Parameter of the linear fit for 8 PMTs of bunch 6 shown as reference. The high voltage values that define the *same gain settings* are shown. Those values are calculated with Eq.5.9.

In general, we can say that the calibration curves allowed obtaining for each PMT the HV needed for a specific gain. This will be very useful in the installation phase of the Neutron Veto since we would like to have all the PMTs set at the same gain. This would also simplify, in the DAQ phase, for instance, the way we set the pe threshold for each of the 120 PMTs.

Once that the HV values to have this condition were extrapolated, we supplied the PMTs with these values (at least from the third bunch) and we took *Same Gain* runs in order to verify that the gains were equalized. Figure 5.21 shows some charge spectra obtained from this kind of run. One can easily see that the mean values of the gaussian fits are more or less the same. After the same gain measurements were

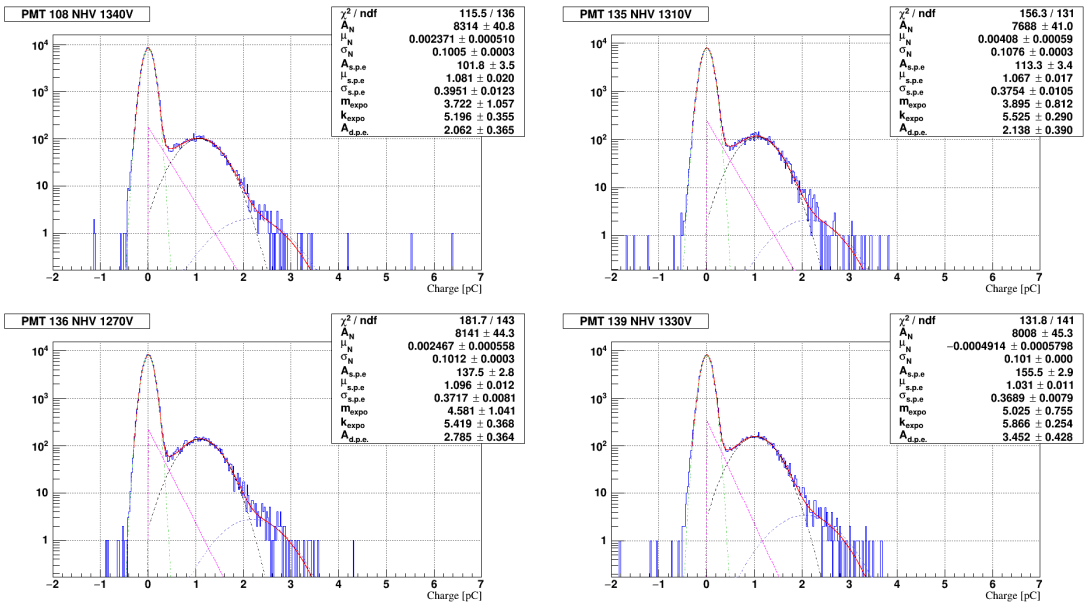

Figure 5.21: Charge spectra of four PMTs obtained from the integration of 100k events (single p.e.). On the top left of each histogram is indicated the corresponding PMT and its "Same Gain Voltage". The fit curves in red are the same as the histogram at NHV (Figure 5.12).

completed, for each bunch we checked the equalization in gain of the PMTs; this

was done considering the distribution shown in figure 5.22 of the gain for the 24 PMTs of bunch 6 as reference. As shown in figure 5.22 the PMTs were equalized

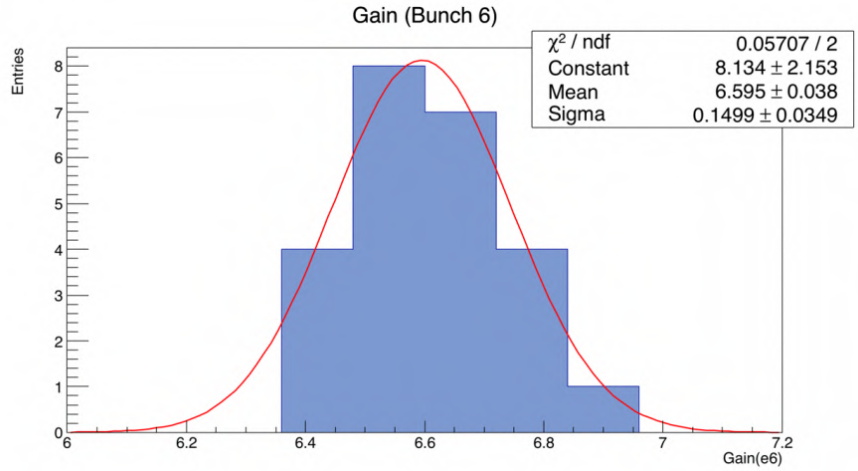

Figure 5.22: Distribution of the gain for the 24 PMTs of bunch 6, obtained with the *Same Gain* settings. The distribution is fitted with a gaussian function and from its width, we quantified the equalization of the PMTs' gain.

within $\sim 2\%$ which is a really promising result in view of the nVeto purposes.

Gain Monitoring Another important feature that the PMTs must satisfy is their performance stability. The gain stability was checked with several runs automatically acquired during the night and the weekends when a regular data taking was not necessary scheduled. Each photomultiplier was tested at least for 9 days; so for most of the PMTs we could check only the short-terms stability, as shown in figure 5.23 as a reference. It should be noted that each point of the plot in figure 5.23 actually represents the average gain value between all the gain run taken on that day (usually we had 4/5 spe runs per day).

As already mentioned, since the beginning of the test, we decided to keep two PMTs monitored for the entire period; the behavior of these PMTs gave us some information about long terms stability and about the uniformity of the setup conditions during the period of the tests. In figure 5.24 the monitoring of the PMT KQ00023 for the whole period of test is shown as a reference, with the various bunch of tests highlighted. From the third onward it is possible to note an abrupt variation of the gain; this coincides with the variation of the HV in order to have the gain of 6.24×10^6. In the plot of figure 5.24 all the variations of the setup are reported. In particular, the vertical black lines stand for the transition from one bunch to another, while the blue dashed lines represent the filling of the SWT with water. After this operation, the gain seems to not change, as expected. The red dashed lines indicate that the PMTs are set to the Same Gain voltage; this happens only from bunch 3 onward. Finally, the pink solid line in bunch 6 indicates the installation of the magnetic shield (Section 5.6) on the PMT, while the green line in bunch 3 indicates the test of the HV filter (not described in this work).

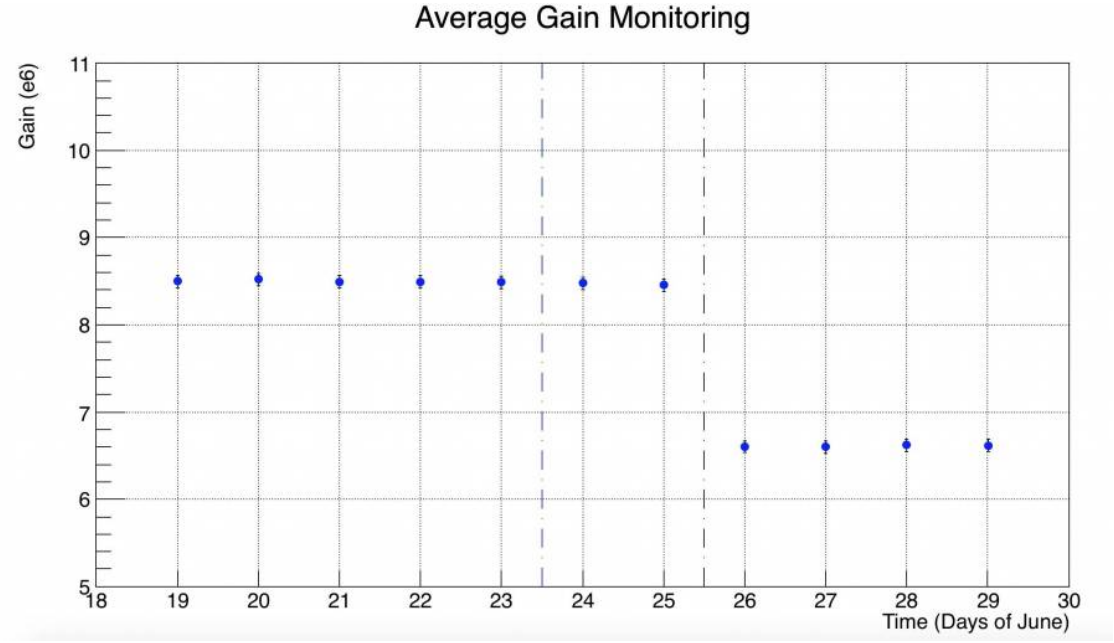

Figure 5.23: Plot of the gain monitoring of one PMT of bunch 6 shown as a reference. The two vertical dashed lines represent the filling of the SWT with water and the changing of the HV with the Same Gain settings respectively. On the x-axis are reported the acquisition day (bunch 6 was tested in the last week of June).

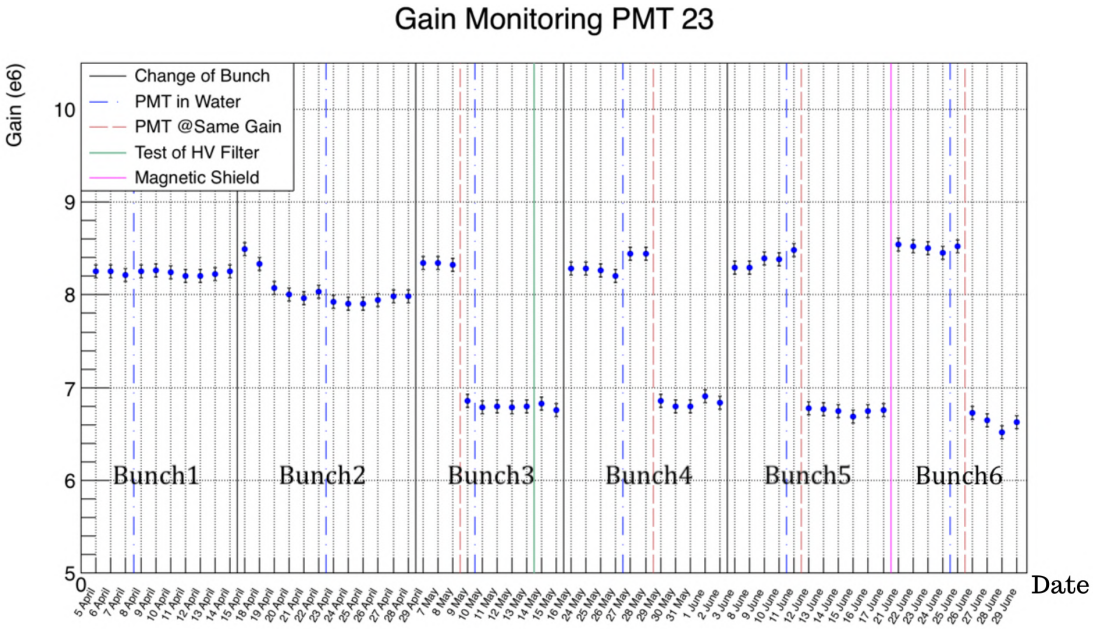

Figure 5.24: Plot of the gain monitoring of one reference PMT (KQ00023). The monitoring for the reference PMTs is done for the entire period of test and on the x-axis the acquisition day of each point is reported. All the colored vertical lines represent the variations of the setup condition (filling with water, transition between bunches, changing of the HV etc.)

5.4 Dark Rate measurements

Dark counts are the signals generated by the PMTs in the absence of light. At room temperature, the thermionic emission of electrons is the major source of dark counts. In the experiments where the expected event rate is very small, knowing the dark counts rate is important to predict the fake coincidence rate. The dark rate (DR) depends on a threshold which in turn is expressed in a fraction of photoelectrons. During the SWT test we performed measurements of the dark rate on runs without illumination and with the following characteristics:

- Acquisition Window of 10 μs;
- Trigger Rate of 0.5 kHz;
- 100k Events;
- Zero Length Encoding = $\pm$1 ADC Count.

The acquisition window was longer with respect to the one employed for the gain runs; this was decided in order to have enough statistics and thus a reasonable error from the counting ($\sim 10\%$)[2]. Another difference from the gain runs is the presence of the Zero Length Encoding suppression of all the samples of the waveforms inside the Baseline$\pm$1 ADC count threshold.

The usual way to measure the dark rate is just to count the waveform peaks over an ADC threshold and eventually with a Time-Over-Threshold (TOT). However due to a low resolution in terms of vertical axes of the waveforms (*i.e.* ADC Counts) it was decided to also exploit the charge spectra[3] rather than counting the peaks directly from the waveform. This idea is based on the fact that the dark rate pulses coming from thermionic emission are of single p.e. nature [115]. Thus the analysis procedure was divided in:

1. setting a *DAQ threshold* for the peak finding (5.25);
2. integration of the waveform peaks;
3. fit of the charge spectrum obtained with a single Gaussian function. The mean value represents the charge of 1 pe; thus the charge of its fractions are also known;
4. counting of the entries above the *software threshold* (figure 5.26); the corresponding error is the square roots of the counts.

In particular, with *DAQ threshold* we refer to the ADC Count and TOT set as shown in figure 5.25, while we call *software threshold* the one of the single pe fractions to calculate the DR (Figure 5.26). However, it should be noted that, even if both the thresholds are set via software, the first one is called in that way because it simulates the threshold that one can impose via the digitizer's firmware.

[2]estimated thanks to the fact that we already knew the order of magnitude of the DR from Hamamatsu data-sheets ($\mathcal{O}$(2 kHz)).

[3]featuring a higher resolution because of the compensation of the time resolution.

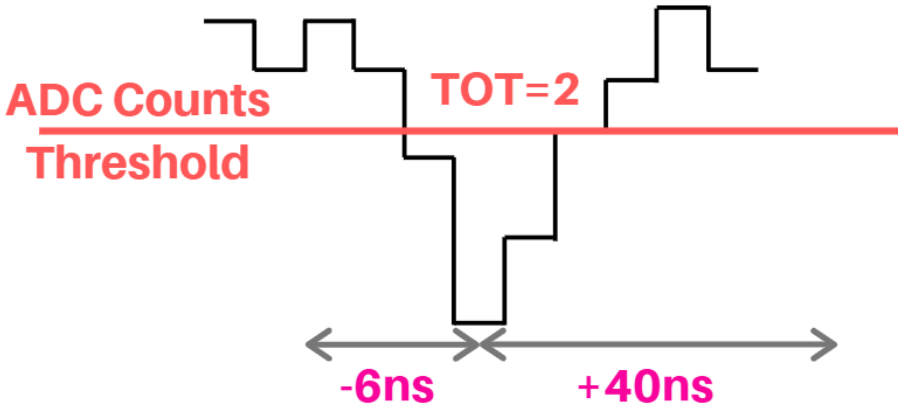

Figure 5.25: Schematic draw of the peak finding algorithm used to define a peak within the dark rate analysis. A peak is defined by giving an ADC threshold (for the analysis this was set equals to 3 ADC counts) and a TOT of 2 samples (2 ns). Once that a peak is found, the integration starts with a [-6,+40] ns window starting from the peak. This window was not chosen randomly; it resulted as the most efficient one from a dedicated study (Figure 5.15). After the finding of one peak, the algorithm skips $\sim$ 150 ns that is a time interval comparable to the coincidence window of the MV PMTs (which is 300 ns).

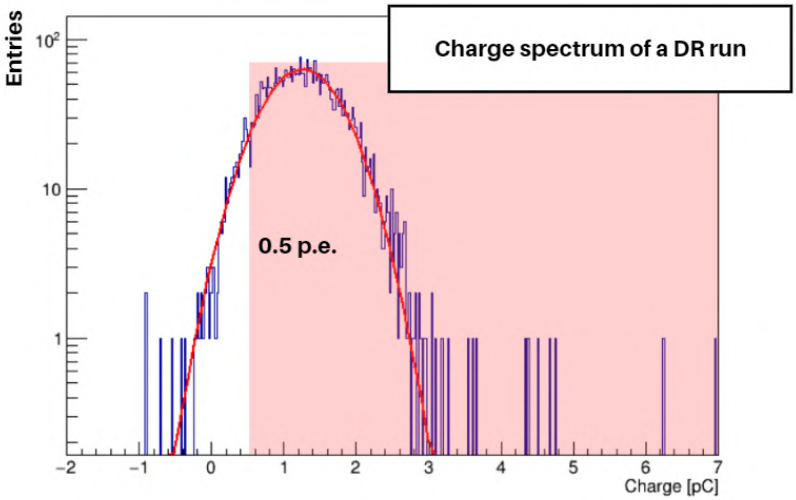

Figure 5.26: Charge spectrum of one PMT obtained by integrating the dark count peaks (as explained in figure 5.25). The thermionic emission contribution is expected to give single pe signals and this is evident from this spectrum. The absence of the pedestal is linked to the threshold of 3 ADC count which cut most of the electronic noise. From the mean of the gaussian fit of the charge spectrum, the charge values of the single pe are obtained. Thus also the 0.5 pe, shown as a reference, can be derived and the counting of the dark rate is based on the integration from [0.5 pe , $+\infty$] (red area).

The choice of the DAQ threshold of 3 ADC counts and 2 samples over threshold, was made after studying the comparison between charge spectra obtained with different thresholds in spe runs. In Figure 5.27a and figure 5.28a is shown for reference the comparison between two overlapped histograms; the black one is obtained without any threshold in the definition of the peak (thus the pedestal is

evident), while the second (red) is obtained with the thresholds. In particular, in figure 5.27a it is equal to 1 ADC counts and 3 samples over threshold, while for figure 5.28a is 3 ADC counts and 2 samples over threshold. The evaluation of the most efficient cut, in this case, is more complicated and takes into consideration different parameters and not only the efficiency curve (as the ones obtained from the study of the integration windows in figure 5.14). In particular, the comparison

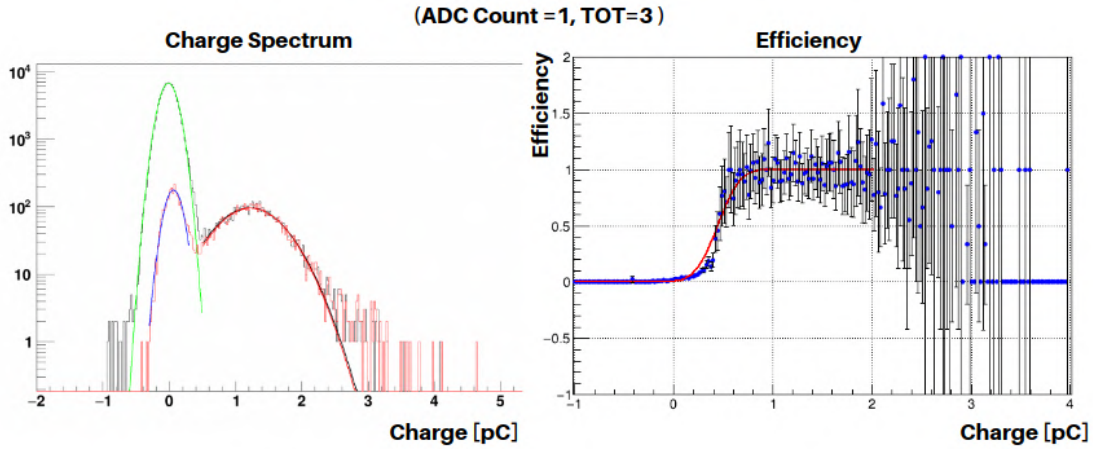

(a) (b)

Figure 5.27: (a) Comparison of the charge spectrum obtained without cut (see SWT algorithm definition in Section 5.3) (black) and the charge spectrum obtained with the threshold of ADC Counts=1 and TOT =3. Both the spectra are fitted with a double gaussian to obtain the parameters used to quantify the efficiency of the threshold. (b) Efficiency plot where each point is obtained by the ratio between the black and the red histograms in each bin. The plot is fitted with the error function of Eq. 5.4. In particular, here we were interested in the p_0 parameter which is the inflection point of the function. Anyway, the two plots are shown for a channel of an spe run as reference.

is made in terms of several quantities like:

- SPE Amplitude (amplitude of the SPE gaussian in the charge spectrum);
- Signal-to-Noise Ratio (defined as the ratio between the SPE amplitude and the pedestal amplitude);
- Ratio between the SPE amplitude of the spectrum obtained without cut and the one with cut.

Finally from the same calculation of Eq.5.3, the trend shown in figure 5.27b and 5.28b is obtained; these are fitted with the same error function of Eq.5.4. In this case, since the various cuts gave similar curves, the efficiency was estimated as:

$$\text{Efficiency} = \frac{p_0}{\mu_{SPE}} \tag{5.10}$$

where p_0 [pC] is the parameter of the error function that represents the charge of the inflection point of the curve, and μ_{spe} [pC] is the mean value of the SPE

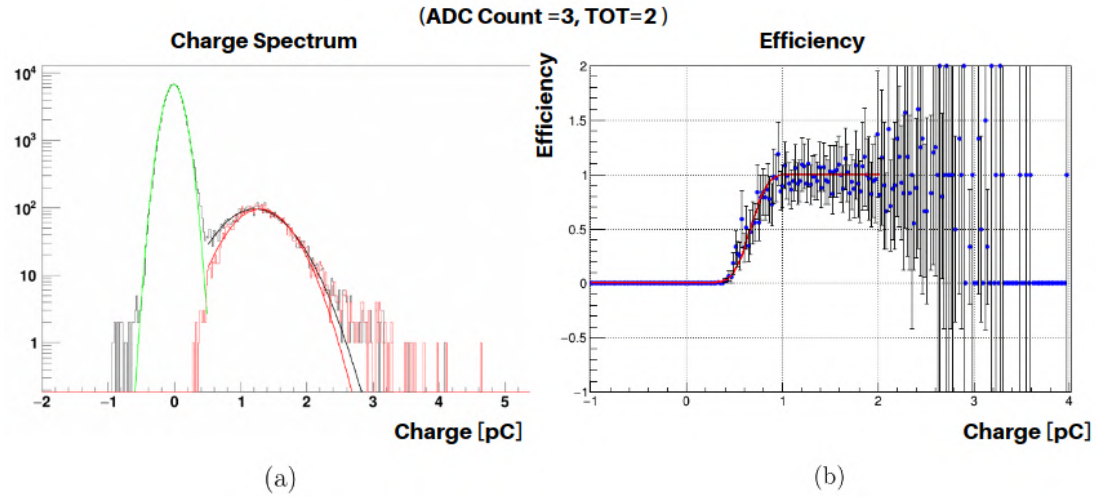

Figure 5.28: (a) Comparison of the charge spectrum obtained without cut (see SWT algorithm definition in Section 5.3) (black) and the charge spectrum obtained with the threshold of ADC Counts=3 and TOT =2. The black spectrum is fitted with a double gaussian, while the red one shows just the spe gaussian contribution: indeed with this threshold, the pedestal cut off. (b) Efficiency plot where each point is obtained by the ratio between the black and the red histograms in each bin. The plot is fitted with the error function of Eq. 5.4. The two plots are shown for a channel of an spe run as reference.

Thresholds		Area SPE		S/N		Efficiency [spe]
ADC	TOT	without cut	with cut	without cut	with cut	(p_0/μ_{spe})
1	2	95.12	93.67	0.014	0.2	0.33
1	3	”	94.19	”	0.54	0.36
2	1	”	93.17	”	0.08	0.33
2	2	”	94.73	”	∞	0.43
2	3	”	94.76	”	∞	0.47
3	1	”	95.79	”	∞	0.43
3	2	”	95.1	”	∞	0.52
3	3	”	94.8	”	∞	0.6

Table 5.2: Values of the parameters considered for the threshold efficiency study. The values of one single pe run, for one channel are shown as reference. The area of the SPE peak is evaluated considering the gaussian amplitude parameter. The ∞ values of the S/N ratio mean that it is not defined the pedestal, which is cut by the threshold. The last column is the value associated to the efficiency calculated from the error function. In particular it is expressed as [spe]. From the comparison between these values the threshold defined by ADC Counts=3 and TOT=2 resulted to be the most efficient.

gaussian. Thus, the ratio is expressed in units of photoelectrons. The values of all these quantities are shown in table 5.2 for several thresholds.

In the end, the resulting best threshold was the one with ADC Counts=3 and TOT=2, which was used as DAQ threshold for the whole DR analysis; indeed considering the threshold with ADC=3 and TOT=3, which is the characteristic

threshold of the XMASS algorithm, even if it has a high efficiency in terms of pe, the threshold tends to cut part of the signal, as shown by the value *Area SPE with cut*. For each PMT, we studied the dark rate varying the software threshold between $\{0.25, 0.5, 0.75, 1., 1.5, 2.\}$ pe. The dark rate values for each threshold for eight PMTs of bunch 5 are reported as reference in table 5.3, while in figure 5.29, the plot for the PMT 114 is shown as reference.

PMT	Dark Rate [kHz] for different thresholds [pe]					
s/n	0.25	0.5	0.75	1.	1.5	2
124	4.53± 0.07	4.29± 0.07	3.58± 0.06	2.40± 0.05	0.71± 0.03	0.35± 0.02
142	6.48± 0.08	6.10± 0.08	5.00± 0.07	3.36 ±0.06	0.86 ±0.03	0.35± 0.02
112	3.20± 0.06	3.03 ±0.06	2.54± 0.05	1.78± 0.04	0.56± 0.02	0.30± 0.02
121	2.86± 0.05	2.67± 0.05	2.21 ±0.05	1.58± 0.04	0.58± 0.02	0.34± 0.02
110	2.32± 0.05	2.13 ±0.05	1.82± 0.04	1.42± 0.04	0.58± 0.02	0.32± 0.02
113	2.39± 0.05	2.25± 0.05	1.91± 0.04	1.38 ±0.04	0.48± 0.02	0.27± 0.02
117	6.19 ±0.08	5.84 ±0.08	4.82± 0.07	3.33± 0.06	0.87± 0.03	0.36± 0.02
114	2.68± 0.05	2.50 ±0.05	2.08± 0.05	1.51± 0.04	0.52± 0.02	0.31± 0.02

Table 5.3: Dark rate value at different pe thresholds, for 8 PMTs of bunch 5, shown as reference.

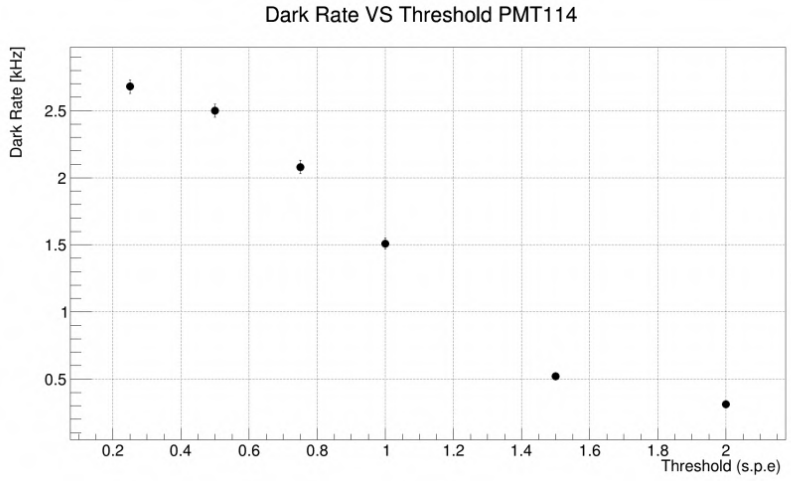

Figure 5.29: Plot of the DR [kHz] versus threshold (expressed in fraction of single p.e.) for one PMT of bunch 5, shown as reference. The points obtained range within $\{0.25, 0.5, 0.75, 1., 1.5, 2.\}$ pe. The trend is consistent with our expectations.

The MV thresholds [107] are set at the level of single p.e. but we hope to do even better in the nVeto, in order to detect lower energy events, by increasing the overall neutron veto tagging efficiency. For this reason, we have particular care for the DR values when the threshold is equal to 0.5 pe. The distribution of the dark rate values at 0.5 pe threshold, for the 125 PMTs tested are shown in figure 5.30; among them, < 5 PMTs have high DR values. We suspect that this can be due to the large electronic noise that we did not manage to reduce properly.

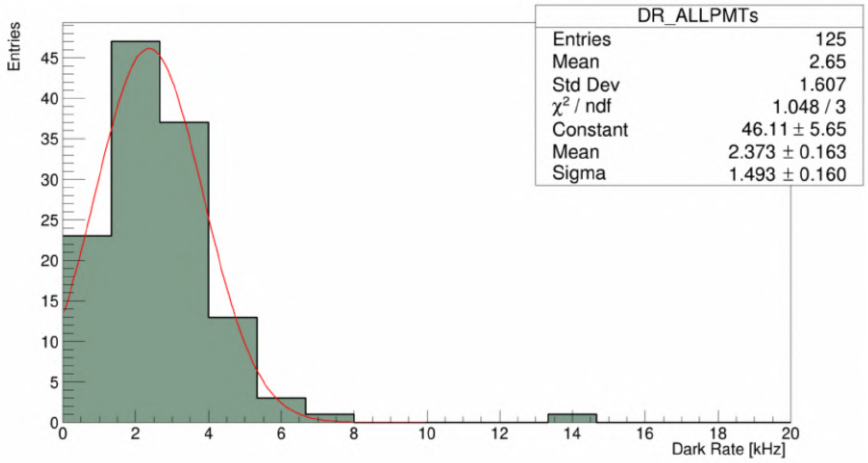

Figure 5.30: Distribution of the dark count rate values at 0.5 pe threshold for the 125 PMTs tested. The average dark rate stands at (2.37 ± 0.16) kHz. It is quite higher than the DR of the MV PMTs (which was ~ 1.6 kHz); the reason for that can be linked to the electrical noise always present in our setup. This can be also the cause of the high dark rate registered for the PMTs that stands in the distribution tail.

In particular, this can be seen considering the PMT with the Dark Rate ~ 14 kHz (which is the PMT 9); from the charge spectrum of the dark rate run (Figure 5.31) is evident the contamination of the pedestal even with the ADC threshold in the peak finding. The values obtained for the DR will give us a hint on which PMT use as spare (since we will use in the nVeto only 120 PMTs out of 125). Another analysis concerns the dark rate varying the PMT supply voltages. Figure 5.32 shows as a reference the trend for the dark rate of PMT 29 at 0.5 pe threshold. As for the gain calibration, we took dark rate runs for 7 points of High Voltage, *i.e.* starting from the NHV and subtracting/adding 150, 100 and 50. The latter analysis can be useful if one is interested in having all the PMTs of the experiment at the same dark rate value rather than at the same gain.

5.5 Timing measurements

Hits' timing information could be useful to discriminate between neutron capture signal and background in Neutron Veto. Thus, the relative timing difference among the PMTs needs to be taken into account. The availability of fast digitizers, as well as of a laser, allowed us to perform these kinds of measurement; in particular, we focused on the relative difference in Transit Time, its dependency on the HV and

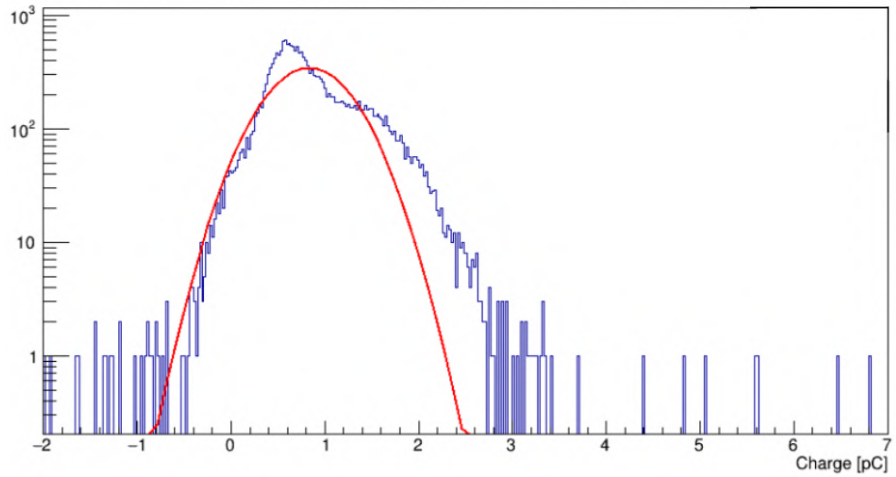

Figure 5.31: Charge spectrum obtained from a DR run of the PMT KQ0009, which shows contamination of the pedestal due to the electronic noise. Thus, the resulting DR value at 0.5 pe threshold is (13.23 ± 0.12) kHz, which is higher with respect to the other PMTs.

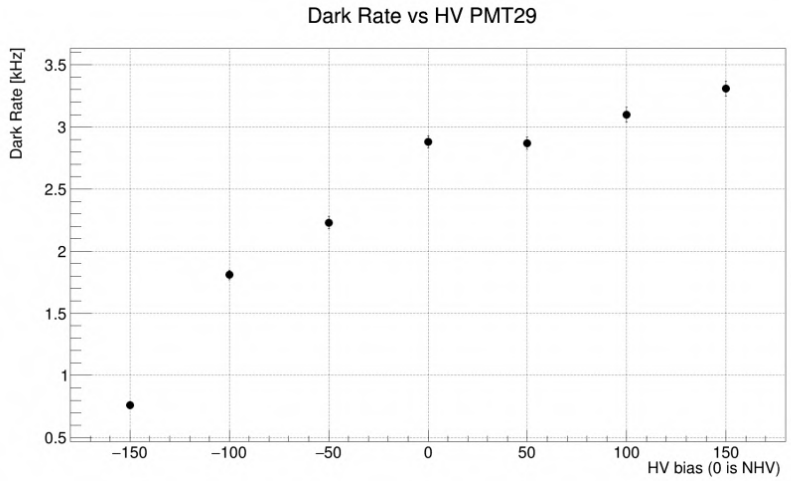

Figure 5.32: Plot of the DR [kHz] versus bias voltage (e.g NHV+bias) at 0.5 pe threshold for one PMT, shown as reference. Except for the DR at NHV the trend of the 7 points is consistent with the expectation of increasing DR with the high voltage.

the Transit Time Spread of the 125 PMTs. First of all, before making any kind of timing measurements it was necessary to correct effects like the trigger jitter between the digitizers.

Trigger Jitter The trigger signal inside the digitizer is generated synchronized to the 125 MHz internal clock. Thus, with respect to the trigger input, the response shows temporal fluctuations events by events, the so-called *jitter*; it is evident in figure 5.33 where 100 waveforms (thus 100 separate events) recorded by one digitizer are shown as a reference. Since we used several digitizers, whose trigger was transferred from one digitizer to another in daisy chain, a trigger delay between the boards was also induced. Therefore, to obtain precise timing information these

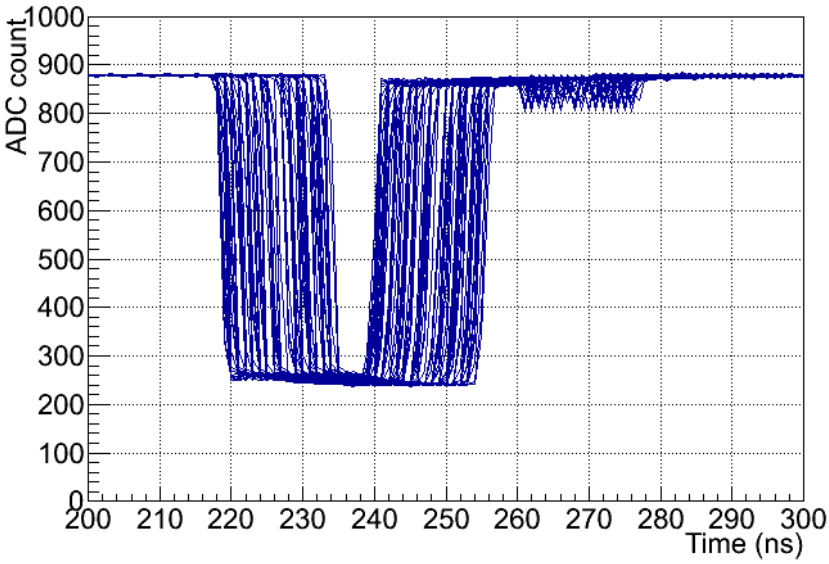

Figure 5.33: Plot of 100 trigger waveforms overlapped. The trigger signals recorded by one board have jitter event-by-event of ±8 ns, which corresponds to the internal clock frequency (125 MHz).

effects need to be corrected. Figure 5.34 shows the distributions of the trigger time for board 0-2. They were measured in dedicated runs by connecting the split trigger signal in one channel of each digitizer. From the distributions, one can easily notice the trigger delay between the boards (including also the trigger jitter of (±8 ns)). Since we took a particular care that all the PMTs had the same signal cable's

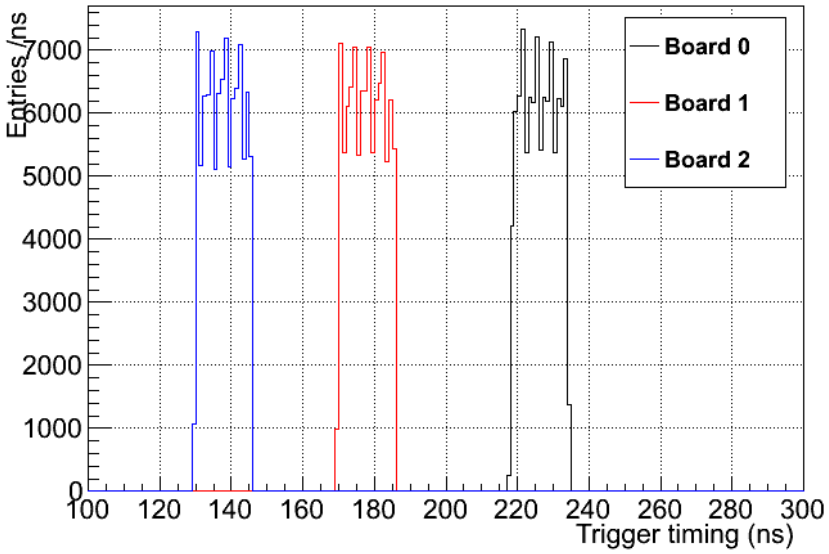

Figure 5.34: Distributions of the trigger timing for Board 0-2. The trigger signal was studied with dedicated runs where the trigger was duplicated and inserted in the boards' first channel. The width of the distributions is around 16 ns and is the so-called trigger *jitter*.

length and that we used lemo cables exactly of the same length for generating the split trigger, we derived a formula to correct the timing difference:

$$t^{'} = t - T_{trigger} + 8 \text{ ns } \times (\Delta TTT) + T_{delay} \tag{5.11}$$

where

$t^{'}$ [ns]	Time after correction
t [ns]	Time before correction
$T_{trigger}$ [ns]	Threshold crossing time
ΔTTT	Trigger Time Tag difference
T_{delay} [ns]	Trigger delay with respect to board 0 (Master)

The Trigger Time Tag difference is commonly known as the event time tag and is given by a 32-bit counter which marks the arrival time of an external trigger signal (as in our case) or the time when a signal crosses the relative threshold set. It is expressed in units of clock cycles, characterized by a duration of 8 ns corresponding to a frequency of 125 MHz. The origin of this delay is linked to the difference between the internal clock frequency and the ADC sampling frequency, which in our case was 1 GHz. Figure 5.35 is explanatory for all contributions related to synchronization when working with two boards in a situation similar to our case. Once the correction was established it was possible to proceed with the timing

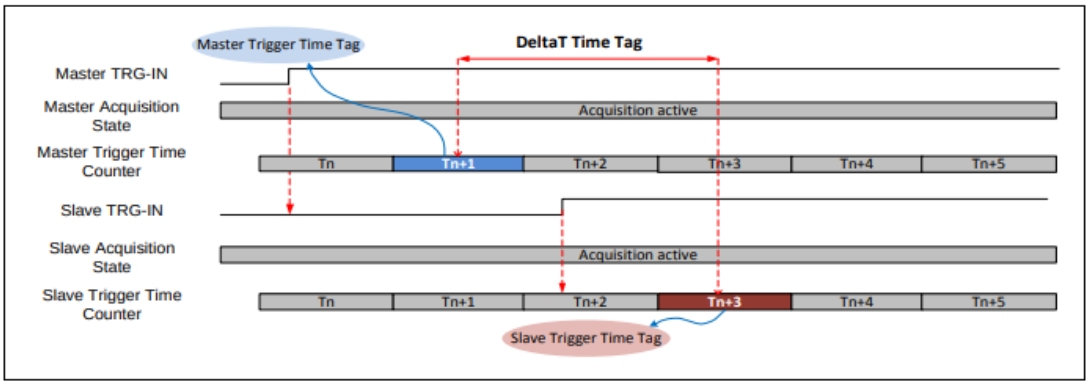

Figure 5.35: Considering the case where we want to synchronize two boards that share a trigger and a clock in daisy chain, the trigger delay, as well as the event time tag difference, are here represented. The trigger signal sent to the Master is propagated to the Slave so that the latter will receive the trigger signal with a fixed delay compared to the Master (T_{delay} in Eq.5.11). When the acquisition starts, the trigger time counters are initialized. When in the Master board the trigger signal occurs, within the 8 ns of the clock cycle T_n, the counter is not incremented until the end of the cycle, when the $T_n + 1$ period starts. The same situation happens for the slave but since the trigger signal is delayed, this occurs within the $T_n + 2$ period and registered in the $T_n + 3$. Thus the Trigger Time Tag difference is given by $(T_n + 3) - (T_n + 1) = 2$ clock count, *i.e.* 16 ns of delay.

characterization of the PMTs, which required a different setup from the original test.

Transit Time and Transit Time Spread The setup employed for the TT and the TTS measurements is shown in figure 5.36.

In particular, we had a LASER with blue light of $\lambda = 405$ nm (model EPL-405 [122]) and, since it had a fixed intensity ($> 10^6$ photons), an attenuator with several lenses was employed. Furthermore, the LASER had an internal trigger with the minimum frequency of 20 kHz; thus, in order to trigger-IN the digitizers directly, we necessarily had to use some more NIM modules. Thus to the setup described in figure 5.9 we added:

- NIM Crate with:
  - NIM-TTL adapter CAEN mod. N89;
  - Quad Discriminator Le Croy mod. 821;
  - Dual Timer CAEN mod N93B.

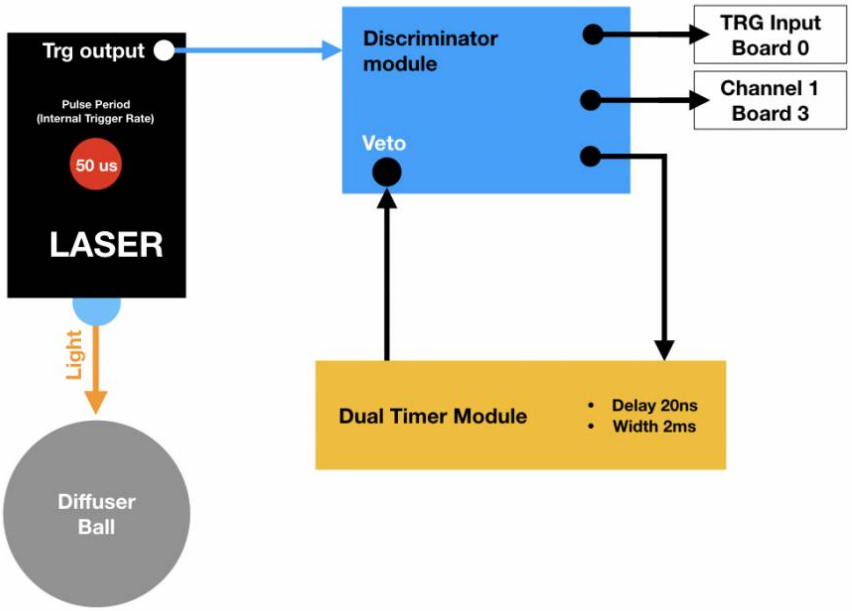

Figure 5.36: Scheme of part of the setup for the LASER measurements. The LASER, coupled with the diffuser ball, was the light source for the runs dedicated to the study of the PMT timing characteristics. The LASER provided an external trigger to be used for the acquisition of the run. The highest pulse period, i.e. the lowest trigger rate, was 50 μs. Thus in order to be compatible with the DAQ maximum frequency, the trigger signal duration had to be extended with a Discriminator NIM module + Dual Timer Module. The latter received the output of the discriminator and once delayed sent it back to the veto channel.

Once we found the correct attenuator in order to have single pe pulses, we took diffuser ball runs. In figure 5.37 we show the time position of the spe peak for all the boards before (blue line) and after (red line) the correction of Eq. 5.11; it appears very clearly the trigger delay due to the configuration of the daisy chain

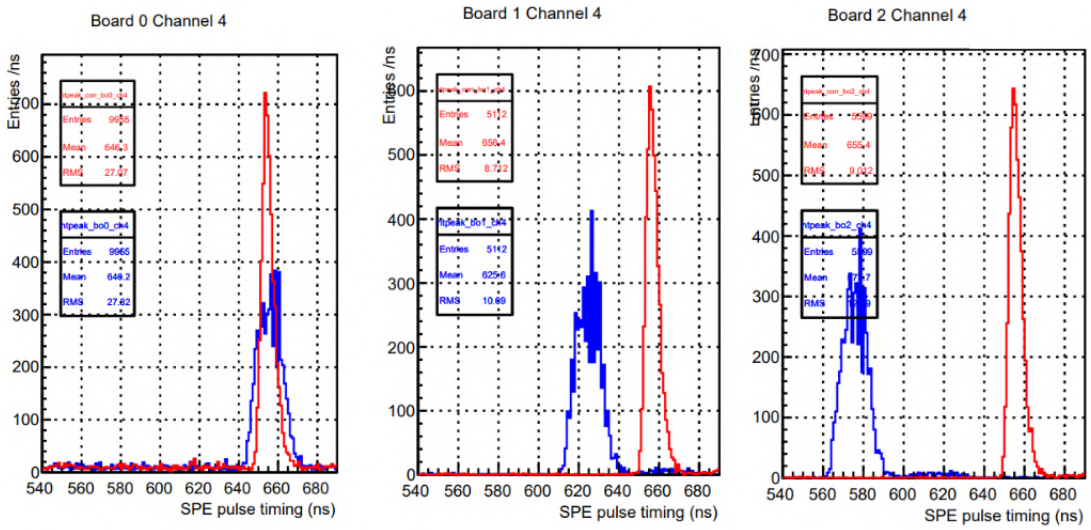

Figure 5.37: Time distributions of the single p.e. pulse before (blue) and after (red) the correction of Eq. 5.11 for the three digitizers (channel 4 shown as reference).

and also that the width of the distributions becomes sharper once we remove the systematics due to the digitizers.

The red distributions are fitted with an asymmetric[4] gaussian function with four parameters:

$$y = \begin{cases} \frac{N}{\sqrt{2\pi\sigma_+^2}} \exp\left(-\frac{(x-t_{max})^2}{2(\sigma_+)^2}\right) & (x \geq t_{max}) \\ \frac{N}{\sqrt{2\pi\sigma_-^2}} \exp\left(-\frac{(x-t_{max})^2}{2(\sigma_-)^2}\right) & (x < t_{max}) \end{cases} \tag{5.12}$$

where t_{max} is the peak timing and is linked to the TT, $\sigma_\pm$ are the standard deviation for the fall/rise side and N is the normalization constant. On the other hand, the TTS is linked to the FWHM of the distribution:

$$FWHM = \sqrt{2\ln 2} \times (\sigma_- + \sigma_+) \tag{5.13}$$

The results of the analysis for one board are shown as reference in figures 5.38-**??**, while the TT distribution of all the PMTs is shown in figure 5.39. The plot reported can be summarized as follows:

- When the PMTs are set at the same HV (see black dots in Fig. 5.38),the TT becomes the same within 1 ns;
- If the PMTs are set at the same gain (yellow dots in Fig. 5.38), the difference in TT among the PMTs becomes ∼5 ns;
- The HV dependency is similar among the PMTs (Fig. 5.40) with the TT that decreases with increasing voltage;
- The TTS for all the PMTs is <4 ns (Fig. 5.41);
- The TT for the 125 PMTs is the same within 2.7 ns (Figure 5.39).

[4]since we expect the rise and fall to be different

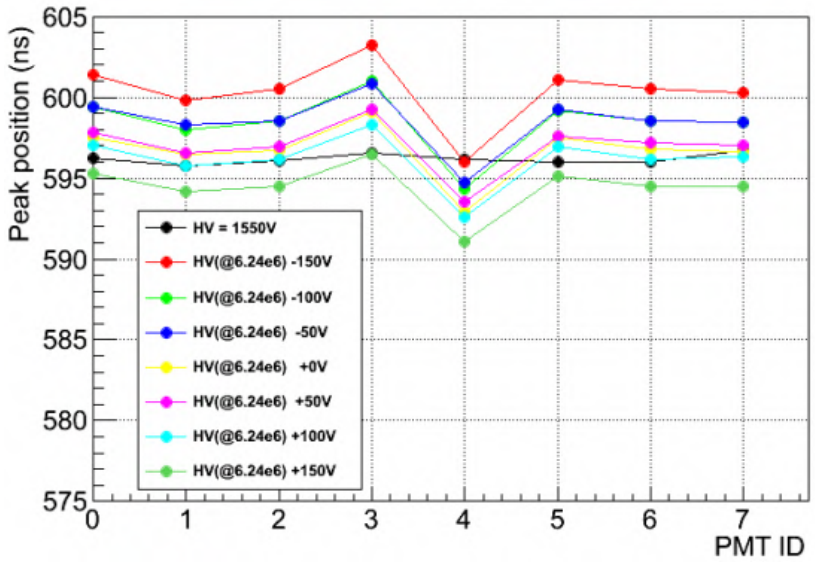

Figure 5.38: Peak timing curves for 8 PMTs of one board, shown as reference, for different HV values . When the PMTs are set at the same HV the transit time is almost the same as expected.

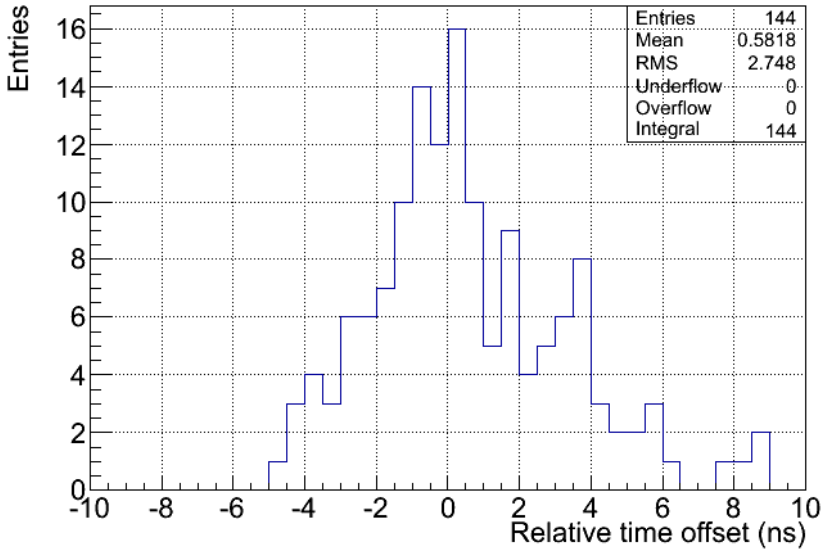

Figure 5.39: Distribution of the Transit Time of all the PMTs tested (the entries are more than 125 because are reported also the PMT retested), expressed as relative time offset with respect to the PMT KQ00043. The width of the distribution is 2.7 ns.

5.6 Magnetic field influence

Exploiting the setup available at LNGS we planned a measurement to check the Earth's magnetic field influence on the PMTs behavior and if this influence can be attenuated employing of a thin flexible sheet of high-permeability mu-metal FINEMET foil as magnetic shield. Preliminary measurements concerning

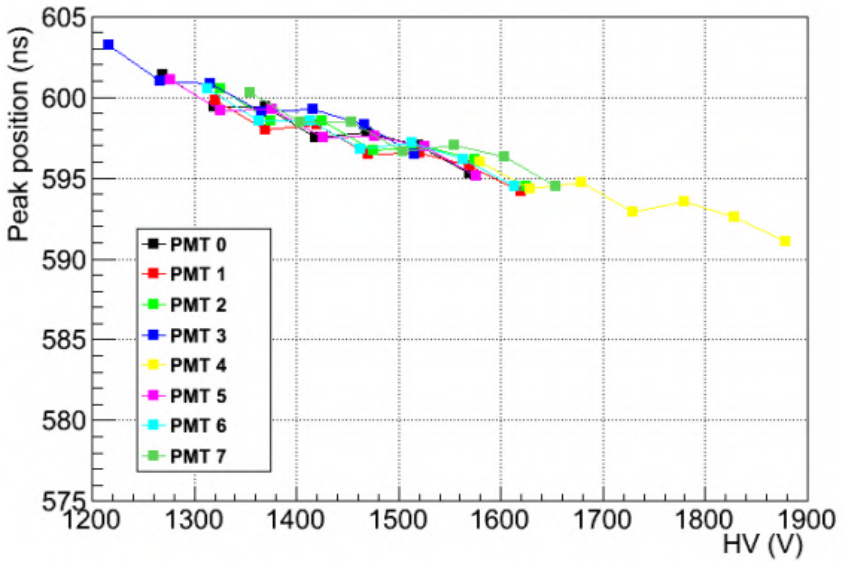

Figure 5.40: Peak timing curves as functions of the HV for 8 PMTs of one board, shown as reference (different colors). The peak timing (related to the TT) decreases with the HV as expected.

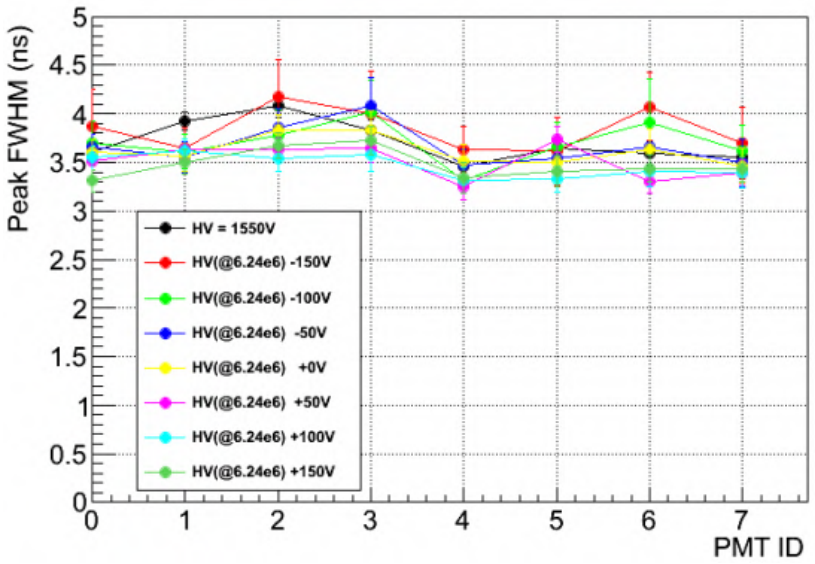

Figure 5.41: Peak FWHM for 8 PMTs of one board, shown as reference, for different HV values (different colors). The width of the distribution, i.e. the TTS, is within 4 ns for every PMT.

the application of the foil around the PMTs were performed in Bologna. The application of the foil, as well as the measurement itself, follows a similar procedure as the one used in the Daya-Bay experiment [117]. The PMT's parameters that can be monitored in order to see such effects are the ones obtained by the single p.e.

spectrum, *i.e.* the gain, the peak-to-valley ratio and the "area ratio", defined as:

$$\text{Area Ratio} = \frac{\text{Area SPE Gaussian}}{\text{Area of the entire spectrum}} \tag{5.14}$$

where "Area SPE Gaussian" refers to the area under the guassian fit (thus the amplitude) of the SPE peak in the charge spectrum. The area ratio indicates the number of triggers that generated a PMT signal and is strictly connected to the PMT's *collection efficiency*.

5.6.1 Preliminary tests in Bologna

The aim of the preliminary test performed in the INFN Bologna laboratory was to check any changes in the performance of the PMT varying its orientation according to the cardinal directions. In addition, we cross-checked, after the installation of the mu-metal foil, the attenuation of the influence of the Earth's magnetic field. The experimental setup in Bologna consisted of:

- one PMT Hamamatsu R5912 (nVeto model);
- optical fiber coupled to polyethylene reflector spout;
- 1 VME bridge CAEN V1718;
- NIM-TTL adapter CAEN model N89;
- 1 digitizer V1724 (14 bit, 100 MS/s ADC, 8 channels 2.25 V_{pp} input range);
- Dual Timer NIM N93B (used as trigger EXT for LED);
- LED driver CAEN model SP5601;
- Power Supply CAEN 1470;
- Black Box (Fig. 5.42) with the PMT inside;
- FINEMENT, magnetic shield (Fig. 5.43).

In order to have quick feedback on the magnetic field effect in this test, we monitored just the gain. Varying the direction of the PMT polar axis (Fig. 4.7) with the PMT in horizontal position we calculated the gain variation considering the North direction as reference, via:

$$\text{Gain Difference}[\%] = \frac{\text{Gain} - \text{Gain at North}}{\text{Gain at North}} \tag{5.15}$$

The results for the PMT "naked" are shown in figure 5.44 with the black dots. Then we took several spe runs in case of two different shapes for the magnetic shield as shown in figure 5.45 and 5.46 on the right, while on the left, the corresponding results of the the gain monitoring are shown.

The mean gain for the two configurations is the same within the error; this is consistent with the expectation that *the influence of external magnetic fields*

Figure 5.42: Photo of the light-tight Black Box containing the PMT for the magnetic field influence test. The setup is located in the INFN Bologna laboratories.

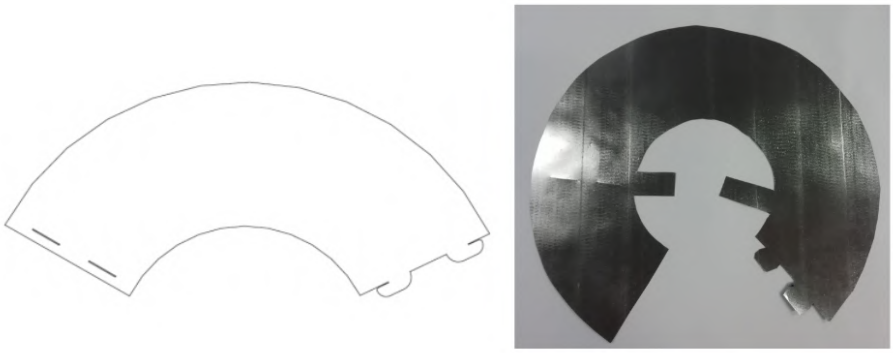

(a) (b)

Figure 5.43: (a) Drawing of the shape that we used for the magnetic shield installation on the PMTs [117]. (b) Picture of the magnetic shield with the tabs towards the center to hold it still with the PMT holder.

involves mainly the electron focusing region. The configuration (b), shown also in figure 5.47 was adopted for the subsequent tests, resulting also more practical to install considering the interference with the PMT holder in the configuration (a). Therefore, the gain difference was measured also for the shielded PMT; the results are shown in figure 5.44 with the blue triangles. In table 5.4 are reported the values of the gain when the PMT is with or without shield for each direction; the difference between the two cases is also reported for completeness.

From the comparison in figure 5.44 one can conclude that the gain variation due to the PMT orientation is reduced after the application of the foil, while, considering only one direction, *e.g.* the South, the mean gain stands at $(7.88 \pm 0.13) \times 10^6$ without the FINEMENT, while with the shield it increases up to $(8.47 \pm 0.11) \times 10^6$. It should be mentioned that with the PMT covered only up to the first dynode of the amplification chain, we tried different configurations with different radius. In the end the one already represented in figure 5.43 (with minor radius $r = 62$ mm and

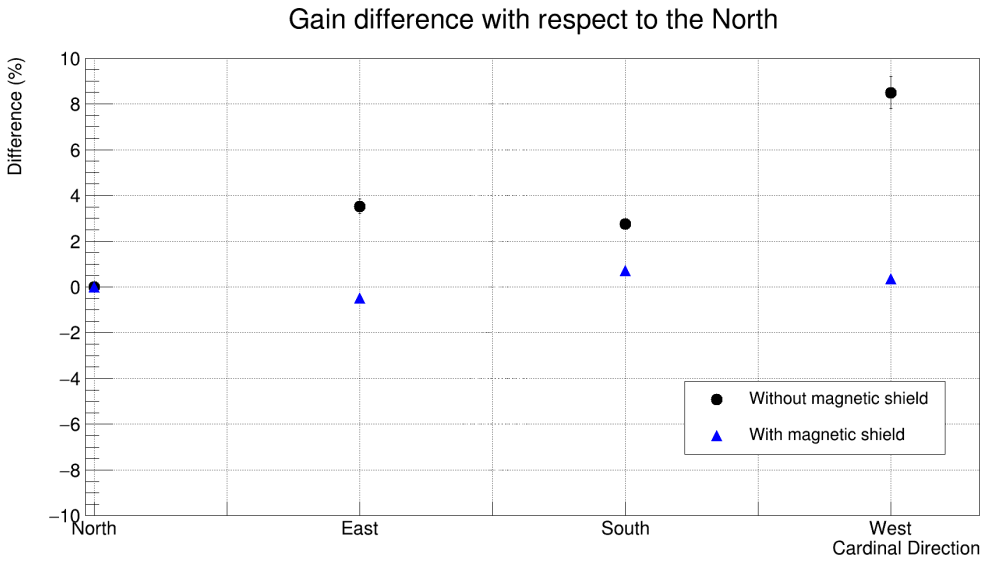

Figure 5.44: Plot of the PMT relative gain difference (Eq. 5.15) with respect to the PMT in North position, without (black dots) and with (blue triangles) the magnetic shield installed. This plot summarizes the influence of the magnetic field on the PMT gain. With respect to the variations registered without the shield the influence of the magnetic field is mitigated.

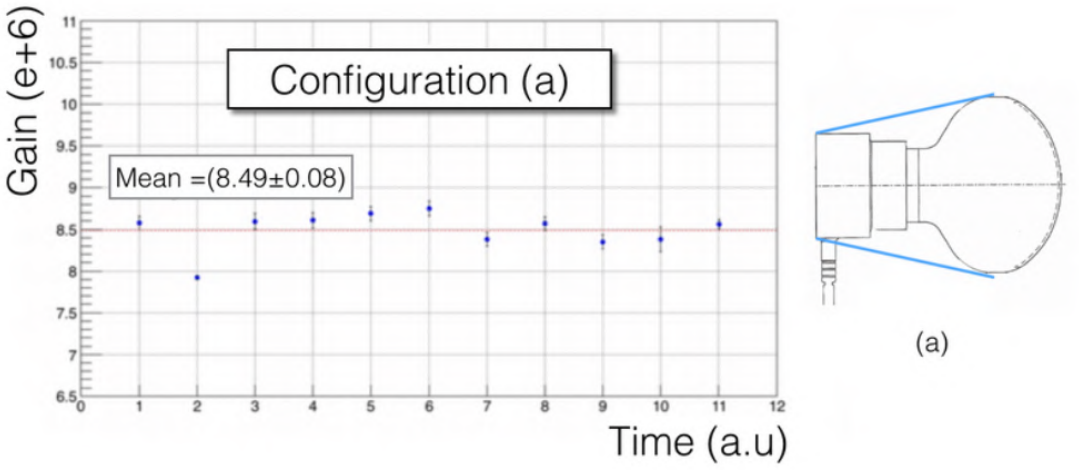

Figure 5.45: Gain monitoring plot with the magnetic shield installed as the configuration (a) (right). The mean gain stands at $(8.49 \pm 0.08) \times 10^6$

greater radius $R = 172$ mm) showed the best improvement of PMT performances.

In the end, the results obtained in the Bologna test although interesting were not enough to claim an improvement in the PMTs' performance with the FINEMENT foil, also due to the limitations imposed by the experimental setup. Thus, further measurements were planned at the LNGS using the SWT setup.

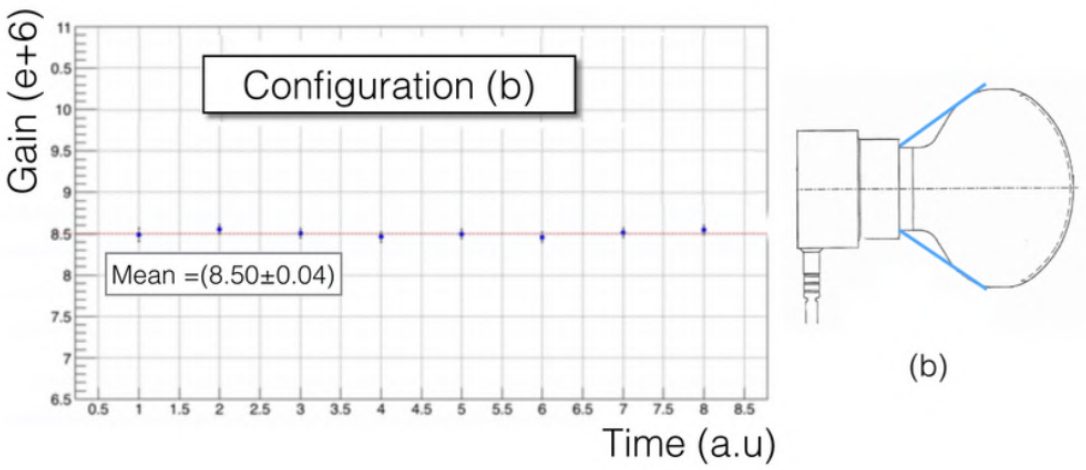

Figure 5.46: Gain monitoring plot with the magnetic shield installed as the configuration (b) (right). The mean gain stands at $(8.50 \pm 0.04) \times 10^6$

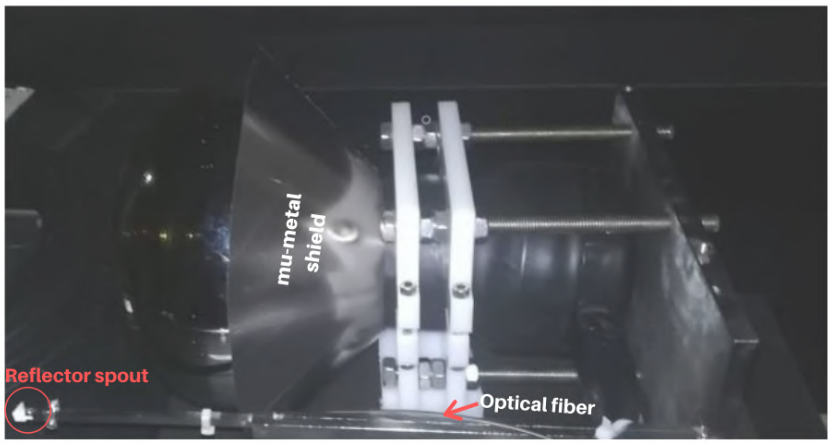

Figure 5.47: Picture of the PMT in the horizontal position inside the black box (of figure 5.42) with the magnetic shield installed as the configuration (b) (Figure 5.46). The calibration was made with the optical fiber focused on the reflector spout (highlighted in figure). The PMT was mounted on a holder different from the nVeto ones; indeed we reused a holder from the Muon Veto PMT tests [107].

Orientation	Gain ($\times 10^6$) without shield	Gain ($\times 10^6$) with shield	Difference (%)
North	7.89 ± 0.12	8.64 ± 0.09	8.6 ± 0.3
East	7.99 ± 0.14	8.74 ± 0.08	8.6 ± 0.3
South	7.88 ± 0.13	8.47 ± 0.11	6.9 ± 0.3
West	8.22 ± 0.09	8.70 ± 0.09	5.70 ± 0.17

Table 5.4: Gain values for each orientation without and with the magnetic shield foil installed. The difference (%) is also reported.

5.6.2 Measurements at LNGS

Recalling the SWT setup, we had 24 PMTs arranged in a structure with two rings. Only 4 of them in the top ring were chosen for the application of the foil;

the PMTs chosen were the ones pointing the four cardinal directions defined with the help of a compass (Fig. 5.48). All the PMTs were oriented in the horizontal position.

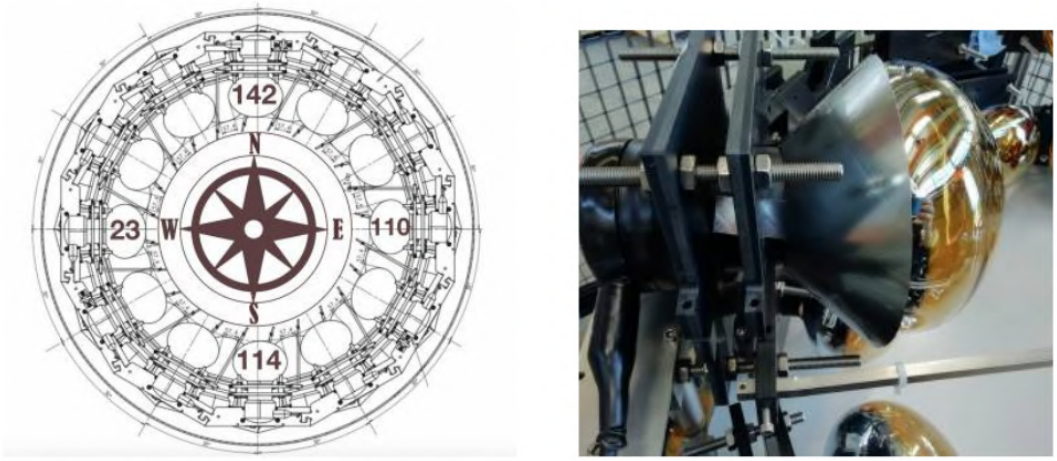

(a) (b)

Figure 5.48: (a) Schematic of the PMT location inside the SWT. The s/n of the PMT tested with the magnetic shield is reported and their orientation is indicated with the compass. (b) Photo of one PMT mounted on the support structure with the magnetic shield installed.

In particular, we exploited the fact that in bunch 6 we had 11 free places on the support structure to retest some photomultipliers. Thus in bunch 5, we tested the PMTs oriented as shown in figure 5.48a without shield and then we performed the measurements by installing the shield (as shown in figure 5.48b) in bunch 6. The four PMTs tested had similar High Voltage values but different gain. Thus, only when they were set in the "same gain" condition they could be considered as the same PMT oriented towards the 4 cardinal points. Thus we set:

- Nominal High Voltages to check the spe parameters variation without/with the FINEMENT foil;
  - in this case we are checking the influence of the magnetic shield on four different PMTs in different cardinal directions;
- Same Gain Voltages to check the magnetic field influence without/with the FINEMENT foil;
  - in this case the four PMTs are considered as the same PMT in terms of gain, and we can compare the different cardinal position between each other.

Carrying out diffuser ball runs we were able to verify the PMT performances by monitoring the gain, the peak to valley ratio (P/V) and the area ratio for each PMT at NHV. As shown in figure 5.49 and 5.50 the gain and the peak to valley tend to increase after the installation of the foil (as shown in figure 5.48b).

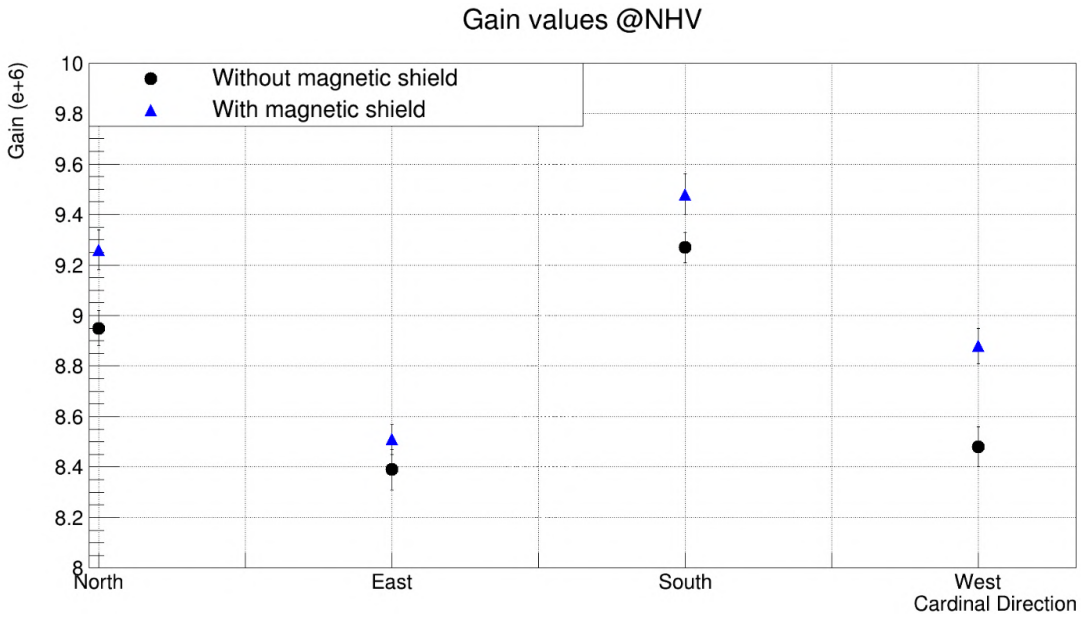

Figure 5.49: Plot of the gain (at NHV) in each cardinal point without (black dots) and with (blue triangles) the magnetic shield. For every orientation a slight increase of the gain is observed.

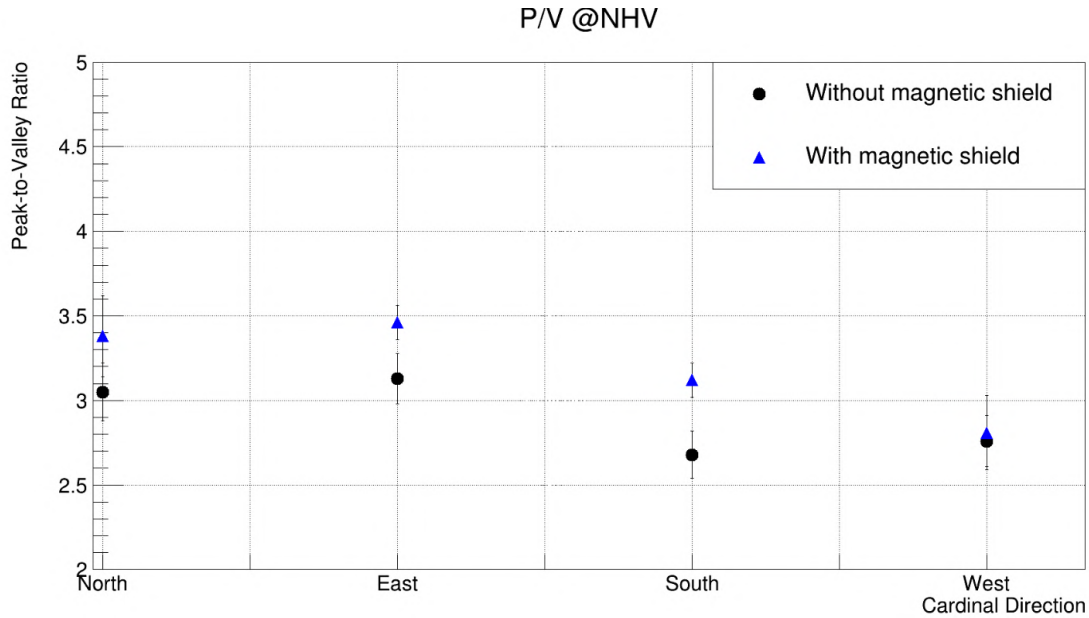

Figure 5.50: Plot of the peak to valley ratio (at NHV) in each cardinal point without (black dots) and with (blue triangles) the magnetic shield. An increase of the p/v is observed.

To give an idea of the gain variation, the values for the three parameters monitored are reported in tables 5.5,5.6 and 5.7.

On the other hand, the amplitude ratio behaves ambiguously being lower with the magnetic shield installed. The reason is not yet completely understood also because the area ratio strongly depends on the electronic noise and on the setup, *e.g.* if the position of the diffuser ball is not the same (or perfectly centered) in the

Gain			
Orientation (PMT s/n)	Without shield	With shield	Difference (%)
North (114)	8.95 ± 0.07	9.26 ± 0.08	3.48 ± 0.03
East (23)	8.39 ± 0.08	8.51 ± 0.06	1.43 ± 0.01
South (142)	9.27 ± 0.06	9.48 ± 0.08	2.31 ± 0.01
West (110)	8.48 ± 0.08	8.88 ± 0.07	4.70 ± 0.04

Table 5.5: Gain values for the PMTs tested (at nominal high voltage) without and with the magnetic shield. The difference (%) is also reported.

Peak-to-Valley			
Orientation (PMT s/n)	Without shield	With shield	Difference (%)
North (114)	3.05 ± 0.17	3.38 ± 0.36	10.8 ± 2.3
East (23)	3.13 ± 0.25	3.46 ± 0.28	10.6 ± 2.5
South (142)	2.68 ± 0.21	3.12 ± 0.35	16.2 ± 4.3
West (110)	2.76 ± 0.16	2.81 ± 0.16	1.9 ± 0.3

Table 5.6: P-to-V values for the PMTs tested (at nominal high voltage) without and with the magnetic shield. The difference (%) is also reported.

Area Ratio			
Orientation (PMT s/n)	Without shield (e-2)	With shield (e-2)	Difference (%)
North (114)	3.5 ± 0.1	3.1 ± 0.1	-11.8 ± 0.3
East (23)	3.8 ± 0.1	3.8 ± 0.1	0
South (142)	5.8 ± 0.1	5.1 ± 0.1	-12.0 $\pm$ 0.2
West (110)	5.0 ± 0.1	4.4 ± 0.1	-12.0 ± 0.2

Table 5.7: Area Ratio (or Amplitude Ratio) values for the PMTs tested (at nominal high voltage) without and with the magnetic shield. The difference (%) is also reported.

two bunches considered.

Regarding the Same Gain conditions, figures 5.51, 5.52 and 5.53 show the variations of the parameters with respect to the North direction (obtained with a formula similar to Eq.(5.15)).

In both cases, the application of the magnetic foil seems to mitigate the magnetic influence which is broad for the area ratio parameter ($\lesssim 60\%$). In the end, it is difficult to draw conclusions about the effectiveness of the configuration with the magnetic sheet. Anyway since the effect of the magnetic shield does not appear significant, and given the fact that the installation in the nVeto system would not be easy due to the interference with the PMT holders, we have decided to not use the foil.

5.7 Final remarks on the Neutron Veto photomultipliers test and calibration

120 photomultipliers Hamamatsu R5912 will be installed in the Neutron Veto of the XENONnT experiment. These are photomultipliers that have been purchased

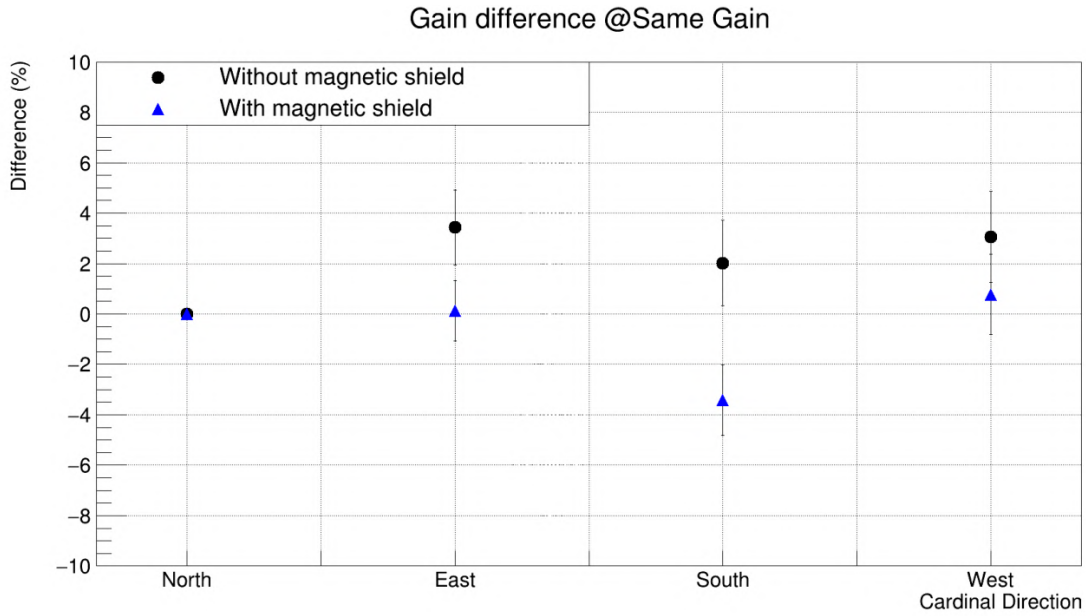

Figure 5.51: Plot of the gain differences in each cardinal point with respect to the North, without (black dots) and with (blue triangles) the magnetic shield. The PMTs were set at the same gain, and without the magnetic shield the equalization is achieved within $\lesssim 4\%$. With the magnetic shield (except for the South direction) the equalization is within $\lesssim 2\%$. Furthermore, the behavior found in the Bologna test (Figure 5.44) is partially confirmed in this plot.

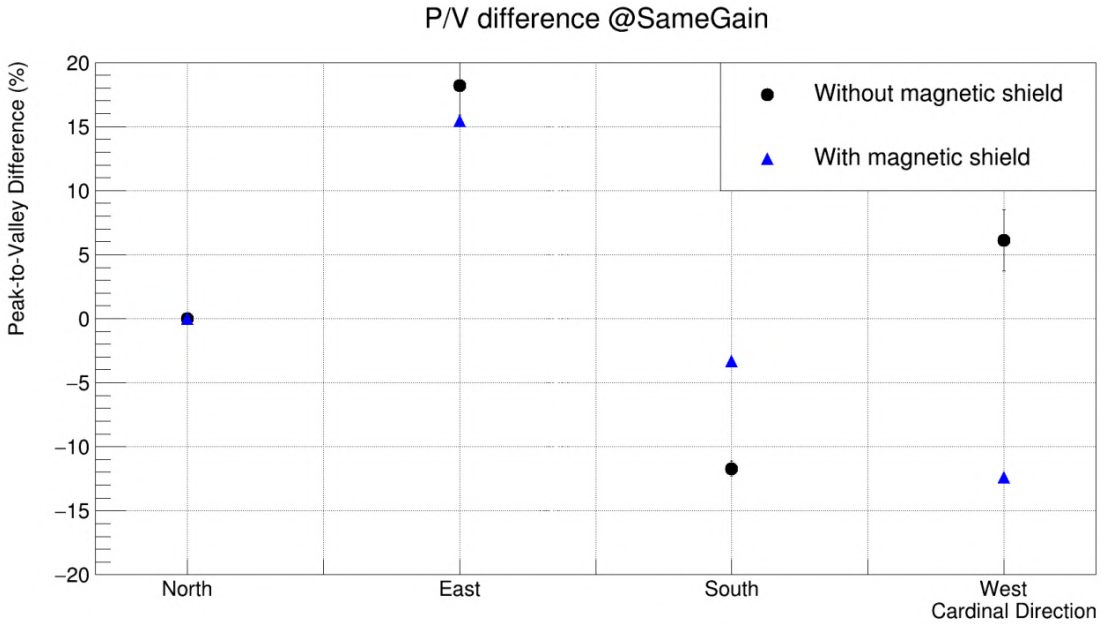

Figure 5.52: Plot of the peak to valley differences in each cardinal point with respect to the North, without (black dots) and with (blue triangles) the magnetic shield. Again, except for the West direction, slight mitigation of the magnetic field influence on the p/v is observed. The ambiguous behavior of the PMT pointing the West direction is not yet completely understood.

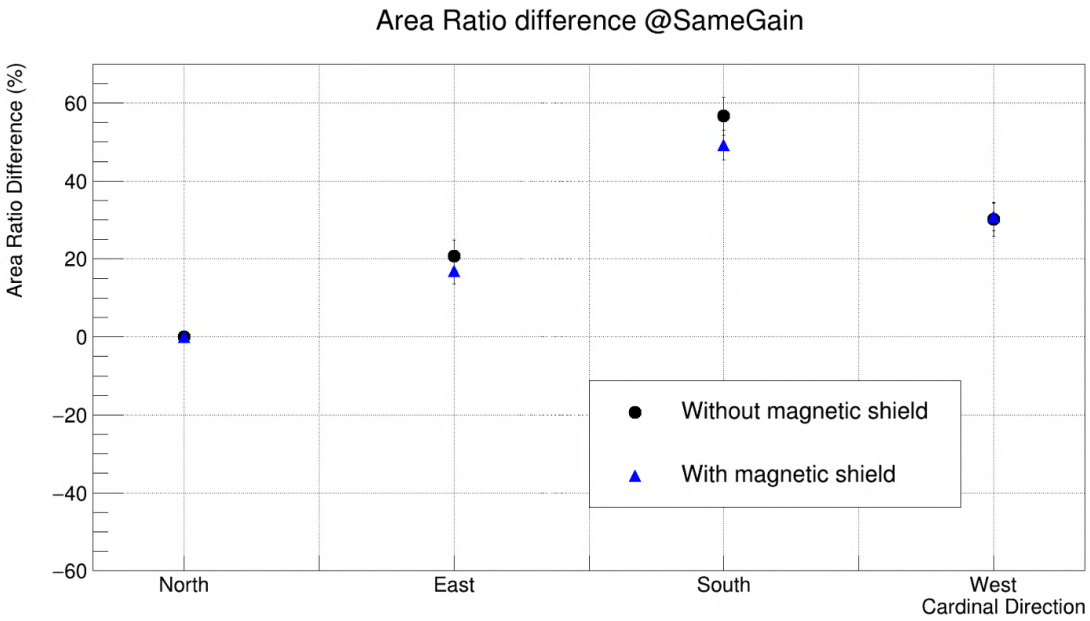

Figure 5.53: Plot of the area ratio differences in each cardinal point with respect to the North, without (black dots) and with (blue triangles) the magnetic shield. Again, except for the West direction, a slight mitigation of the magnetic field influence on the area ratio is observed. The ambiguous behaviour of the PMT pointing the West direction is not yet completely understood.

with specific requests for high quantum efficiency, low dark rate, and low radioactivity. In view of the future installation, 125 PMTs have been tested both in air and in water in the Small Water Tank apparatus. The purpose of the test was not only to verify their functioning but also to have a full calibration data-set to be used as reference in the XENONnT experiment.

Several kinds of measurements were made by taking advantage of the availability of an efficient and optimized setup. The installation and calibration procedures were organized along the lines of those tests. The characterization of the photomultipliers was carried out by monitoring the gain, the dark rate and the transit time. In addition, the afterpulses have been monitored, although they have not been described in this chapter since the analysis is still ongoing. We were also able to plan some non-trivial measures *i.e.* the influence of the Earth's magnetic field and the use of the magnetic shield to enhance the PMTs' performance. The calibration data-taking ended on June, 30th 2019, the day on which the electronics and photomultipliers were turned off. Anyway, some analysis, such as the afterpulses, are still going on. The main results obtained from the tests have already been discussed inside the Collaboration and it has been agreed that all photomultipliers exhibit behavior consistent with the Hamamatsu data-sheets. The PMTs tested were 125 (5 spares). The main results of the tests can be summarized as follows:

- the average gain of the 125 PMTs stands at $(8.22 \pm 0.07) \times 10^6$ at Nominal High Voltage (Figure 5.17);

- the average dark rate at 0.5 pe threshold is (2.37 ± 0.16) kHz (Figure 5.30);

- the transit time is the same for all photomultipliers within 2.7 ns (Figure 5.39);
- the transit time spread for all the photomultipliers is $\lesssim$ 4.5 ns (Figure 5.41).

With these characteristics we can request a 10-fold coincidence of the PMTs keeping the fake coincidences rate very low (see section 4.2.2). In addition, the fast response of the PMTs will give us the timing information of the neutron capture events; that is an important feature allowing to establish a time correlation with the TPC events. Finally, one can conclude that the PMTs chosen and calibrated will provide the performances to ensure the NR background reduction as needed.

Conclusions

Shedding light on the mystery of the Dark Matter (DM) is one of the primary goals of research in cosmology and astroparticle physics. DM is required to explain a wide variety of both cosmological and astrophysical observations, such as the anomalies of Cosmic Microwave Background (CMB) and the growth of Large Scale Structure (LSS), galaxy rotation curves and the lensing of galaxies and clusters. However, despite the relentless theoretical and observational efforts, the nature of this form of matter remains still unknown. There is a great variety of DM candidates, many with electromagnetic signatures and coupling to Standard Model (SM) particles via decay, annihilation, and scattering. All these candidates must be identified within theoretical frameworks beyond the SM. The main experimental efforts are focused on the detection of the Weakly Interacting Massive Particle (WIMP), a class of particles considered to be the most promising candidates of dark matter. Despite all constraints coming from the cosmological and astrophysical observations, there remains a large portion of viable parameter space for DM particles. This makes the dark matter one of the most studied topics in both the theoretical and experimental physics fields. Among the experiments, the most motivating results are obtained from the ones that employ direct detection techniques, based on the research of scattering of WIMPs off target nuclei. Given the low number of expected events, these experiments are characterized by large ultra-pure detectors, which are shielded from radioactivity and cosmic rays. With the aim of *enlightening the dark*, in 2007, the XENON project was born. Its detector consists of a dual-phase Time Projection Chamber filled with xenon. The XENON1T experiment, operational from 2016 to 2019, provided the world-wide best exclusion limits regarding the SI and SD WIMP-nuclei interaction cross-section, being the first tonne-scale and most sensitive DM detector in the world to date. Indeed, after 1 t $\times$ year of exposure, XENON1T reached the ER background equal to $83^{+5}_{-3}(sys) \pm 3(stat)$ evt/t$\times$yr$\times$keV$_{ee}$, which is the lowest ever achieved in a DM search experiment. Those results allowed us to set an upper limit for WIMP masses above 6 GeV/c^2, with a minimum at 4.1×10^{-47} cm^2 for a mass of 30 GeV/c^2 [1]. Most of the XENON1T subsystems were designed in order to accommodate for fast construction of the upgrade XENONnT. The XENONnT detector will host about 8 t of xenon, 6 t of which will be employed as active target. However, the scientific goal of increasing the sensitivity by about one order of magnitude will be achieved both thanks to the increase in target mass, and to a further reduction of the background. Thus, since the dominant source of background will be due to the radiogenic neutrons from detector materials, a neutron tagging detector, with a tagging efficiency above 85%, has been designed. That is the Neutron Veto

(nVeto) detector, which will be integrated with the already present subsystems and will be located around the cryostat, inside the water tank. The detection of the photons emitted by the neutron capture process is achieved by means of 120 Photomultiplier Tubes (PMT) 8" Hamamatsu R5912, featuring a high QE and a low amount of intrinsic radioactivity, installed on the walls of the nVeto. The design of the nVeto support structure, as well as of the reflective walls, is one of the subjects of this thesis and is now completed; the final drawings show a non-regular octagonal structure whose walls are made up of expanded-PTFE reflective panels. Moreover, all the nVeto detector materials have been properly selected in order to have a very low intrinsic radioactivity, and not to be deteriorated in a Gd-water solution. They mainly consist of stainless steel, PTFE, ePTFE and a lower amount of other materials (*e.g.* polypropylene, polyester, PMMA, etc.). Another important contribution to the nVeto accomplishment is given by the tests of the 125 photomultipliers which will be installed in the support structure (5 of which will be used as spare). These tests were carried out at the Laboratori Nazionali del Gran Sasso. In order to observe the behavior of the PMTs in conditions similar to those in which they will be in the experiment, the measurements were also performed in water, inside the so-called Small Water Tank setup. The PMTs were characterized by measuring their gain, dark rate, transit time and transit time spread. In addition, we also planned a very interesting measurement regarding the influence of the Earth's magnetic field on the performance of PMTs, in order to decide whether to install or not a magnetic shield on the PMTs, which could mitigate a potential loss of their efficiency.

All the results of the tests carried out are in agreement with our expectations. The photomultipliers feature high gains, with an average value of $(8.22 \pm 0.07) \times 10^6$. On the other hand, the dark rate (DR) has been evaluated at different thresholds, expressed in terms of fractions of single photoelectron (spe). The average value at half-pe is (2.37 ± 0.16) kHz; this value is perfectly in agreement with the nVeto requirements, which aims at an overall tagging efficiency above 85%, as already mentioned. One PMT showed a huge DR, equal to (13.23 ± 0.12) kHz at 0.5 spe threshold; it is still unclear if it is due to electronic noise or intrinsic DR. Anyway, we can keep that PMT just as spare. The availability of very fast digitizers (featuring a temporal resolution of 1 ns) also made it possible to measure the temporal characteristics of the PMTs such as the signal formation time and its spread. Even in this case, the results are in accordance with expectations: the transit time becomes the same, within 1 ns, when the PMTs are set at the same supply voltage, and the transit time spread results to be below 4 ns. In addition, the transit time difference between the 125 PMTs has an RMS equals to 2.7 ns when the PMTs are set at the nominal high voltage.

The influence of the Earth's magnetic field on PMT performances is evident when measuring parameters such as the gain, the peak-to-valley and the PMT detection efficiency (indirectly measured through the so-called area ratio). However, the addition of a mu-metal magnetic shield did not show huge improvements to justify the efforts to install it on all the nVeto photomultipliers.

The data collection lasted approximately 3 months, while some minor analyses are still in progress. To conclude we can say that we are ready to complete the construction of the Neutron Veto, and to install the 120 photomultipliers on the

structure. This will be the last step necessary to complete the installation of the XENONnT experiment. The commissioning is foreseen to start in mid-2020.

Bibliography

[1] E. Aprile et al. "Dark Matter Search Results from a One Ton-Year Exposure of XENON1T". In: *Phys. Rev. Lett.* 121.11 (Sept. 2018).

[2] N. Aghanim et al. *Planck 2018 results. VI. Cosmological parameters*. 2018. arXiv: 1807.06209 [astro-ph.CO].

[3] F. Zwicky. "Die Rotverschiebung von extragalaktischen Nebeln". In: *Helv. Phys. Acta* 6 (1933), pp. 110–127.

[4] F. Zwicky. "The Coma Cluster of Galaxies". In: *Publications of the Astronomical Society of the Pacific* 63.371 (Apr. 1951), p. 61.

[5] E. M. Burbidge et al. "The rotation and mass of NGC 6503". In: *The Astrophysical Journal* 139 (1964), pp. 539–544.

[6] K.C. Freeman. "On the Disks of Spiral and S0 Galaxies". In: *The Astrophysical Journal* 160 (June 1970), p. 811.

[7] R. Massey, T. Kitching, and J. Richard. "The dark matter of gravitational lensing". In: *Reports on Progress in Physics* 73.8 (July 2010).

[8] F.W Dyson, A.S. Eddington, and C. Davidson. "A Determination of the Deflection of Light by the Sun's Gravitational Field, from Observations Made at the Total Eclipse of May 29, 1919". In: *Philosophical Transactions of the Royal Society of London Series A* 220 (Jan. 1920), pp. 291–333.

[9] K. Chang and S. Refsdal. "Flux variations of QSO 0957+561 A, B and image splitting by stars near the light path". In: *Nature* 282 (1979), pp. 561–564.

[10] B. Paczyński. "Gravitational Microlensing in the Local Group". In: *Annual Review of Astronomy and Astrophysics* 34.1 (1996), pp. 419–459.

[11] J.-P. Beaulieu et al. "Discovery of a cool planet of 5.5 Earth masses through gravitational microlensing". In: *Nature* 439.7075 (Jan. 2006), pp. 437–440. ISSN: 1476-4687.

[12] C. Alcock et al. "EROS and MACHO combined limits on planetary mass dark matter in the galactic halo". In: *The Astrophysical Journal* 499 (1998), p. L9.

[13] P. Tisserand et al. "Limits on the Macho content of the Galactic Halo from the EROS-2 Survey of the Magellanic Clouds". In: *Astronomy and Astrophysics* 469.2 (Apr. 2007), pp. 387–404.

[14] An. C. Becker et al. "The SuperMACHO Microlensing Survey". In: *Proceedings of the International Astronomical Union* 2004 (July 2004), pp. 357–362. ISSN: 1743-9221.

[15] Nathália Cibirka et al. "RELICS: Strong Lensing analysis of the galaxy clusters Abell S295, Abell 697, MACS J0025.4-1222, and MACS J0159.8-0849". In: *The Astrophysical Journal* 863 (Mar. 2018).

[16] J. R. Brownstein and J. W. Moffat. "The Bullet Cluster 1E0657-558 evidence shows modified gravity in the absence of dark matter". In: *Monthly Notices of the Royal Astronomical Society* 382.1 (Nov. 2007), pp. 29–47. ISSN: 1365-2966.

[17] D. Clowe, A. Gonzalez, and M. Markevitch. "Weak-Lensing Mass Reconstruction of the Interacting Cluster 1E 0657-558: Direct Evidence for the Existence of Dark Matter". In: *The Astrophysical Journal* 604.2 (Apr. 2004), pp. 596–603.

[18] A.A. Penzias and R.W. Wilson. "A Measurement of Excess Antenna Temperature at 4080 Mc/s." In: *The Astrophysical Journal* 142 (July 1965), pp. 419–421.

[19] D. J. Fixsen. "The Temperature of the Cosmic Microwave Background". In: *The Astrophysical Journal* 707.2 (Nov. 2009), pp. 916–920.

[20] G. Hinshaw et al. "Three-Year Wilkinson Microwave Anisotropy Probe (WMAP) Observations: Temperature Analysis". In: *The Astrophysical Journal Supplement Series* 170.2 (June 2007), pp. 288–334. ISSN: 1538-4365.

[21] M. Milgrom. "A modification of the Newtonian dynamics as a possible alternative to the hidden mass hypothesis." In: *The Astrophysical Journal* 270 (July 1983), pp. 365–370.

[22] Salvatore Capozziello and Mariafelicia De Laurentis. "Extended Theories of Gravity". In: *Physics Reports* 509.4-5 (Dec. 2011), pp. 167–321.

[23] B. P. Abbott et al. "Observation of Gravitational Waves from a Binary Black Hole Merger". In: *Phys. Rev. Lett.* 116 (6 Feb. 2016), p. 061102.

[24] A. G. Doroshkevich et al. *The Theory of Large-Scale Structure of the Universe: Local Properties and Global Topology*. Dordrecht: Springer Netherlands, 1983, pp. 387–391.

[25] Alexander Szalay and G. Marx. "Neutrino rest mass from cosmology". In: *Astronomy and Astrophysics* 49 (May 1976), pp. 437–441.

[26] Planck Collaboration. *Planck 2018 results. I. Overview and the cosmological legacy of Planck*. 2018. arXiv: 1807.06205 [astro-ph.CO].

[27] R.D. Peccei and Helen Quinn. "CP Conservation in the Presence of Pseudoparticles". In: *Phys. Rev. D* 38 (June 1977), pp. 1440–1443.

[28] R. Ballou et al. "New exclusion limits on scalar and pseudoscalar axionlike particles from light shining through a wall". In: *Phys. Rev. D* 92 (9 Nov. 2015), p. 092002.

[29] E. Zavattini et al. "New PVLAS results and limits on magnetically induced optical rotation and ellipticity in vacuum". In: *Phys. Rev. D* 77 (3 Feb. 2008), p. 032006.

[30] D.S. Akerib et al. “Results from a Search for Dark Matter in the Complete LUX Exposure”. In: *Phys. Rev. Lett.* 118.2 (Jan. 2017).

[31] E. Aprile et al. “XENON100 dark matter results from a combination of 477 live days”. In: *Phys. Rev. D* 94.12 (Dec. 2016).

[32] N. Du et al. “Search for Invisible Axion Dark Matter with the Axion Dark Matter Experiment”. In: *Phys. Rev. Lett.* 120.15 (Apr. 2018).

[33] Ki-Young Choi et al. *Searching for axino-like particle at fixed target experiments*. Jan. 2020. URL: http://dx.doi.org/10.1016/j.dark.2020.100460.

[34] Scott Dodelson and Lawrence M. Widrow. “Sterile neutrinos as dark matter”. In: *Phys. Rev. Lett.* 72.1 (Jan. 1994), pp. 17–20. ISSN: 0031-9007.

[35] Esra Bulbul et al. “Detection of an Unidentified Emission Line in the Stacked X-Ray Spectrum of Galaxy Clusters”. In: *The Astrophysical Journal* 789.1 (June 2014), p. 13. ISSN: 1538-4357.

[36] Matteo Guainazzi and Makoto S. Tashiro. *The Hot Universe with XRISM and Athena*. 2018. arXiv: 1807.06903 [astro-ph.IM].

[37] The Lynx Team. *The Lynx Mission Concept Study Interim Report*. 2018. arXiv: 1809.09642 [astro-ph.IM].

[38] R. Kaul. “Supersymmetric solution of gauge hierarchy problem”. In: *Pramana* 19 (Aug. 1982), pp. 183–188.

[39] Michael E. Peskin. *Supersymmetry in Elementary Particle Physics*. 2008.

[40] Toby Falk et al. “Heavy sneutrinos as dark matter”. In: *Physics Letters B* 339 (Nov. 1994), pp. 248–251.

[41] C. Csaba. “The Minimal Supersymmetric Standard Model”. In: *Modern Physics Letters A* 11.08 (Mar. 1996), pp. 599–613.

[42] Daniel J. H. Chung, Edward W. Kolb, et al. “Superheavy dark matter”. In: *Phys. Rev. D* 59.2 (Nov. 1998).

[43] Hsin-Chia Cheng, Jonathan L. Feng, and Konstantin T. Matchev. “Kaluza-Klein Dark Matter”. In: *Phys. Rev. Lett.* 89.21 (Oct. 2002).

[44] TH. KALUZA. “On the Unification Problem in Physics”. In: *International Journal of Modern Physics D* 27.14 (Oct. 2018), p. 1870001.

[45] Oskar Klein. “Quantentheorie und funfdimensionale Relativitatstheorie”. In: *Zeitschrift fur Physik* 37.12 (Dec. 1926), pp. 895–906.

[46] M. Tanabashi et al. “Review of Particle Physics”. In: *Phys. Rev. D* 98 (3 Aug. 2018), p. 030001.

[47] URL: http://pisrv0.pit.physik.uni-tuebingen.de/darkmatter/spectra/index.php.

[48] Marc Schumann. “Direct detection of WIMP dark matter: concepts and status”. In: *Journal of Physics G: Nuclear and Particle Physics* 46.10 (Aug. 2019), p. 103003.

[49] G. Bellini et al. “First evidence of pep solar neutrinos by direct detection in Borexino”. In: *Phys. Rev. Lett.* 108 (2012), p. 051302.

[50] Anne M Green. “Astrophysical uncertainties on the local dark matter distribution and direct detection experiments”. In: *Journal of Physics G: Nuclear and Particle Physics* 44.8 (June 2017), p. 084001.

[51] Mark W. Goodman et al. “Detectability of certain dark-matter candidates”. In: *Phys. Rev. D* 31 (12 June 1985), pp. 3059–3063.

[52] S.P. Ahlen et al. “Limits on cold dark matter candidates from an ultralow background germanium spectrometer”. In: *Physics Letters B* 195 (Sept. 1987), pp. 603–608.

[53] C. E. Aalseth et al. “CoGeNT: A search for low-mass dark matter usingp-type point contact germanium detectors”. In: *Phys. Rev. D* 88.1 (July 2013).

[54] R. Bernabei et al. “The DAMA/LIBRA apparatus”. In: *Nuclear Instruments and Methods in Physics Research Section A: Accelerators, Spectrometers, Detectors and Associated Equipment* 592.3 (July 2008), pp. 297–315.

[55] R. Bernabei et al. “First model independent results from DAMA/LIBRA-phase2”. In: *Nuclear Physics and Atomic Energy* 19.4 (Dec. 2018), pp. 307–325.

[56] C. Kelso et al. “Examining the time dependence of DAMA’s modulation amplitude”. In: *The European Physical Journal C* 78.3 (Mar. 2018).

[57] G. Adhikari et al. “Initial performance of the COSINE-100 experiment”. In: *The European Physical Journal C* 78.2 (Feb. 2018).

[58] Paolo Montini. *Dark matter search with the SABRE experiment*. 2018. arXiv: 1807.08073 [physics.ins-det].

[59] CDMS Collaboration, R. Agnese, et al. *Silicon Detector Dark Matter Results from the Final Exposure of CDMS II*. 2013. arXiv: 1304.4279 [hep-ex].

[60] R. Agnese et al. “Projected sensitivity of the SuperCDMS SNOLAB experiment”. In: *Phys. Rev. D* 95.8 (Apr. 2017).

[61] R. Strauss et al. “A prototype detector for the CRESST-III low-mass dark matter search”. In: *Nuclear Instruments and Methods in Physics Research Section A: Accelerators, Spectrometers, Detectors and Associated Equipment* 845 (Feb. 2017), pp. 414–417.

[62] G. Angloher et al. “Results from 730 kg days of the CRESST-II Dark Matter search”. In: *The European Physical Journal C* 72.4 (Apr. 2012).

[63] C. Amole et al. *Dark matter search results from the PICO-60 CF3I bubble chamber*. Mar. 2016. URL: http://dx.doi.org/10.1103/PhysRevD.93.052014.

[64] E. Aprile et al. “Search for Event Rate Modulation in XENON100 Electronic Recoil Data”. In: *Phys. Rev. Lett.* 115.9 (Aug. 2015).

[65] E. Aprile et al. “First Dark Matter Search Results from the XENON1T Experiment”. In: *Phys. Rev. Lett.* 119.18 (Oct. 2017).

[66] Xiangyi Cui et al. “Dark Matter Results from 54-Ton-Day Exposure of PandaX-II Experiment”. In: *Phys. Rev. Lett.* 119.18 (Oct. 2017).

[67] P. Agnes et al. “First results from the DarkSide-50 dark matter experiment at Laboratori Nazionali del Gran Sasso”. In: *Physics Letters B* 743 (Apr. 2015), pp. 456–466.

[68] D.S. Akerib et al. “The LUX-ZEPLIN (LZ) experiment”. In: *Nuclear Instruments and Methods in Physics Research Section A: Accelerators, Spectrometers, Detectors and Associated Equipment* 953 (Feb. 2020), p. 163047. ISSN: 0168-9002.

[69] P. Di Gangi. “Dark Matter Search with the XENON1T Experiment: Background Predictions, Data Analysis and Final Results”. PhD thesis. Alma Mater Studiorum - Università di Bologna, 2019.

[70] D. Thompson et al. “Calibration of the Energetic Gamma-Ray Experiment Telescope (EGRET) for the Compton Gamma-Ray Observatory”. In: *The Astrophysical Journal Supplement Series* 86 (June 1993), pp. 629–656.

[71] W. B. Atwood et al. “The Large Area Telescope on the Fermi Gamma-Ray Space Telescope Mission”. In: *The Astrophysical Journal* 697.2 (May 2009), pp. 1071–1102.

[72] D. Hooper and L. Goodenough. “Dark matter annihilation in the Galactic Center as seen by the Fermi Gamma Ray Space Telescope”. In: *Physics Letters B* 697.5 (Mar. 2011), pp. 412–428.

[73] Julian Sitarek et al. *Physics performance of the upgraded MAGIC telescopes obtained with Crab Nebula data*. 2013. arXiv: 1308.0141 [astro-ph.IM].

[74] J. Holder et al. “Status of the VERITAS Observatory”. In: *American Institute of Physics Conference Series* 1085 (Oct. 2008), p. 657.

[75] C. Hoischen et al. *GRB Observations with HESS II*. 2017. arXiv: 1708.01088 [astro-ph.HE].

[76] R. M. Wagner et al. *The CTA Observatory*. 2009. arXiv: 0912.3742 [astro-ph.IM].

[77] M. L. Ahnen et al. “Limits to dark matter annihilation cross-section from a combined analysis of MAGIC and Fermi-LAT observations of dwarf satellite galaxies”. In: *Journal of Cosmology and Astroparticle Physics* 2016.02 (Feb. 2016), pp. 039–039.

[78] L. Cazon. *The Pierre Auger Observatory: new results and prospects*. 2018. arXiv: 1808.00745 [astro-ph.HE].

[79] R.U. Abbasi et al. “Study of Ultra-High Energy Cosmic Ray composition using Telescope Array’s Middle Drum detector and surface array in hybrid mode”. In: *Astroparticle Physics* 64 (Apr. 2015), pp. 49–62.

[80] O. Adriani et al. “Ten years of PAMELA in space”. In: *Riv. Nuovo Cim.* 40.10 (2017), p. 1. DOI: 10.1393/ncr/i2017-10140-x. arXiv: 1801.10310 [astro-ph.HE].

[81] Hong-Bo Jin, Yue-Liang Wu, and Yu-Feng Zhou. *Astrophysical background and dark matter implication based on latest AMS-02 data*. 2017. arXiv: 1701.02213 [hep-ph].

[82] Hsin-Chia Cheng et al. "AMS-02 positron excess and indirect detection of three-body decaying dark matter". In: *Journal of Cosmology and Astroparticle Physics* 2017.03 (Mar. 2017), pp. 041–041.

[83] Su-Jie Lin et al. "Systematic study on the cosmic ray antiproton flux". In: *Phys. Rev. D* 96.12 (Dec. 2017).

[84] A. Albert et al. *The ANTARES Collaboration: Contributions to ICRC 2017 Part II: The multi-messenger program*. 2017. arXiv: 1711.01486 [astro-ph.HE].

[85] Dawn R. Williams. *Results from IceCube*. 2019. arXiv: 1909.05173 [astro-ph.HE].

[86] H. Sekiya. *Recent Results from Super-Kamiokande*. 2008. arXiv: 0810.0595 [astro-ph].

[87] Hyper-Kamiokande Proto-Collaboration: K. Abe et al. *Hyper-Kamiokande Design Report*. 2018. arXiv: 1805.04163 [physics.ins-det].

[88] Dmitry Zaborov. "The KM3NeT Neutrino Telescope and the potential of a neutrino beam from Russia to the Mediterranean Sea". In: *Proceedings, 18th Lomonosov Conference on Elementary Particle Physics: Moscow, Russia, August 24-30, 2017*. 2019, pp. 53–60. DOI: 10.1142/9789811202339_0009. arXiv: 1803.08017 [hep-ex].

[89] S F King. "Neutrino oscillations: status, prospects and opportunities at a neutrino factory". In: *Journal of Physics G: Nuclear and Particle Physics* 27.10 (Sept. 2001), pp. 2149–2170.

[90] A. Renshaw. "Research and Development for a Gadolinium Doped Water Cherenkov Detector". In: *Physics Procedia* 37 (Jan. 2012).

[91] M. Ikeda et al. *Evaluation of Gadolinium's Action on Water Cherenkov Detector Systems with EGADS*. 2019. arXiv: 1908.11532 [physics.ins-det].

[92] John F. Beacom and Mark R. Vagins. "Antineutrino Spectroscopy with Large Water Čerenkov Detectors". In: *Phys. Rev. Lett.* 93.17 (Oct. 2004).

[93] F. Kahlhoefer. "Review of LHC dark matter searches". In: *International Journal of Modern Physics A* 32.13 (May 2017), p. 1730006.

[94] E. Aprile et al. "Design and performance of the XENON10 dark matter experiment". In: *Astroparticle Physics* 34.9 (Apr. 2011), pp. 679–698.

[95] J. Angle, E. Aprile, et al. "Limits on Spin-Dependent WIMP-Nucleon Cross Sections from the XENON10 Experiment". In: *Phys. Rev. Lett.* 101.9 (Aug. 2008).

[96] J. Angle, E. Aprile, et al. "First Results from the XENON10 Dark Matter Experiment at the Gran Sasso National Laboratory". In: *Phys. Rev. Lett.* 100.2 (Jan. 2008).

[97] E. Aprile et al. "Dark Matter Results from 225 Live Days of XENON100 Data". In: *Phys. Rev. Lett.* 109.18 (Nov. 2012).

[98] E. Aprile et al. "Limits on Spin-Dependent WIMP-Nucleon Cross Sections from 225 Live Days of XENON100 Data". In: *Phys. Rev. Lett.* 111.2 (July 2013).

[99] E. Aprile et al. "Constraining the Spin-Dependent WIMP-Nucleon Cross Sections with XENON1T". In: *Phys. Rev. Lett.* 122.14 (Apr. 2019).

[100] J. B. Albert et al. "Improved measurement of the $2\nu\beta\beta$ half-life of 136Xe with the EXO-200 detector". In: *Phys. Rev. C* 89.1 (Jan. 2014).

[101] "Observation of two-neutrino double electron capture in 124Xe with XENON1T". In: *Nature* 568.7753 (Apr. 2019), pp. 532–535.

[102] C. Wittweg. "XENON100 Dark Matter Search with the PAX Raw Data Processor for XENON1T". MA thesis. Westfälische Wilhelms-Universität Münster, 2016.

[103] E. Aprile et al. "Physics reach of the XENON1T dark matter experiment." In: *Journal of Cosmology and Astroparticle Physics* 2016.04 (Apr. 2016), pp. 027–027.

[104] E. Aprile et al. "Material radioassay and selection for the XENON1T dark matter experiment". In: *The European Physical Journal C* 77.12 (Dec. 2017).

[105] E. Aprile et al. "The XENON1T dark matter experiment". In: *The European Physical Journal C* 77.12 (Dec. 2017).

[106] Ch. Geis et al. "Optical response of highly reflective film used in the water Cherenkov muon veto of the XENON1T dark matter experiment". In: *Journal of Instrumentation* 12.06 (June 2017), P06017–P06017.

[107] F. Agostini. "Caratterizzazione e calibrazione dei fotomoltiplicatori del sistema di veto di muoni per l'esperimento XENON1T". MA thesis. Alma Mater Studiorum - Università di Bologna, 2013.

[108] E. Aprile et al. "Conceptual design and simulation of a water Cherenkov muon veto for the XENON1T experiment". In: *Journal of Instrumentation* 9.11 (Nov. 2014), P11006–P11006. ISSN: 1748-0221. DOI: 10.1088/1748-0221/9/11/p11006. URL: http://dx.doi.org/10.1088/1748-0221/9/11/P11006.

[109] Kaito Hagiwara et al. "Gamma Ray Spectrum from Thermal Neutron Capture on Gadolinium-157". In: *PTEP* 2019.2 (2019), p. 023D01. DOI: 10.1093/ptep/ptz002. arXiv: 1809.02664 [nucl-ex].

[110] C. Palomares et al. *Double-Chooz Neutrino Experiment*. 2009.

[111] C. Simpson et al. "Sensitivity of Super-Kamiokande with Gadolinium to Low Energy Antineutrinos from Pre-supernova Emission". In: *The Astrophysical Journal* 885.2 (Nov. 2019), p. 133.

[112] H. Sekiya. "Supernova neutrinos in SK-Gd and other experiments". In: *Journal of Physics: Conference Series* 888 (Sept. 2017), p. 012041. DOI: 10.1088/1742-6596/888/1/012041.

[113] D. Ramirez. "Radiogenic Background Simulations for XENONnT". In: Poster presented at TAUP conference, Toyama, Japan.

[114] S.O. Flyckt and K. Marmorier. *Photomultiplier Tubes: principles and applications*.

[115] Hamamatsu Photonics K. K. *Photomultiplier Tubes: Basics and Applications*.

[116] INGV. *Cartografia Magnetica Nazionale*. 2015. URL: http://roma2.rm.ingv.it/it/risorse/rete_magnetica_italiana/36/cartografia_magnetica_nazionale.

[117] P. DeVore et al. "Light-weight flexible magnetic shields for large-aperture photomultiplier tubes". In: *Nuclear Instruments and Methods in Physics Research Section A: Accelerators, Spectrometers, Detectors and Associated Equipment* 737 (Feb. 2014), pp. 222–228.

[118] A. Higuera. *Results and Prospects from the Daya Bay Reactor Neutrino Experiment*. 2016. arXiv: 1607.07324 [hep-ph].

[119] E. Aprile et al. "Lowering the radioactivity of the photomultiplier tubes for the XENON1T dark matter experiment". In: *The European Physical Journal C* 75.11 (Nov. 2015).

[120] Hamamatsu. *PMT R5912*. URL: https://www.hamamatsu.com/eu/en/product/type/R5912/index.html.

[121] CAEN. *V1751*. URL: https://www.caen.it/products/v1751/.

[122] *The EPL Series: Picosecond Pulsed Diode Lasers*. 2014.

[123] W. R. Leo. *Techniques for Nuclear and Particle Physics Experiments: A How to Approach*. 1987.

[124] XENON Collaboration. "Physics Reach of the XENONnT Experiment in WIMP Searches". in press.